Università degli Studi di Napoli "Federico II"
Scuola Superiore Meridionale

Mathematical and physical sciences for advanced materials and technologies

Ph.D. Thesis

Measurement of $B^{+} \to \tau^{+}\nu_{\tau}$ branching fraction with a hadronic tagging method at Belle II

Supervisor:
Prof. Gugliemo De Nardo

Ph.D. Student:
Giovanni Gaudino

XXXVII cycle

INTRODUCTION

Belle II is a flavour physics experiment that aims to search for new physics (NP) beyond the standard model (SM) of elementary particles and improve the precision of some fundamental parameters of this model. The experiment is the successor of the Belle experiment and its general-purpose detector is installed at the e^+e^- SuperKEKB collider, at the KEK laboratories in Tsukuba, Japan. The accelerator collides electrons and positrons at an energy of the center-of-mass of 10.58 GeV, in correspondence with the $\Upsilon(4S)$ resonance, which decays mainly in B mesons pairs. The energy of the two beams is different to boost the center of mass and measure the time-dependent charge-parity (CP) asymmetry.
In this thesis project, I present a measurement for the $B^+ \to \tau^+\nu_\tau$[1] decay, which is a rare process in the SM, sensitive to NP. The study is based on the Belle II experiment Run1 dataset, which corresponds to $(387 \pm 6) \times 10^6$ $\Upsilon(4S)$ (integrated luminosity of 365 fb^{-1}). Assuming the SM, the $B^+ \to \tau^+\nu_\tau$ decay mode provides an alternative way to determine the magnitude of the CKM matrix element $|V_{ub}|$ that is independent of determinations obtained through the reconstruction of exclusive semileptonic $B^+ \to \pi^0\ell^+\nu_\ell$ modes, which are typically studied for this purpose. Moreover, the $B^+ \to \tau^+\nu_\tau$ decay is sensitive to contributions beyond the SM, such as those predicted by models with a charged Higgs boson, or various super-symmetric extensions of the SM. These models can both suppress or enhance the branching ratio of the $B^+ \to \tau^+\nu_\tau$ decay and affect the extraction of $|V_{ub}|$.
We select the signal events by a likelihood fit to the reconstructed $B^+ \to \tau^+\nu_\tau$ candidate events and estimate the branching fraction of the decay.
The result was finally published in October 2025, on *Phys. Rev. D 112, 072002*.

OUTLINE OF THE THESIS

This thesis is organized as follows:

1 Throughout this thesis, the inclusion of the charge-conjugate decay mode is implied unless otherwise stated.

- Chapter 1 provides the theoretical background of flavor physics, discussing the fundamental principles and symmetries that govern particle interactions, with a focus on the role of the CKM matrix and its implications for rare decays. Morover it provides an overview of B meson physics, focusing on the theoretical framework and experimental techniques relevant to the study of rare decays.
- Chapter 2 describes the Belle II experiment, including its design, detector components, and data production workflow.
- Chapter 3 details the reconstruction algorithms and cut-based event selection strategies used to isolate signal events from background processes.
- Chapter 4 discusses the optimization of signal selection criteria to enhance the sensitivity of the analysis.
- Chapter 5 covers the calibration and validation procedures employed to ensure the of the simulation for the goodness of the result.
- Chapter 6 presents the methodology for extracting the branching ratio of $B^+ \to \tau^+ \nu_\tau$ from the data and the final result.
- Chapter 7 addresses systematic uncertainties that affect the measurement and their impact on the final results.
- Finally, the thesis concludes with a summary of the main results and their significance in the context of flavor physics.

After the main body of the thesis, I also include three appendices:

- Appendix A provides a detailed description of the Full Event Interpretation (FEI) algorithm, which is a machine-learning-based technique used for the full reconstruction of B meson decays in the Belle II experiment. The FEI plays a crucial role in enhancing the efficiency and purity of signal event selection, both in my analysis and in the broader Belle II physics program.
- Appendix B provides an overview of the Run Dependent Monte Carlo at Belle II, detailing the methodology and results of the Monte Carlo simulations used to model the detector response and optimize the analysis. During my Ph.D., I contributed to the production of the Run Dependent Monte Carlo for the Belle II experiment.

- Appendix C presents a study on the feasibility of implementing dual-readout techniques in homogeneous scintillating crystals, specifically bismuth germanate (BGO) and bismuth silicate (BSO), utilizing Silicon Photomultipiers (SiPMs) to achieve the discrimination between scintillation and Čerenkov light components required for dual-readout operation. This work was conducted, together with the Milano Bicocca and University of Perugia FCC-ee groups, as part of the DRDCalo activities for the Future Circular Collider (FCC) project.

CONTENTS

1 THEORETICAL BACKGROUND

1.1 THE STANDARD MODEL OF PARTICLE PHYSICS

The standard model (SM) is a theoretical framework that describes the elementary particles and three of the four fundamental interactions in nature: electromagnetism, the strong interaction, and the weak interaction [1, 2, 3, 4, 5, 6].
This model is built upon a Lagrangian formalism, where the dynamics of the fields are constrained by the requirement of local gauge invariance. The interactions arise from the invariance of the Lagrangian under local transformations associated with symmetry groups. For each interaction, a group is assigned. The $SU(3)_C$ characterizes the strong interaction (quantum chromodynamics, QCD), with "C" denoting color charge, and $SU(2)_L \otimes U(1)_Y$ describes the electroweak interaction, where L refers to left-handedness and Y to hypercharge.
Each fundamental interaction is characterized by one or more universal coupling constants, which reflect the strength of the corresponding gauge symmetry.
The mediators of these interactions are spin-1 particles known as *gauge bosons*:

- **Strong force:** transmitted by eight massless gluons, corresponding to the generators of $SU(3)_C$.

- **Electroweak sector:** comprises the $W^{\pm}$, Z^0, which emerge from the spontaneous breaking of the $SU(2)_L \otimes U(1)_Y$ gauge symmetry, and the photon γ, which remains massless. The charged current interactions are mediated by the $W^{\pm}$ bosons, which are defined as linear combinations of the $SU(2)_L$ gauge fields:

$$W^{\pm} = \frac{1}{\sqrt{2}}(W_1 \mp \imath W_2), \tag{1.1}$$

  where W_1 and W_2 are the generators of $SU(2)_L$. The neutral current and electromagnetic interactions are mediated by the Z^0 boson and photon γ, respectively, which are obtained through the mixing of the neutral gauge fields:

$$\begin{pmatrix} \gamma \\ Z^0 \end{pmatrix} = \begin{pmatrix} \cos\vartheta_W & \sin\vartheta_W \\ -\sin\vartheta_W & \cos\vartheta_W \end{pmatrix} \begin{pmatrix} B \\ W_3 \end{pmatrix}, \tag{1.2}$$

where B is the $U(1)_Y$ gauge field, W_3 is the third component of the $SU(2)_L$ gauge field, and ϑ_W is the Weinberg angle, which parameterizes the electroweak mixing and relates the gauge couplings to the masses of the $W^{\pm}$ and Z^0 bosons.

- **Higgs mechanism:** all massive particles acquire their mass through interactions with the Higgs field, mediated by the null-spin Higgs boson.

The constituents of matter are spin-1/2 fields called *fermions*, each paired with a corresponding antiparticle. Fermions are organized into quarks and leptons, each forming three generations of weak isospin doublets.
Quark doublets comprise an up-type quark (charge $+2e/3$) and a down-type quark (charge $-e/3$): (u, d), (c, s), and (t, b). Here, e is the elementary proton charge. Quarks participate in both strong and electroweak interactions, carrying color and flavor quantum numbers. Due to color confinement, free quarks are never observed; instead, they form color-neutral bound states: mesons (quark-antiquark pairs) and baryons (three-quark states). Baryons possess a conserved quantum number known as baryon number.
Lepton doublets consist of a nearly massless neutrino and a charged lepton (charge $-e$): (ν_e, e^-), (ν_μ, μ^-), and (ν_τ, τ^-). Leptons interact exclusively via electroweak forces. Each lepton flavor is associated with a global lepton number, which is conserved in most interactions, although individual lepton numbers are violated in neutrino oscillations. Beyond gauge symmetries, discrete symmetries are also fundamental. These include parity (P), which inverts spatial coordinates; charge conjugation (C), which exchanges particles with their antiparticles; and time reversal (T). While the combined CPT symmetry is a cornerstone of quantum field theory [7, 8], the individual symmetries are not always respected. Parity and CP symmetries are maximally violated in weak interactions [9, 10]. Although the strong interaction could, in principle, violate CP symmetry, no such violation has been detected, motivating the hypothesis of axions as a possible solution [11].

1.2 EXPERIMENTAL TESTS OF THE STANDARD MODEL

Finalized in the 1970s, the SM has demonstrated extraordinary predictive power, successfully passing an immense number of experimental tests with unprecedented precision, sometimes reaching relative uncertainties as low as one part per trillion [12]. Despite its triumphs, both experimental observations and the-

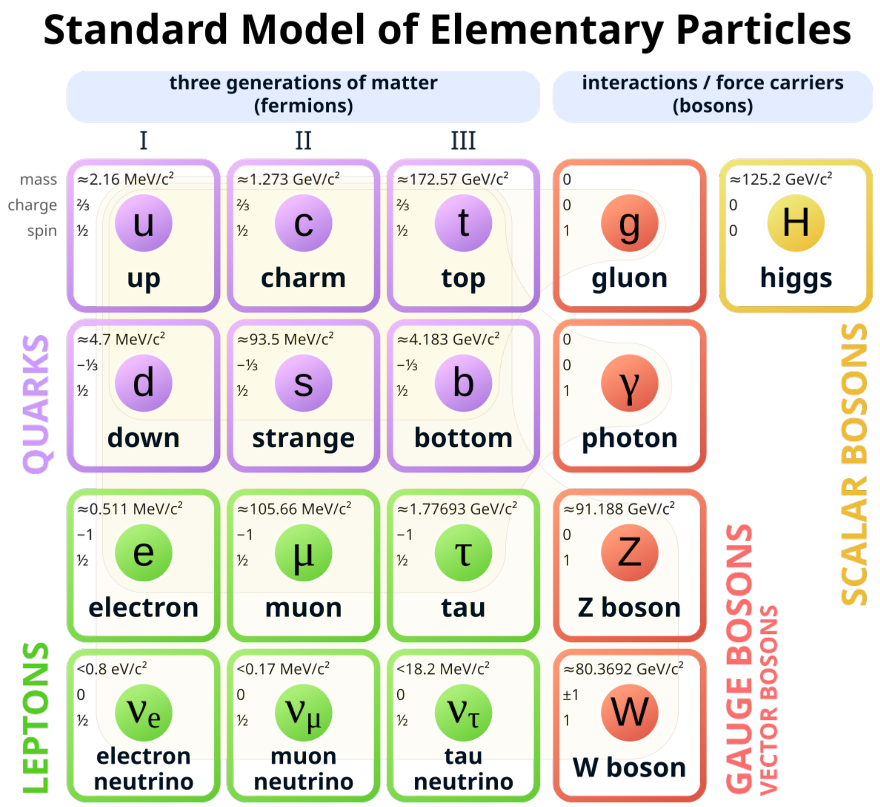

Figure 1.1: Schematic representation of the SM particles and their interactions.

oretical considerations indicate that the SM is not the ultimate description of nature, but rather an effective theory valid within the energy range explored so far (from the eV to the TeV scale).

Among the most profound open questions, the origin of the observed matter-antimatter asymmetry in the Universe remains unexplained. Fermion masses still lacks any principle within the current theoretical framework. Furthermore, a consistent quantum field theory of gravity is still absent from the SM, leaving one of the fundamental forces outside its scope. Finally, cosmological evidence strongly indicates the existence of dark matter (and dark energy), yet the SM does not provide any seen candidate for this mysterious component of the Universe.

These unresolved issues drive the ongoing quest to extend the SM. Two complementary research strategies are currently pursued.

The first is the **energy frontier** approach, which seeks direct evidence of new physics by producing heavy, non-SM particles in high-energy collisions. When kinematically accessible, such particles can be detected via their decay products. Historically, this strategy has led to major discoveries, such as the top quark and the Higgs boson, but its reach is fundamentally limited by the maximum energy achievable at current and future colliders.

The second strategy is the **intensity frontier**, which rather than producing new particles directly, aims to uncover indirect signs of new physics by searching for deviations in high-precision measurements. Such deviations may arise from virtual (off-shell) contributions of heavy particles, which manifest as subtle corrections to observables at lower energies. Heisenberg's uncertainty principle ($\Delta E\,\Delta t \geqslant \hbar/2$) permits these virtual effects over short timescales. This strategy is particularly powerful when comparing SM predictions with precise experimental results in rare or forbidden processes. This approach is historically fundamental for the discovery of the Higgs boson, which was first observed in precision measurements of electroweak observables before being directly produced at the LHC. It has also led to the discovery of the nature of the weak interaction, via the β decay, overcoming the 4-fermions interaction model proposed by Fermi in the 1930s.

Among the most promising arenas for the intensity frontier is the study of weak interactions among quarks, commonly known as *flavor physics*, which focuses on the properties and interactions of quarks and leptons, particularly in processes that change one flavor into another. Flavor physics has played a central role in the development of the SM, particularly in addressing inconsistencies in weak interaction data observed in the mid-20th century.

1.3 FLAVOR PHYSICS IN A NUTSHELL

The term *Flavor* was first used in particle physics in the context of the quark model of hadrons. It was coined in 1971 by Murray Gell-Mann and his student at the time, Harald Fritzsch, at a *Baskin-Robbins* ice-cream store in Pasadena.

> *Just as ice cream has both color and flavor so do quarks* [13].

"Flavor" is now used slightly more generally to denote the family of any SM fermion, both quarks and leptons, and the "Flavor" physics studies how quarks and leptons mix each other. Till then, only three quarks were discovered (u, d and s), related to each other by Nicola Cabibbo mechanism [14], which in 1963 theorized the universality of the $V - A$ structure including a quark mixing between the negative charged quarks. Specifically, a mixing angle ϑ_C (now known as the Cabibbo angle) was introduced to describe the mixing between the d and s quarks:

$$\begin{pmatrix} d' \\ s' \end{pmatrix} = \begin{pmatrix} \cos\vartheta_C & \sin\vartheta_C \\ -\sin\vartheta_C & \cos\vartheta_C \end{pmatrix} \begin{pmatrix} d \\ s \end{pmatrix} . \tag{1.3}$$

While this formulation explained the discrepancies in weak decay rates, it also predicted rates for rare decays such as $K^0_L \to \mu^+ \mu^-$ that were too large compared to experimental limits. This tension led Glashow, Iliopoulos, and Maiani to postulate the existence of a fourth quark, the charm quark (c), whose contribution to these decay amplitudes would cancel the divergent terms from the u quark, suppressing the branching fractions to experimentally acceptable levels [15]. This mechanism, known as the GIM mechanism, successfully predicted the charm quark, which was discovered a few years later [16, 17].
In 1973, Kobayashi and Maskawa extended this framework to include three generations of quarks in order to explain the observed violation of the combined charge-conjugation and parity (CP) symmetry in K meson decays [18]. They introduced a 3×3 unitary matrix, now known as the Cabibbo-Kobayashi-Maskawa (CKM) matrix, which relates the weak eigenstates (d', s', b') to the mass eigenstates (d, s, b):

$$\begin{pmatrix} d' \\ s' \\ b' \end{pmatrix} = \begin{pmatrix} V_{ud} & V_{us} & V_{ub} \\ V_{cd} & V_{cs} & V_{cb} \\ V_{td} & V_{ts} & V_{tb} \end{pmatrix} \begin{pmatrix} d \\ s \\ b \end{pmatrix} . \tag{1.4}$$

Each element V_{ij} encodes the strength of the weak-interaction coupling between an up-type quark i and a down-type quark j via $W^{\pm}$ boson exchange.

While the CKM matrix for N quark generations is a general $N \times N$ unitary matrix with N^2 complex entries, the requirements of unitarity and the freedom to redefine quark field phases reduce the number of independent physical parameters to $(N-1)^2$. In the case of three generations, the CKM matrix is fully specified by three real mixing angles and a single irreducible complex phase, the latter being responsible for CP violation within the Standard Model.
A convenient parametrization of the CKM matrix is given by Wolfenstein [19], where the elements are expanded in terms of the small parameter $\lambda = \sin\vartheta_C \approx 0.23$:

$$V_{\text{CKM}} = \begin{pmatrix} 1-\frac{\lambda^2}{2} & \lambda & A\lambda^3(\rho - \imath\eta) \\ -\lambda & 1-\frac{\lambda^2}{2} & A\lambda^2 \\ A\lambda^3(1-\rho-\imath\eta) & -A\lambda^2 & 1 \end{pmatrix} + \mathcal{O}(\lambda^4),$$

where A, ρ, and η are real parameters. The unitarity of the CKM matrix implies that the rows and columns form orthonormal vectors. This gives rise to six unitarity conditions, which can be represented as triangles in the complex plane. The angles of these triangles are directly related to measurable CP-violating processes.
The CKM matrix is thus a key component of the SM, enabling flavor-changing weak decays and providing the only known source of CP violation within the model. Its structure, determined by experimental measurements, plays a central role in the search for new physics.

1.3.1 The unitarity triangle

The unitarity triangle is a graphical representation of the unitarity condition of the CKM matrix, which states that the sum of the products of the elements in any row or column must equal zero. For the CKM matrix, one of the most commonly used unitarity triangles is formed by the elements of the first row and the first column:

$$V_{ud}^* V_{ub} + V_{cd}^* V_{cb} + V_{td}^* V_{tb} = 0. \tag{1.5}$$

Figure 1.2 illustrates this triangle in the complex plane, where each vertex corresponds to a CKM matrix element. The sides of the triangle are given by the magnitudes of these elements, while the angles are related to the phases of the CKM matrix [20].
The angles of the triangle are related to the CP-violating phases in the CKM matrix. The most commonly used angles are:

- $\alpha/\phi_2 = \arg(-V_{td}^* V_{tb}/V_{ud}^* V_{ub})$,

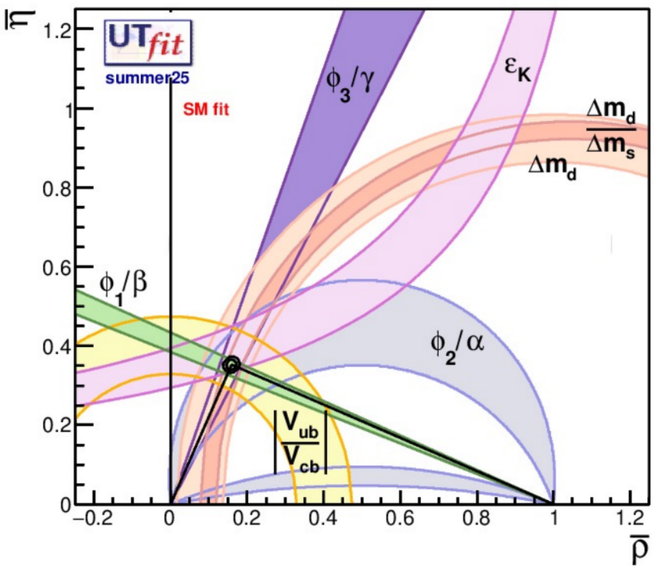

Figure 1.2: The unitarity triangle in the complex plane, illustrating the CKM matrix unitarity condition.

- $\beta/\phi_1 = \arg(-V^*_{cd}V_{cb}/V^*_{ud}V_{ub})$,
- $\gamma/\phi_3 = \arg(-V^*_{td}V_{tb}/V^*_{cd}V_{cb})$.

These angles are crucial for understanding CP violation in B meson decays and are measured through various decay processes. The unitarity triangle provides a powerful tool for testing the consistency of the CKM matrix and searching for new physics beyond the SM. Deviations from the expected angles or sides of the triangle could indicate the presence of additional sources of CP violation or new particles that affect flavor-changing processes.
All the parameter of the CKM matrix (the angles, the sides and the area) are determined through experimental measurements of various flavor-changing processes, *e.g.* B meson decays.

1.4 B MESON DECAYS

The study of B meson decays provides insights into the CKM matrix and CP violation. The B meson system consists of two types of mesons: charged $B^\pm$ mesons and neutral B^0 mesons. The charged $B^\pm$ mesons are composed of a bottom quark (b) and an up-type quark (u or c), while the neutral B^0 mesons consist of a bottom quark and a down-type quark (d, s). The production of B^+ and B^0 mesons (or simply B) occurs primarily through the decay of the $\Upsilon(4S)$ resonance, which is produced in e^+e^- collisions at the Belle and Belle II experiments. In Chap. 2, an overview of the Belle II experiment is done.

1.4.1 Hadronic decays of B mesons

Hadronic decays of B mesons are processes in which a B meson decays into a final state consisting of hadrons, which are composite particles made up of quarks and gluons. These decays are of great interest in flavor physics because they provide valuable information about the properties of the B meson system, the CKM matrix, and CP violation.
The hadronic decays of B mesons can be classified into two main categories:

- **Tree-level decays:** These decays occur through the exchange of a virtual W boson and involve a direct transition from the initial B meson to the final state hadrons. Tree-level decays are typically characterized by a simple topology, where the B meson decays into a final state consisting of two or more hadrons. Examples include decays like $B \to D\,\pi$, $B \to D^*\,\pi$, and $B \to D_s^+\,K$. These decays are often dominated by the CKM matrix elements and provide important information about the unitariery triangle angles and CP violation

- **Penguin decays:** These decays involve loop diagrams where the B meson decays into a virtual particle, which then decays into the final state hadrons. Penguin decays are typically more complex and can involve multiple intermediate states. They are often suppressed compared to tree-level decays but can provide valuable information about higher-order corrections and new physics contributions.

Figure 1.3 shows two possible cases of hadronic B decays. These decays are crucial for understanding the dynamics of the B meson system and testing the predictions of the SM. They also play a key role in searches for new physics, as deviations from the expected decay rates or patterns could indicate the presence of new particles or interactions beyond the SM.

1.4.2 Semi-leptonic decays of B mesons

Semileptonic B decays are processes in which a B meson decays into a lepton, its associated neutrino, and one or more hadrons. Within the SM, the $b \to c/u$

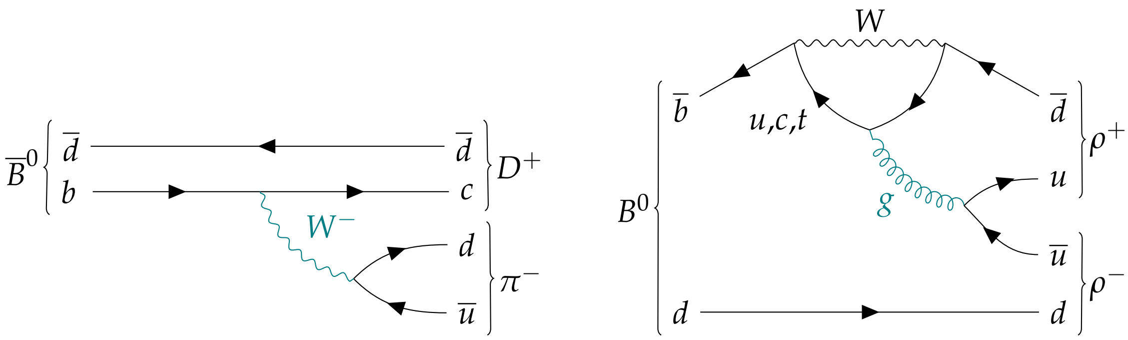

(a) Tree-level decay **(b)** Penguin decay

Figure 1.3: Feynman diagrams illustrating the two main types of hadronic decays of B mesons: (a) tree-level decay and (b) penguin decay. The tree-level decay involves a direct transition from the initial B meson to the final state hadrons, while the penguin decay involves a loop diagram.

transition occurs at tree level via the exchange of a W boson, as illustrated in Fig. 1.4. The effective Lagrangian (*à la Fermi*) describing this kinds of process is (from Ref. [21]):

$$\mathcal{L}_{\text{eff}} = -\frac{4G_F}{\sqrt{2}} V_{cb} (\bar{c}\gamma^\mu P_L b)(\bar{\ell}\gamma_\mu P_L \nu_\ell) + \text{h.c.} \tag{1.6}$$

Here, the fermion field $\psi = c, b, \ell, \nu$ denotes the Dirac spinor, with L and R indicating left- and right-handed chiralities, respectively. The lepton ℓ can be an electron, muon, or τ. The Fermi constant G_F is defined as $(\sqrt{2}/8)g_W^2/m_W^2$, where g_W is the $SU(2)$ weak coupling constant. The projection operators $P_{L,R} = (1 \mp \gamma_5)/2$ select the left- or right-handed components, and γ_5 is the usual Dirac matrix.
Since the W boson is much heavier than the B meson, semileptonic B decays are effectively described by a four-fermion interaction at leading order.

1.4.3 Leptonic decays of B mesons

The SM provides a very precise theoretical prediction of the branching fraction of leptonic B decays, for these reason a precise measure of this quantity could be an important stress of the model. The calculation gives:

$$\mathcal{B}(B \to \ell\nu_\ell) = \frac{G_F^2 m_B m_\ell^2}{8\pi}\left[1 - \frac{m_\ell^2}{m_B^2}\right]^2 f_B^2 |V_{ub}|^2 \tau_B, \tag{1.7}$$

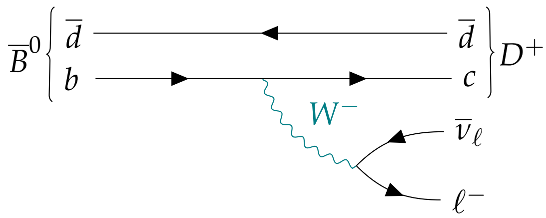

Figure 1.4: Feynman diagram illustrating the semileptonic decay of a B meson into a charm quark, a charged lepton, and its associated neutrino via the exchange of a virtual W boson.

where G_F is the Fermi constant, m_B and m_ℓ are the B^+ meson and the lepton masses, respectively, and τ_B is the B^+ lifetime.
As Eq. 1.7 shows, the τ channel has the highest branching fraction of a purely leptonic decay of B meson. Moreover, with the actual statistics limitations, only an upper limit for the branching fraction of $\mu\nu$ mode can be measured, while the $e\nu$ decay is detectable only if new physics greatly enhances its decay rate.
The last value reported on the PDG review [22] for $\mathcal{B}(B^+ \to \tau^+\nu_\tau)$ is $(1.09 \pm 0.24) \times 10^{-4}$. In the SM context, the observation of $B \to \tau\nu_\tau$ provides an experimental value of f_B (considering as known $|V_{ub}|$). Viceversa, if f_B is calculated precisely from QCD lattice, the branching ratio measurement could bring to an indirect measurement of $|V_{ub}|$.
Even if the purely leptonic decay offers a clean signature to extract the signal events from the backgrounds, the helicity suppression makes the decay in the muon and electron channels harder to study.
Belle and BABAR measured $\mathcal{B}(B^+ \to \tau^+\nu_\tau)$ reconstructing the accompanying B^- meson in hadronic decays [23, 24] or semileptonic decays [25, 26]. Table 1.1 shows past measurements and the current world average.

Table 1.1: Published results for $\mathcal{B}(B^+ \to \tau^+\nu_\tau)$ by Belle, BABAR and the PDG average.

Experiment	Tag	$\mathcal{B}(10^{-4})$
Belle	Hadronic	$0.72^{+0.27}_{-0.25} \pm 0.11$
BABAR	Hadronic	$1.83^{+0.53}_{-0.49} \pm 0.24$
Belle	Semileptonic	$1.25 \pm 0.28 \pm 0.27$
BABAR	Semileptonic	$1.7 \pm 0.8 \pm 0.2$
PDG[22]		1.09 ± 0.24

1.5 (SEMI-)LEPTONIC B DECAYS: A MODERN PERSPECTIVE

In the SM, the charged weak current couples universally to all three generations of lepton doublets, a property known as *lepton flavor universality* (LFU). This feature arises naturally from the structure of the electroweak interaction, which treats all lepton families identically except for their masses. Tests of LFU thus provide a sensitive probe for new physics.
Over the past decade, several measurements by the BABAR, Belle, and LHCb experiments have revealed intriguing tensions with SM predictions in semileptonic B decays. These so-called *LFU anomalies in B decays* are observed in transitions of the type $\bar{B} \to D^{(*)}\ell^-\bar{\nu}_\ell$.
The key observables are ratios of branching fractions for decays that differ only in the flavor of the final-state charged lepton. In particular, the following ratios are defined:

$$R(D^{(*)})_{\tau/\ell} = \frac{\mathcal{B}(\bar{B} \to D^{(*)}\tau^-\bar{\nu}_\tau)}{\mathcal{B}(\bar{B} \to D^{(*)}\ell^-\bar{\nu}_\ell)}, \tag{1.8}$$

where ℓ denotes either a light lepton (electron or muon). In the SM, these ratios are predicted with high precision, with only small corrections due to lepton mass differences.
The Heavy Flavor Averaging Group (HFLAV) reports the current world averages for these ratios [27], reported in Fig. 1.5. The current world averages exceed the SM predictions by approximately 3.77σ.
If confirmed, these deviations could indicate an enhancement in the $b \to c\tau^-\bar{\nu}_\tau$ transition mediated by new interactions beyond the SM. Several classes of models have been proposed to explain these anomalies, including:

- Tree-level exchange of a heavy W' boson (the charged counterpart of a Z') [28];
- Scalar contributions from a charged Higgs boson [29, 30, 31, 32, 33];
- Leptoquarks, hypothetical particles that couple simultaneously to quarks and leptons [34, 35];
- Supersymmetric extensions of the SM [36, 37]

In most of these scenarios, a sizable new-physics contribution would be required to account for the observed enhancements in $R(D^{(*)})$, which would likely also affect other processes.

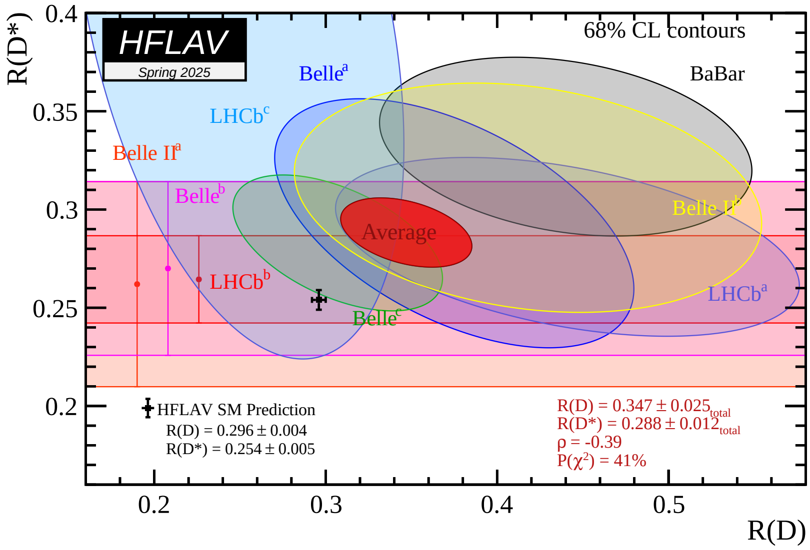

Figure 1.5: Current status of the $R_D^{\tau/\ell}$ and $R_{D^*}^{\tau/\ell}$ measurements, compared to the SM predictions. The contours indicate the 1σ uncertainties. The black dot represents the SM prediction.

The experimental hints are therefore satisfying but not yet conclusive. A definitive interpretation requires:

- Additional measurements with larger datasets and improved control of systematic uncertainties,
- Cross-checks in other decay modes involving third-generation leptons, such as $b \to u\tau^-\overline{\nu}_\tau$.

The possible connection between these anomalies and processes involving τ leptons provides strong motivation for dedicated searches, including the measurement of rare decays involving $b \to u\tau^-\overline{\nu}_\tau$ transitions, such as $B^+ \to \tau^+\nu_\tau$, which is the subject of this thesis.

$B^+ \to \tau^+\nu_\tau$ DECAY The $B^+ \to \tau^+\nu_\tau$ decay is particularly interesting because it is a pure leptonic decay, which means it does not involve any hadronic final states and a precise measurement could be a hint for new physics model which can have a non negligible impact on the decay rate of this phenomenoun. The Feynman diagram with also possible different mediators is shown in Fig. 1.6. The Two Higgs Doublet Model (2HDM) represents a theoretically well-motivated

extension of the SM. It addresses several open questions and allows for a richer phenomenology in the scalar sector. By introducing a second complex scalar $SU(2)_L$ doublet, the model predicts the existence of five physical Higgs bosons: two CP-even neutral scalars (h and H), one CP-odd pseudoscalar (A), and a charged pair (H^+ and H^-), see Ref. [38].
One of the key features of the 2HDM is the potential for new contributions to flavor-changing processes, especially in purely leptonic decays. The interference between the SM and BSM amplitudes can either enhance or suppress the decay rate, depending on the parameters of the model, *e.g.*:

$$\mathcal{B}(B^+ \to \ell^+ \nu_\ell) = \mathcal{B}_{SM} \left(1 - \tan^2 \beta \frac{m_{B^+}^2}{m_{H^+}^2}\right) \tag{1.9}$$

where $\tan \beta$ is the ratio of the vacuum expectation values of the two Higgs doublets, m_{B^+} is the mass of the B^+ meson, and m_{H^+} is the mass of the hypothetical charged Higgs boson. The parameter $\tan \beta$ is a free parameter of the 2HDM, and its value can significantly affect the decay rate. For large values of $\tan \beta$, the charged Higgs contribution can become dominant, leading to a significant enhancement of the branching fraction. On contrary, for small values of $\tan \beta$, the charged Higgs contribution can be negligible, and the decay rate approaches the SM prediction.
Furthermore, other classes of theories beyond the SM, such as various Grand Unified Theories (GUTs), predict the existence of new bosons known as leptoquarks [39]. These hypothetical particles couple simultaneously to a quark and a lepton, and can mediate processes such as $B^+ \to \tau^+ \nu_\tau$ via virtual exchange, as shown if Fig. 1.6b. Leptoquark-induced contributions could alter the observed branching fraction, similarly to the charged Higgs.
Precision measurements of the branching fraction $\mathcal{B}(B^+ \to \tau^+ \nu_\tau)$ at Belle II therefore provide an excellent opportunity to test these BSM scenarios. Any significant deviation from the SM prediction would be a potential indicator of new physics, enabling constraints on the parameter space of models such as the 2HDM and leptoquark frameworks.

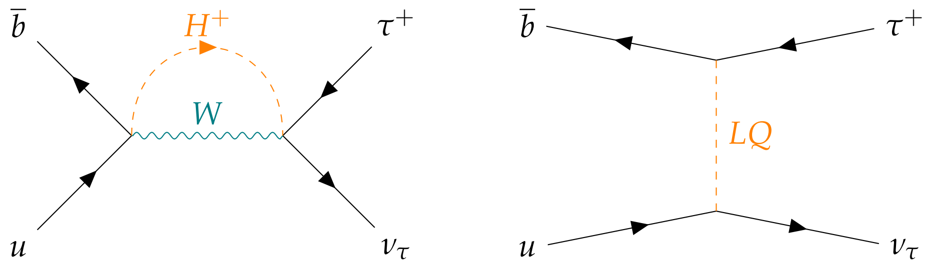

(a) Feynman diagram illustrating the $B^+ \to \tau^+\nu_\tau$ decay, with a SM W^+ or a BSM H^+ as mediator.

(b) Possible Feynman diagram illustrating the $B^+ \to \tau^+\nu_\tau$ decay, with a Lepto-Quark as mediator.

Figure 1.6: Feynman diagrams illustrating the $B^+ \to \tau^+\nu_\tau$ decay. The decay proceeds via the exchange of a virtual W^+ boson, which couples to the b and the u quarks, producing a τ lepton and neutrino. The diagram also shows possible contributions from new physics models, such as the Two Higgs Doublet Model (2HDM) or Lepto-Quark, which can modify the decay rate.

2 THE BELLE II EXPERIMENT

In this chapter the main features of the SuperKEKB accelerator and the Belle II detector are described. The machine upgrade and the physics goals have required a profound transformation to the detector, which had to overcome several technological challenges.
In an electron-positron collider the most efficient way to produce B mesons is to tune the energy to the $\Upsilon(4S)$, the lightest strong resonance with a mass sufficient to decay in b-flavoured mesons ($B^0\overline{B}^0$ or B^+B^- pairs). The beauty meson threshold is at $2m(B) \approx 10.56\,\text{GeV}/c^2$ and $m_{\Upsilon(4S)} \approx 10.58\,\text{GeV}/c^2$. A schematic picture of this process is shown in Fig. 2.1.
In an e^+e^- collider, the study of rare or forbidden decays is ideal, because of the lower track multiplicity compared with the hadron machines (like LHCb), *e.g.* an average $\Upsilon(4S)$ event is characterized only by 11 charged tracks, between pions, kaons and leptons. Moreover the trigger efficiency is higher in this kind of experiments. In this thesis the studied phenomenoun is $B^+ \to \tau^+\nu_\tau$ and the detection of the τ (and all the other missing energy decays) is much easier in a leptonic collision, since the initial energy is known and the number of possible backgrounds is limited. Table 2.1 reports the cross sections of the main phenomena in an e^+e^- collision at this energy.
The branching fraction for the decay of the $\Upsilon(4S)$ into $B\overline{B}$ pair is over 96% [27]. The pair of B mesons are entangled, which implies that from the knowledge

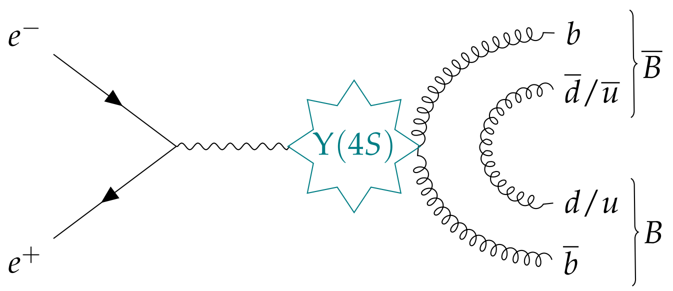

Figure 2.1: Schematic picture of the B meson production in an e^+e^- collision at the $\Upsilon(4S)$ resonance

Table 2.1: e^+e^- main processes

$e^+e^- \to$	Cross Section (nb)
$\Upsilon(4S)$	1.110
$c\bar{c}$	1.30
$u\bar{u}$	1.61
$d\bar{d}$	0.40
$s\bar{s}$	0.38
$\tau^+\tau^-\ (\gamma)$	0.919
$\mu^+\mu^-\ (\gamma)$	1.148
$e^+e^-\ (\gamma)$	≈ 300

of the characteristics of one B it is possible to assign the related features to the second B too, at a certain time t.

2.1 THE SUPERKEKB ACCELERATOR

The Belle II experiment is installed in the interaction point of the SuperKEKB accelerator in Tsukuba, Japan. The machine is currently the only e^+e^- running B-factory in the world with a design luminosity of 6.4×10^{35} cm^{-2} s^{-1} [40]. The essential elements in the increase of the luminosity are a reduction in the beam size at the collision point by a factor of 20 and an increase in the currents by a factor of 2 compared to the KEKB values, where Belle (the predecessor of Belle II) was installed. This is known as a "nano-beam" scheme, and was invented by P. Raimondi for the Italian Super$B$-factory [41]. The reduction of the luminous volume size to about 5% with respect to the predecessor KEKB, combined with doubling of beam currents, is expected to yield a factor 40 gain in intensity (see Fig. 2.2). SuperKEKB is designed to deliver collisions corresponding to 50 ab^{-1} of integrated luminosity, corresponding $\approx 5.3 \times 10^{10}$ of $B\bar{B}$ pairs.
The beam energies bring to the result of the Lorentz boost factor

$$\beta\gamma = \frac{|\vec{p}_{e^+} + \vec{p}_{e^-}|}{\sqrt{s}} \approx 0.28, \tag{2.1}$$

that is around two-thirds of that at KEKB. This condition is advantageous for analyses with neutrinos in the final state that require good detector hermetic-

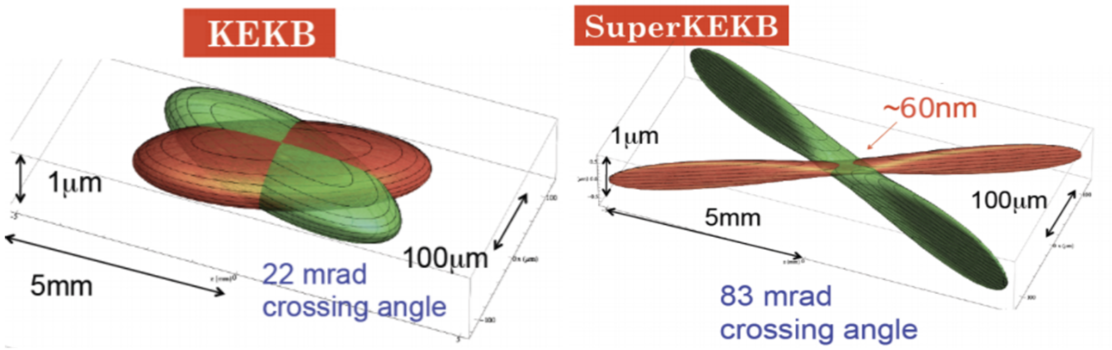

Figure 2.2: Two-dimensional sketch of the nano-beam mechanism implemented in SuperKEKB (right) compared with the previous KEKB collision scheme (left)

Table 2.2: SuperKEKB beam characteristics

	LER(e^+)	HER()	
Energy	4.000	7.007	GeV
Half crossing angle	41.5	41.5	*mrad*
Horizontal emittance	3.2	4.6	*nm*
Emittance ratio	0.27	0.25	%
β functions at IP(x/y)	32/0.27	25/0.30	*mm*
Beam currents	3.6	2.6	
Beam-beam parameter	0.0881	0.0807	

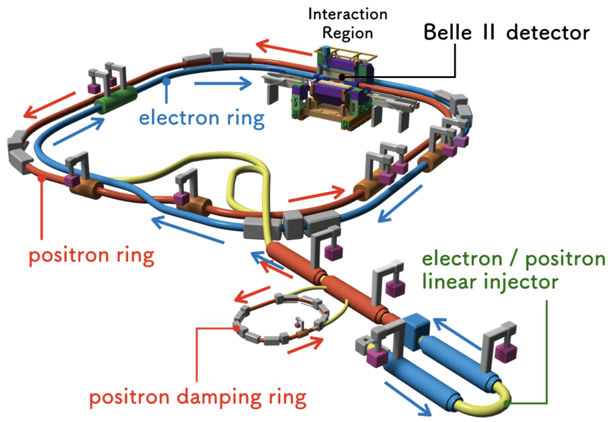

Figure 2.3: SuperKEKB accelerator complex with the upgraded and the new components

ity, but leads also to less separation between the B vertices, in fact the spatial resolution of the Vertex Tracker has to be very precise.
Electrons are produced via photoelectric effect by illuminating a cold cathode with a pulsed laser, then accelerated to 7 GeV with a linear accelerator and injected in the High Energy Ring (HER). Positrons are produced by colliding electrons on tungsten; they are first injected in a damping ring to reduce their emittance, which is the average spread of particles in position and momentum phase-space (a small emittance corresponds to particles confined in a small region and having a similar momentum), then accelerated to 4 GeV with the linear accelerator and injected in the Low Energy Ring (LER). When the circulating beams are sufficiently intense, they are brought to collision in the Interaction Point (IR).

2.1.1 Beam-Induced Background

The characteristics of the beams lead to a non negligible background. The cross section of the background phenomena have been studied and precise predictions are also based on simulated SuperKEKB data.
The background sources are the following:

1. **Touschek effect**: an intra-bunch Coulomb scattering process which deviates the particle energies from nominal values. The scattered particles propagate around the accelerating ring and finally are lost at the beam pipe inner wall, producing a shower. In order to reduce this effect in the

SuperKEKB sub-detectors, in the final section of the beam pipe, collimators and metal shields are located;

2. **Beam gas scattering**: the beam could interact with residual gas molecules in the beam pipe by Bremsstrahlung or elastic scattering. The countermeasures used for Touschek background are efficient also for beam-gas background;

3. **Radiative Bhabha scattering**: the photons could interact with the SuperKEKB magnets producing neutrons by photo-nuclear resonance mechanism. In order to reduce this effect, a neutron shield has been placed close to the detector;

4. **QED processes**: e^+e^- collision could lead to many QED processes, *e.g.* $e^+e^- \to e^+e^-\ e^+e^-$ and the generated particles might spiral inside the detector. Moreover, the accelerating process generate hopelessly synchrotron radiation (from few keV to tens of keV). However, the beam pipe shape is designed to avoid synchrotron radiation photons pass through the detector. Finally, the inner surface of beryllium beam pipe is gold plated to absorb scattered photons. These precautions should completely suppress the synchrotron radiation background.

2.2 OVERVIEW OF THE BELLE II DETECTOR

The Belle II experimental setup is a major upgrade of its predecessor, Belle, and targets more ambitious physics goals. It is a system of multiple subdetectors, each optimized to reconstruct some specific features arranged asymmetrically in concentric layers forming an approximately cylindrical layout around the collision point of the SuperKEKB accelerator. While it is located in the same experimental hall and has a similar design to its predecessor, most of its detectors are new or considerably upgraded. A more efficient charged hadron identification is implemented for increased separation of final-state charged hadrons, reduction of backgrounds, and improved flavor-tagging; a better resolution in the reconstruction of the decay positions (vertices) of long lived particles is achieved, to enhance background suppression and sensitivity in measurements of decay-time dependent quantities; a more hermetic acceptance is achieved thanks to the smaller boost of the center of mass of the collision. These improvements are achieved through technologies designed to sustain the

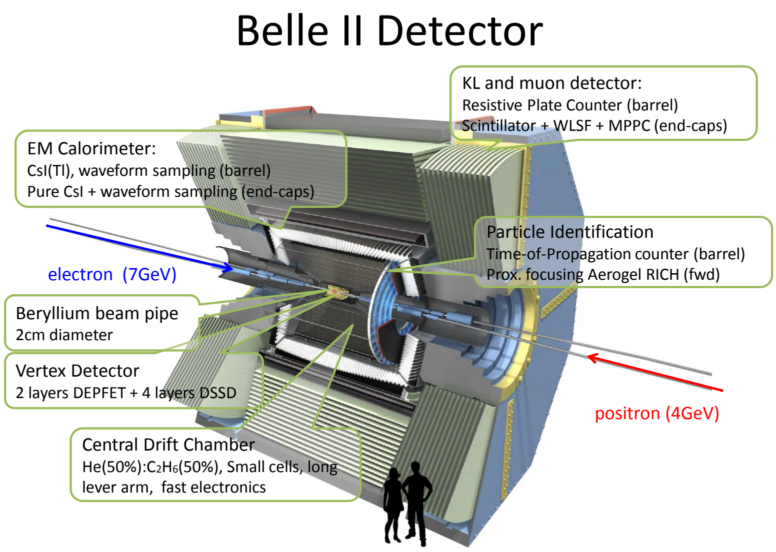

Figure 2.4: Top view of the Belle II detector.

side-effects of higher SuperKEKB instantaneous luminosity.
The main subsystems are shown in Fig. 2.4. They are detailed in next sections and can be broadly classified as follows:

- **Detectors for charged particle tracking**: silicon pixel and strip detectors close to the beam pipe and a wire drift chamber, all immersed in a 1.5 T magnetic field parallel to the beam axis, are used for reconstruction of charged-particle trajectories (tracks).
- **Detectors for particle identification**: Čerenkov radiators, an electromagnetic calorimeter, and scintillators for muon and long-lived neutral hadrons achieve particle identification.
- **Trigger system**: a two-stage trigger is designed to acquire interesting events at the high rates expected at design luminosities.

2.3 TRACKING DETECTORS

The innermost detectors are used for the tracking of charged-particle reconstruction. Effective track reconstruction is of great importance since flavor-physics final states are mostly composed of charged particles and analyses rely

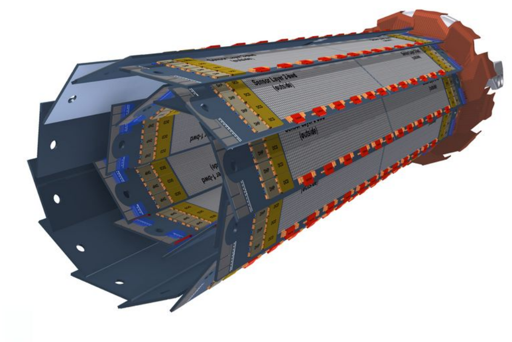

Figure 2.5: Scheme of the PXD detector geometry

strongly on precise measurements of their momenta and the decay positions of their long-lived parent particles, in order to separate signal and background thanks to invariant-mass reconstructed by kinematics variables. Moreover, information on the decay time is key for measurements of CP-violating asymmetries involving mixing, because an entangled state composed by a $B\overline{B}$ pair leads to a same path between the two meson before the decay. To simplify pattern recognition, tracks are first reconstructed in the outer tracking volume, and are then extrapolated into the innermost detector to define coarse regions of interest around their expected intersection points in the inner active layers. If a measurement point is found in the region of interest, the corresponding event is included in the pattern recognition algorithm, otherwise it is not considered.

2.3.1 Silicon-pixel vertexing detector

The innermost detector is a pixel vertexing detector (PXD).
PXD sensors are based on depleted electric field-effect transistor technology. Incident particles generate electron-hole pairs in the depleted region, and thus induce a current. Sensors are 75 μm thick.
The PXD consists of two sets of rectangular layers arranged around the beam pipe with a cylindrical simmetry, at 14 and 22 mm radii and it has a longitudinal dimension of 174 mm at the radius of the outer layer. It comprises around 8 million pixels and the polar acceptance ranges from 17° to 150°.

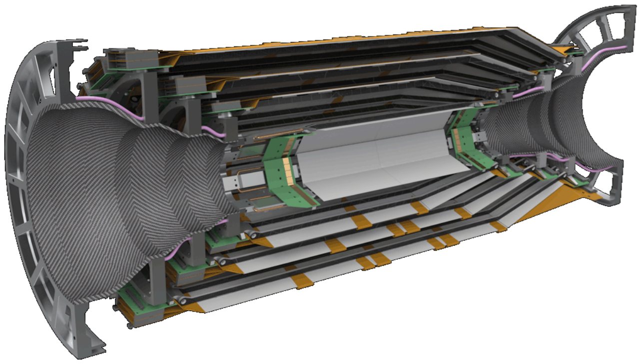

Figure 2.6: Exploded view of a SVD detector half

2.3.2 Silicon-microstrip vertexing detector

A little outer the PXD there is the SVD (Ref. [42]), a silicon detector with the goal to reconstruct decay vertices and charged-particle tracks at high spatial resolution.
SVD uses double-sided silicon strips. Each sensor is a classic photodiode, hence traversing charged particles ionize the silicon, freeing electron-hole pairs that drift due to the electric field, and induce a signal in the electrodes. The fine segmentation of SVD sensors reduces the dead time of the detector, to deal with the high expected rates.
As shown in Fig. 2.6, SVD has a cylindrical asymmetric geometry that mirrors the asymmetry due to the center-of-mass boost. The polar acceptance ranges from 17° to 150°. SVD is radially structured into four concentric layers at 39, 80, 104, and 135 mm, composed by, respectively, 7, 10, 12, and 16 independently readout modules. Sensors are 300 μm-thick, and the separation between adjacent sensing strips ranges from 50 to 240 μm. Hence, the spatial resolution varies with the polar angle. Since the charge associated with an incident particle is usually distributed among several strips, position resolution is improved by interpolation.

2.3.3 Central drift chamber

The CDC is a drift chamber, hence its objective is to identify particles by measuring their specific-ionization energy-loss. It samples charged-particle trajectories at large radii, thus providing trigger signals for events containing charged particles. The CDC has a hollow cylindrical geometry with radii be-

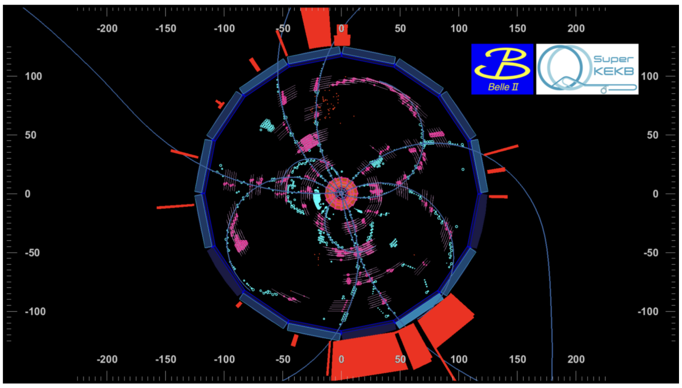

Figure 2.7: Example of event display of a typical hadronic event at Belle II. Curved tracks are reconstructed in the CDC

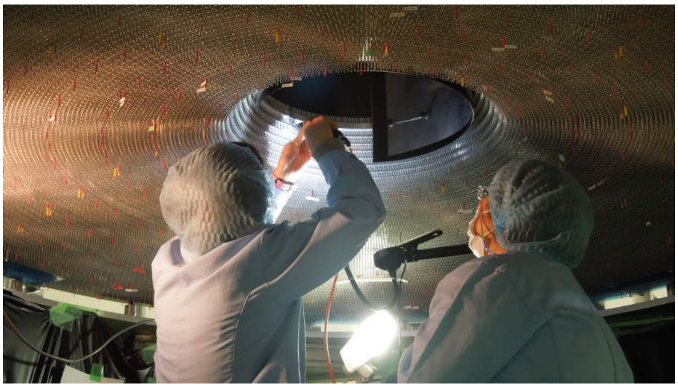

Figure 2.8: Testing of the inner CDC wires before installation. The wires are arranged in a cylindrical geometry, with the inner wires at 16 cm radius and the outer wires at 113 cm radius.

tween 16 cm and 113 cm. The chamber is composed of 14336 sense wires, divided in 56 layers, immersed in a gaseous mixture of 50% He and 50% C_2H_6, while 42240 aluminum wires shape the electric field. The azimuthal acceptance ranges from 17° to 150°.

The single hit has an about 100 μm spatial resolution and the energy resolution is 11.9% for an incident angle of 90°. Figure 2.7 shows a reconstructed hadronic event in the CDC. The transverse momentum resolution is $\sigma(p_T)/p_T^2 \approx 0.5\%/\text{ GeV }/c$. A picture of the chamber installation is shown in Fig.2.8.

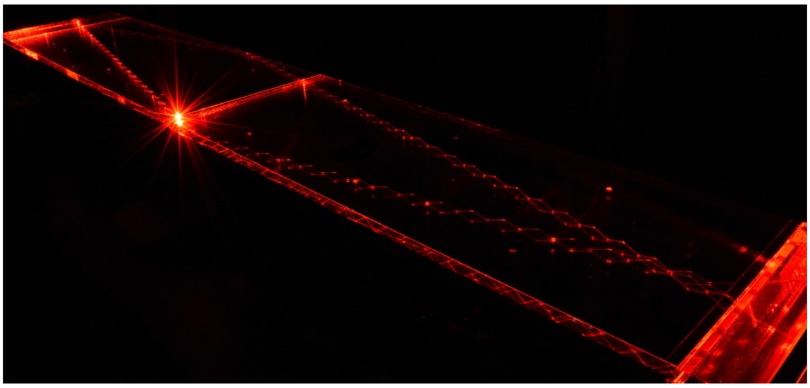

Figure 2.9: Internal reflection of a laser inside one of the 16 bars of the TOP detector.

2.4 PARTICLE-IDENTIFICATION DETECTORS

Charged particle identification in the Belle II experiment is characterized by by two detectors: the time of propagation counter (TOP) and the aerogel ring-imaging Čerenkov counter (ARICH). Their principle is the same: the Čerenkov light. Particle-identification information is also provided by the electromagnetic calorimeter (ECL) and the K_L^0 and muon detector (KLM).

2.4.1 Time of propagation counter

The TOP counter is located in the barrel region. It measures the time of propagation of the photons produced by charged particles with Čerenkov effect. A three-dimensional image of the cone is reconstructed using the correlation between hits positions in the $x - y$ plane and time of propagation. The TOP consists of 16 quartz bars mounted on the barrel at $1.2\,m$ radius from the interaction point. Each bar is a photon radiator and has three main components (Fig. 2.9): a long section where Čerenkov radiation happens; a spherical mirror mounted on the forward end, which focuses the light; and a prism, mounted on the backward end of the bar, which collects and guides the photons to a photomultiplier.
The polar angular acceptance ranges from $31°$ to $128°$. The single-photon time resolution is about $100\,ps$, providing a good separation of pions and kaons with momentum between $0.4\,\text{GeV}/c$ and $4\,\text{GeV}/c$ (kaon identification efficiency is about 95%, pion fake rate is about 10%). This time resolution is achieved with a photo-multiplier specially developed for this purpose.

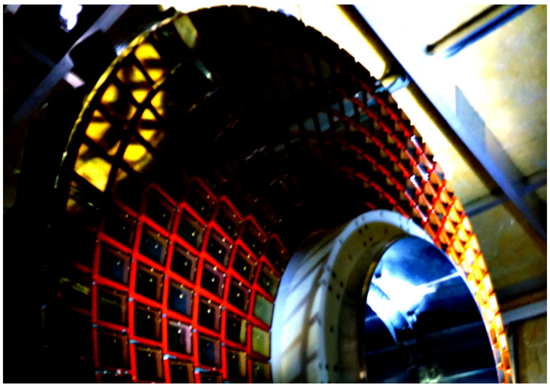

Figure 2.10: Picture of the ARICH before installation.

2.4.2 Aerogel ring-imaging Čerenkov

K/π separation is also provided by ARICH counter, which measures the Čerenkov ring produced by the passage of charged particles through a radiator. The ARICH provides not only discrimination between pions and kaons, but also discrimination between pions, muons, and electrons below 1 GeV /c. When charged particles pass through the aerogel radiator, Čerenkov photons are produced; they propagate in a expansion volume where they form a ring on a photo-diodes surface. Two aerogel radiators with different refraction indexes are used to increase the number of generated photons without degrading the Čerenkov-angle resolution.
The ARICH is composed of 420 modules for photon detection arranged in seven layers extending from 0.41 to 1.14 m radii, and by 248 aerogel tiles placed on the detector endcaps. The polar angular acceptance ranges from 14° to 30°. The observed ARICH performances allows for a 5σ separation between 0.4 and 4 GeV /c momenta kaons and pions, and a 4σ separation between pions, muons and electrons slower (momenta smaller than 1 GeV /c).

2.5 ELECTROMAGNETIC CALORIMETER

The electromagnetic calorimeter (ECL) is the end of the path for photons and electrons. This characteristic allows the ECL to detect photons over a wide energy range as well as to identify electrons and separate them from hadrons. These cluster are related a posteriori with the CDC tracks. The ECL is a highly-segmented array of thallium-doped and cesium iodide crystals. To improve

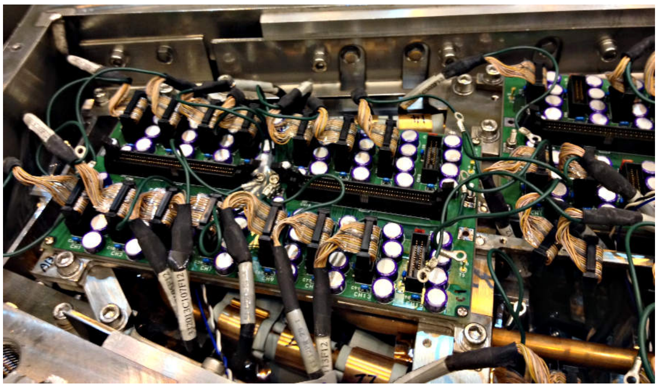

Figure 2.11: A section of the ECL endcap electronics. The visible boards route signals from the preamplifiers (not shown) to the cables leading to the ShaperDSP modules. Cooling lines are also visible beneath the boards.

the probability to emit a photon in the visible, Thallium impurities are added to create other energy level, in which the electrons can "jump". The scintillation light is then collected by phototubes. The $CsI(Tl)$ crystals offer a good time resolution, which reduces the contamination of beam-background photons, which are not in time with the collision products. In the ECL, photons and electrons are identified through their kinematics, shower shapes and timing information, as they have different (in shape and magnitude) energy losses with respect to charged hadrons. To separate electrons from photons, information from tracking detectors is correlated with the ECL signal. The ECL consists of a 3- m-long barrel section with an inner radius of 1.25 m. The polar angle coverage ranges from 12.4° to 155.1°, with two holes between 31.4° to 32.2° and 128.7° to 130.7°. The energy resolution ranges from $\sigma_E/E = 4\%$ at 100 MeV to $\sigma_E/E = 1.6\%$ at 8 GeV. The observed resolution for the reconstructed π^0 mass is 8 MeV. The ECL also allows for determining luminosity by measuring the Bhabha scattering rate and using its precisely known cross-section.

2.6 K_L^0 AND MUON DETECTION SYSTEM

The KLM detects muons and neutral particles, because most of the particles get absorbed before the last step of the Belle II experimental setup. It is made of alternating iron plates and active detector elements, this kind of detector is called "sampling calorimeter", because has active and inactive components. Iron elements act also as magnetic flux returns for the tracking solenoid. In the inner layers, the active material is scintillator, while in the outer layers are resistive plate chambers (RPC), with a gas mixture filling the space between electrodes. When particles traverse the KLM, they produce charges that are collected by applying an appropriate voltage. The barrel section of the detector covers 45° to 129° in polar angle. The endcaps cover 25° to 40° and 129° to 155°. Design reconstruction efficiency exceeds 80% for muons with momentum greater than 1 GeV /c and K^0_L with momentum greater than 3 GeV /c.

2.7 TRIGGER SYSTEM

The Belle II trigger system covers a very important role to reject background events and accept event of interest during data taking. The bunch crossing time is about 4 ns and it is much faster than the detectors signal collection time, so the beam can be considered continuous. Anyway, at full luminosity, the expected event rate is about 50 kHz, and over than 90% of these events are Bhabha scattering or 2γ QED processes (the Bhabha cross section is about 300 times greater than the resonance).
Despite $B\bar{B}$ events are characterized by a higher charged track multiplicity with respect to others events, this variable can not be used in the trigger because τ and low multiplicity events would be discarded too. The required trigger must have instead an efficiency close to 100% for $B\bar{B}$ events, since B forbidden or rare decays are one of the main studied physics phenomena. Some efficiency degradation is allowed to suppress the Bhabha and 2γ QED backgrounds. The trigger rate must be below 30 kHz, the maximum acquisition frequency of DAQ, and the trigger must provide time information with a precision below 10 ns to exploit the potential of the Belle II sub-detectors.
The Belle II trigger is composed in two main stages: a hardware trigger or Level 1 trigger (L1) and a software trigger or High Level Trigger (HLT). The first one removes most of the background events with the help of the faster sub-detectors (frequency higher than 30 kHz), while the second one refine the selection with a more exhaustive analysis and reduce the event rate from L1 trigger to a storable rate of 10 kHz.

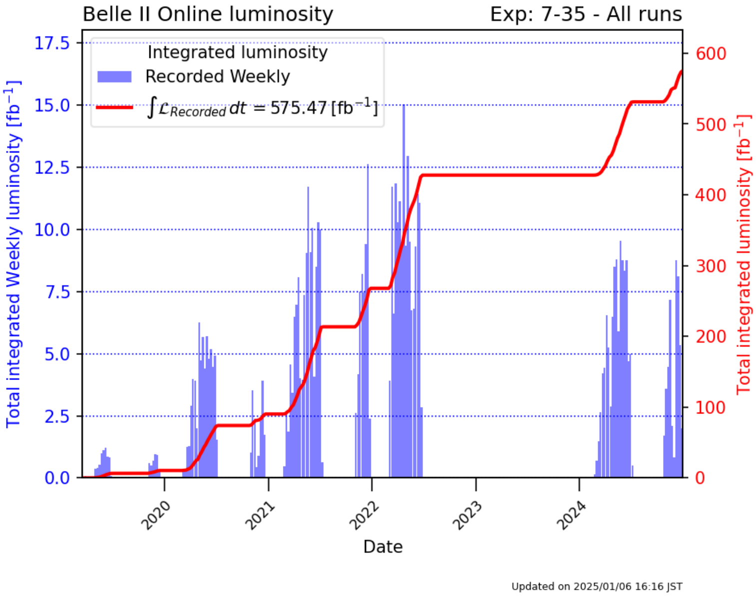

Figure 2.12: Integrated luminosity collected by Belle II as a function of time, showing contributions from Run1 (2019-2022) and Run2 (2024-...).

2.8 DATA TAKING

Physics data taking for Run1 began in the spring of 2019 and concluded on June 2022, after which operations paused for a scheduled program of maintenance and upgrades to both the detector and the accelerator. During Run1, SuperKEKB achieved a record instantaneous luminosity of $4.7 \times 10^{34}\, cm^{-2}\, s^{-1}$, and Belle II recorded an integrated luminosity of $424\, \text{fb}^{-1}$. These data provide large samples of beauty and charm hadrons, as well as τ leptons, enabling a broad physics program including unique searches for dark-matter-related particles.

Data taking resumed in 2024 following the long shutdown. In December 2024, SuperKEKB set a new world record for instantaneous luminosity at $5.1 \times 10^{34}\;\; cm^{-2}\, s^{-1}$, and the total integrated luminosity collected by Belle II reached $575\, \text{fb}^{-1}$, until December 2024.

Figure 2.12 shows the integrated luminosity collected by Belle II as a function of time, highlighting the significant contributions from both Run1 and the ongoing Run2.

In order to produce B mesons, it is necessary to collide electrons and positrons at a center-of-mass energy corresponding to the mass of the $\Upsilon(4S)$ resonance,

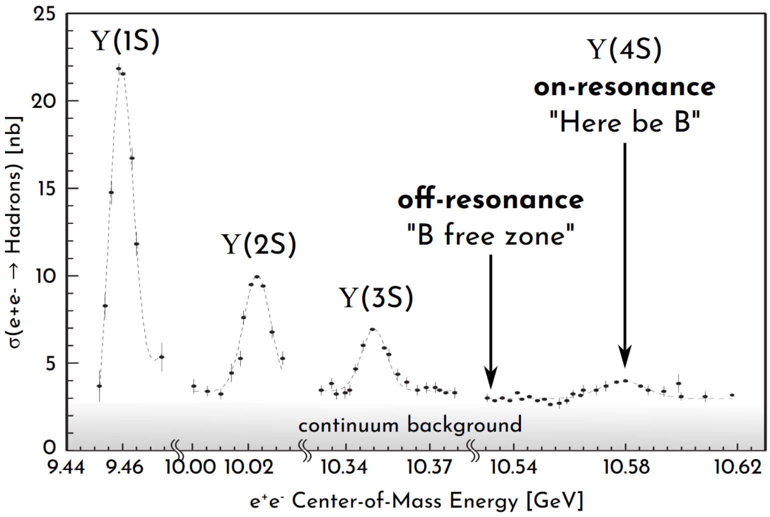

Figure 2.13: Cross section of the $e^+e^- \to \Upsilon(nS)$ process, showing the peak at 10.58 GeV and the off-resonance region at 10.52 GeV.

i.e. 10.58 GeV $/c^2$. This is the primary operational mode of the SuperKEKB accelerator and the main data-taking configuration for the Belle II experiment. Figure 2.13 shows the different cross section around the Υ resonances showing the difference between on- and off-resonance.
However, SuperKEKB is capable of operating at a range of energies, allowing the collection of several distinct types of datasets, each serving specific physics goals and calibration needs:

- **On-resonance:** the standard data-taking mode, in which the beams are tuned to collide at the $\Upsilon(4S)$ resonance energy. This maximizes the production of $B\bar{B}$ pairs, which are essential for the core physics program of Belle II, including studies of CP violation, rare decays, and searches for new physics.

- **Off-resonance:** data collected at an energy approximately 60 MeV below the $\Upsilon(4S)$ resonance, where the production of B mesons is kinematically forbidden. These datasets are crucial for characterizing and subtracting non-resonant background processes, such as continuum $q\bar{q}$ production, in analyses of on-resonance data.

- **Cosmic runs:** data acquired using cosmic-ray muons, independent of beam collisions. These runs are primarily used for detector calibration, alignment, and performance studies, as cosmic muons provide a clean and well-understood source of charged particles traversing the detector.

- **Beam runs:** special runs dedicated to studying backgrounds induced by the accelerator beams themselves, such as beam-gas interactions and synchrotron radiation. These datasets are essential for understanding and mitigating beam-related backgrounds that can affect detector performance and data quality.

- **Energy scans:** short data-taking periods in which the center-of-mass energy is varied in small steps around the $\Upsilon(4S)$ resonance. These scans are performed to precisely measure the resonance line shape, determine the cross section as a function of energy, and search for possible exotic vector resonances.

- **Non-$\Upsilon(4S)$ datasets:** data collected at energies significantly above or below the $\Upsilon(4S)$ resonance. These datasets are used for a variety of studies, including spectroscopy of other bottomonium states, investigations of hadronic physics, and searches for phenomena related to the dark sector.

This flexible data-taking strategy enables Belle II to address a broad range of physics topics, from precision measurements in the B meson system to exploratory searches for new particles and interactions. The projection of the Belle II experiment is to collect a total integrated luminosity of $50\,\mathrm{ab}^{-1}$, which will significantly enhance the statistical power of analyses and the sensitivity to rare processes. The projection plot is shown in Fig 2.14, illustrating the expected increase in integrated luminosity over the coming years.

2.9 MONTE CARLO EVENT GENERATION AND DETECTOR SIMULATION

In high-energy physics experiments, it is crucial to compare the recorded data with the corresponding theoretical expectations. While in extremely rare cases a discovery may be evident without requiring a detailed comparison, for example, the observation of the J/ψ resonance, most measurements demand careful validation to ensure that the observed features are not artifacts of the complex experimental apparatus.
To facilitate this comparison, simulated events are generated to emulate the behavior of particles in the real detector as accurately as possible. This is achieved using repeated sampling of random variables, a technique commonly referred

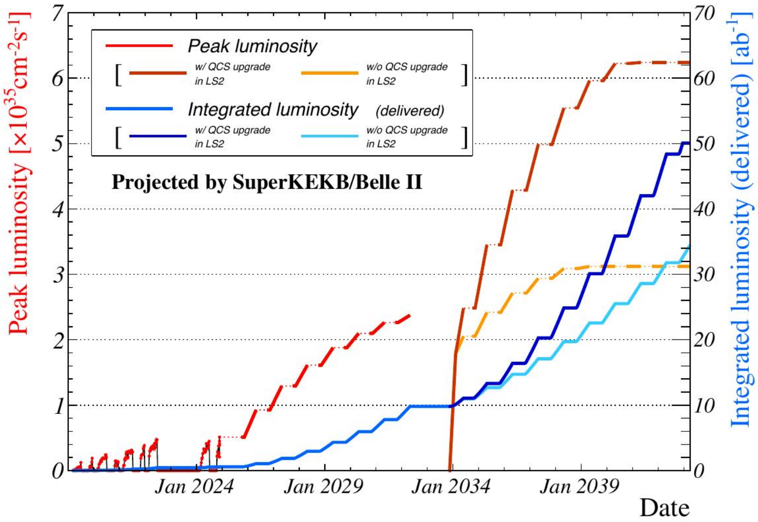

Figure 2.14: Projected integrated luminosity for the Belle II experiment, showing the expected increase over the next years as the experiment continues to collect data.

to as the *Monte Carlo method* [43]. The entire simulation workflow is typically abbreviated as MC.
The Monte Carlo workflow can be conceptually divided into two main components:

1. **Event Generation**: which describes the underlying physics processes.
2. **Detector Simulation**: which models the response of the detector to the generated particles.

The first stage of the simulation process involves generating the physics interaction to be studied. Given the initial conditions of the colliding particles, such as an e^+e^- interaction, we simulate the production of secondary particles according to a given theoretical model. This model could be based on the SM, or it could involve extensions such as supersymmetry or dark sector particles, like axion like particle (ALP) or Z'.
The specific choice of event generator depends on the analysis goals. For instance:

- **Signal MC** simulates the decay mode under investigation.
- **Generic MC** represents inclusive SM processes for comparison.

- **Background MC** is used to simulate and study processes that may mimic the signal and must be excluded.

In all cases, the generator produces the four-momenta and vertex positions of all particles involved. Within Belle II, this step is computationally efficient, typically requiring only a few milliseconds per event.
Several generators are available for specific physics processes. The $B\bar{B}$ samples are generated with EvtGen [44]. Continuum $e^+e^- \to q\bar{q}$ ($q = u, d, s, c$) and $e^+e^- \to \tau^+\tau^-$ events are generated with KKMC [45]. The fragmentation of $q\bar{q}$ uses Pythia8 [46], and τ decays are simulated by Tauola [47]. Final state radiation is simulated by Photos [48, 49]. Following event generation, the particles must be propagated through a virtual representation of the detector to simulate how they would interact with the detector material. This includes modeling electromagnetic and hadronic interactions such as ionization, scintillation, bremsstrahlung, pair production, and Čerenkov radiation.
These processes are well understood and can be modeled accurately using dedicated simulation software. Belle II uses the Geant4 toolkit [50], a widely adopted software package developed to simulate the passage of particles through matter. Geant4 propagates the generated particles through a geometrical model of the Belle II detector, simulating their interactions with detector components. The resulting output consists of energy depositions and secondary particles created in each subdetector. Custom Belle II software modules then translate this output into simulated detector signals. For instance, the pixel detector module converts deposited energy into the corresponding fired pixels.
While event generation is relatively fast, full detector simulation is computationally intensive. A single Belle II event takes approximately one second to simulate. In high-energy experiments like ATLAS or CMS, this can extend to several minutes per event due to the increased event complexity.
A more detailed description of the Monte Carlo simulation workflow and the specific types of MC samples produced at Belle II is provided in Appendix B.
During my Ph.D., I was responsible for generating the MC simulated samples for the collaboration.

2.10 DISCREPANCIES BETWEEN SIMULATION AND REAL DATA

Despite the accuracy of modern simulation tools, differences between simulated and real detector data inevitably arise. GEANT4 operates on an idealized detector geometry, whereas the real Belle II detector is a massive, highly intricate system, built from thousands of components with micrometer-level precision.

Uncertainties in the exact composition and location of each material component (*e.g.*, screws, cables) limit the fidelity of the simulation. Modeling every detail would also drastically increase the computational load, rendering the simulation impractical.

As a result, simplifications are necessary. These approximations must be minimized, especially during the early phases of the experiment, when the detector response is still being characterized. Ongoing work by the Belle II Performance Group focuses on understanding and reducing these differences through dedicated calibration campaigns and validation studies.

3 RECONSTRUCTION AND CUT-BASED EVENT SELECTION

In my Ph.D. research, I measured the branching fraction ($\mathcal{B}$) of the $B^+ \to \tau^+ \nu_\tau$ decay using data collected by the Belle II experiment at the SuperKEKB electron-positron collider. The dataset, recorded between 2019 and 2022 at a center-of-mass energy of $10.58\,\mathrm{GeV}/c^2$ (corresponding to the $\Upsilon(4S)$ resonance), corresponds to an integrated luminosity of $365\,\mathrm{fb}^{-1}$, or $(387 \pm 6) \times 10^6$ $\Upsilon(4S)$.
This chapter describes the procedures for event reconstruction and selection. The first part of the reconstruction is done via a hadronic tag, explained in Sec. 3.3 and more in detail in App. A. The $B^+ \to \tau^+ \nu_\tau$ signal is identified through the 1-prong decay modes of the τ^+ lepton, specifically: $\tau^+ \to e^+ \, \nu_e \, \overline{\nu}_\tau$, $\tau^+ \to \mu^+ \, \nu_\mu \, \overline{\nu}_\tau$, $\tau^+ \to \pi^+ \, \overline{\nu}_\tau$, and $\tau^+ \to \rho^+ \, \overline{\nu}_\tau$ with $\rho^+ \to \pi^+ \, \pi^0$. Table 3.1 reports the τ branching fractions. Figure 3.1 illustrates the targeted signal event.

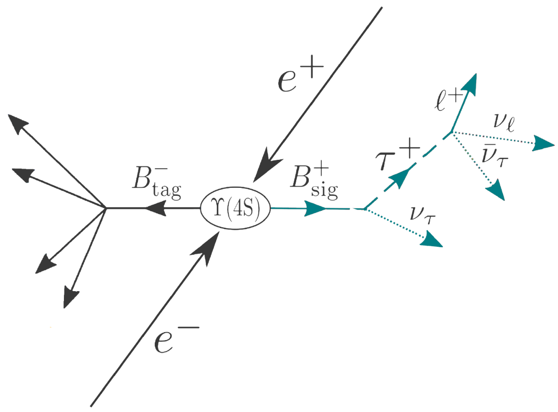

Figure 3.1: Sketch of the $B^+ \to \tau^+ \nu_\tau$ decay. First, a hadronic B decay is reconstructed on the tag side. The other B is searched using the 1-prong decays of the τ lepton. We require no extra charged tracks from the Interaction Point (IP).

Table 3.1: Branching fractions of the main 1-prong τ decay modes used in this analysis [22]

$\tau \to$	$\mathcal{B}(\%)$
$e^+ \nu_e \overline{\nu}_\tau$	17.82 ± 0.04
$\mu^+ \nu_\mu \overline{\nu}_\tau$	17.39 ± 0.04
$\pi^+ \overline{\nu}_\tau$	10.82 ± 0.05
$\rho^+ \overline{\nu}_\tau$	25.49 ± 0.09

3.1 COMPUTING ENVIRONMENT

The Belle II collaboration developed a dedicated tool, the Belle II Analysis Framework (`basf2`) [51], to process the data. Raw data from the detector are calibrated, reconstructed, and stored in PANTHER-based data summary tape (DST) files, a custom serialization format [52]. After each experiment, calibration constants are updated and stored in the Belle II Condition Database, and data are reprocessed into a compact, compressed format known as mDST files in ROOT [53] format. `basf2` is responsible for handling the reconstruction and processing of mDST files.
`basf2` is written in C++ and PYTHON [54], and incorporates third-party libraries such as EVTGEN, GEANT4, and ROOT, a modular scientific software developed by CERN that offers extensive functionality for handling large datasets. It is structured into packages, each covering a different aspect of data processing: data acquisition, Monte Carlo event generation, detector and sub-detector simulation, track reconstruction, event visualization within the detector, and physics analysis. These packages contain libraries, modules, and data objects. Libraries, implemented in C++, provide shared functionality across modules. Modules are small, self-contained processing blocks built on top of these libraries, working event by event to complete specific tasks. A series of modules forms a processing chain, or "path", with data objects (*e.g.*, `Track`, `ECLCluster`, `Particle`, and `ParticleList`) stored in a common DataStore accessible to all modules. `basf2` users provide a PYTHON-based steering file to manage this workflow.
After the data processing and the MC simulation production, the final mDST files are read and analyzed using ROOT. Additionally, PYTHON and specialized libraries such as NUMPY [55], SCIPY [56], SCIKIT-LEARN [57], and MATPLOTLIB [58] are employed for implementing machine learning algorithms and generating plots.

Table 3.2: Categories of simulated events, integrated luminosity, and breakdown of signal and background categories. In the $e^+e^- \to \to B^+B^-$ background simulation, the signal contribution is excluded.

Simulated Categories	Int. Lum.(fb^{-1})
$B^+ \to \tau^+\nu_\tau$	324525
$e^+e^- \to \Upsilon(4S) \to B^+B^-$	2800
$e^+e^- \to \Upsilon(4S) \to B^0\bar{B}^0$	2800
$e^+e^- \to u\bar{u}$	1000
$e^+e^- \to d\bar{d}$	1000
$e^+e^- \to c\bar{c}$	1000
$e^+e^- \to s\bar{s}$	1000
$e^+e^- \to \tau^+\tau^-$	600

3.2 DATASET

The data were organized into 10 different channels: 8 containing MC simulations of the primary physics processes and 2 with experimental data from Belle II (on- and off-resonance). The simulated event categories are listed in Tab. 3.2, with the generated equivalent luminosity.
To assess the sensitivity of the Belle II experiment in detecting $B^+ \to \tau^+\nu_\tau$ decays, each MC sample was normalized to match the data luminosity of $365\,\mathrm{fb}^{-1}$.

3.3 FULL EVENT INTERPRETATION AND TAGGING

A multivariate tagging method, known as the Full Event Interpretation (FEI), is used to identify signal events by fully reconstructing one of the B mesons in each event (the B_{tag}), defining the *tag-side*. The remaining particles are then analyzed on the recoil, which is defined as the *signal-side*.
The FEI algorithm, a component of the `basf2` software package, is implemented in Python and is responsible for:

- reconstructing user-defined multi-level decay topologies;
- training interdependent multivariate classifiers (MVCs) for each decay channel;

- setting channel-specific pre-cuts and particle-specific post-cuts to manage combinatorics;
- generating a report summarizing key performance metrics and control plots for each decay channel and particle used.

Users define the reconstructed decay topology, along with the methods and variables for multivariate classification. The FEI reconstructs one of the two B mesons from $\Upsilon(4S)$ decays to gain information about the other B meson. Three distinct tagging methods exist:

- **Hadronic tagging**: reconstructs hadronic decay channels, yielding precise kinematics and the purest sample, though with low tagging efficiency.
- **Semileptonic tagging**: uses semileptonic decay channels, which offer higher tagging efficiency but less purity due to missing kinematic information from neutrinos.
- **Inclusive tagging (no-tagging)**: combines four-momenta of all particles directly for the desired signal, achieving higher tagging efficiency but with high background and low purity.

The first two are included in the FEI algorithm. The FEI automatically constructs plausible B_{tag} decay chains compatible with observed tracks and clusters. It estimates the likelihood of each decay chain representing the true process using gradient-boosted decision trees. The process begins with reconstructing final-state particles, training MVCs using detector data. Intermediate particle candidates are then reconstructed, and MVCs are trained per decay channel. Finally, B candidates are reconstructed, and classifiers are trained, resulting in four particle lists: B^+ (hadronic and semileptonic) and B^0 (hadronic and semileptonic). The candidate with the highest FEI discriminant is chosen for analysis, and here, the hadronic tagging method is used.
Additionally, two kinematic variables help to distinguish correctly reconstructed B_{tag} candidates from mis-reconstructed events: the beam energy-constrained mass $M_{bc} = \frac{1}{c^2}\sqrt{s/4 - p_B^2 c^2}$ and the energy difference $\Delta E = E_B - \sqrt{s}/2$, where $\sqrt{s}$ is the total energy in the $\Upsilon(4S)$ center-of-mass system (CMS), and p_B and E_B represent the momentum and energy of the B_{tag} candidate in the CMS. Signal events with correctly reconstructed B_{tag} and background events from $\Upsilon(4S) \rightarrow B^+B^-$ are characterized by an M_{bc} distribution peaked at the

B meson mass (Fig. 3.2). Continuum backgrounds ($e^+e^- \to q\bar{q}$ for $q = u, d, c, s$) and mis-reconstructed combinatorial backgrounds exhibit a smooth M_{bc} distribution.
To reduce the number of B_{tag} candidates, a loose pre-selection is applied:

- $M_{bc} > 5.24\,\text{GeV}/c^2$;
- $-300 < \Delta E < 300\,\text{MeV}$;
- $\mathcal{O}_{\text{FEI}} > 0.001$.

Approximately 0.30% of $\Upsilon(4S)$ events have a correctly reconstructed B_{tag} candidate with a purity of 29%.

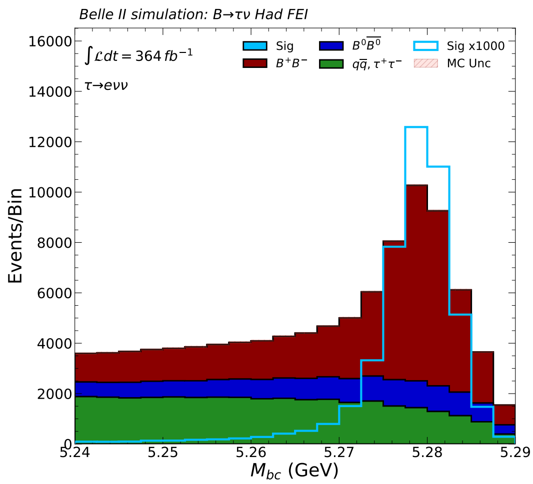

Figure 3.2: Plot of M_{bc} for the e channel with loose pre-selection applied; similar distributions are observed for the μ, single π, and ρ channels.

More details on the FEI algorithm are provided in App. A.

3.4 SIGNAL PRE-SELECTION CRITERIA

In events where a B_{tag} is reconstructed, we require exactly one additional oppositely charged track, consistent with a 1-prong τ decay mode (`good-track`). A `good track` is defined as a track meeting the following criteria: `dr` $< 0.5\,cm$, $|$`dz`$| < 2\,cm$, θ within the CDC acceptance range ($0.297 < \theta < 2.67$), and momentum $p > 0.5\,\text{GeV}/c$.
Additionally, we enforce that the Rest of Event (ROE), defined as everything

not associated with the B_{tag} and B_{sig}, contains no `ROE tracks`. A `ROE track` is any track in the ROE satisfying $\texttt{dr} < 0.5\,cm$, $|\texttt{dz}| < 2\,cm$, and θ within the CDC acceptance range.

For charged particle identification (PID), we use both likelihood-based and machine learning-based selectors. Detector system information, including specific ionization ($\mathrm{d}E/\mathrm{d}x$) from the SVD and CDC, E/p from the ECL, and measurements from the TOP, ARICH, and KLM is analyzed independently to determine both a likelihood and a machine learning classifier for each charged particle type (electron, muon, pion, kaon, proton, and deuteron). Specifically, likelihoods from each detector are combined to form a likelihood ratio:

$$\frac{\mathcal{L}(\text{particle})}{\mathcal{L}(e) + \mathcal{L}(\mu) + \mathcal{L}(\pi) + \mathcal{L}(K) + \mathcal{L}(p) + \mathcal{L}(d)}. \tag{3.1}$$

Particle identification criteria are then applied to select specific τ decay modes:

- $\tau^+ \to \boldsymbol{e}^+ \nu_e \, \overline{\nu}_\tau$, machine learning-based
- $\tau^+ \to \boldsymbol{\pi}^+ \overline{\nu}_\tau$, likelihood-based
- $\tau^+ \to \rho^+ \, \overline{\nu}_\tau$ with $\rho^+ \to \boldsymbol{\pi}^+ \pi^0$, likelihood-based

The selected decay categories collectively account for approximately 71.5% of all τ decays.

For the $e^+ \, \nu_e \, \overline{\nu}_\tau$ mode, tracks are identified as electron candidates if they satisfy $\texttt{electronID} > 0.9$. For the $\mu^+ \, \nu_\mu \, \overline{\nu}_\tau$ mode, tracks that do not pass the `electronID` selection but meet $\texttt{muonID} > 0.9$ are considered muon candidates. For the $\pi^+ \, \overline{\nu}_\tau$ and $\pi^+ \, \pi^0 \, \overline{\nu}_\tau$ modes, tracks that satisfy $\texttt{pionID} > 0.6$ are selected as pion candidates.

These PID selection criteria achieve electron, muon, and pion identification efficiencies of 99%, 82%, and 97%, respectively, with corresponding misidentification rates of 1%, 5%, and 9%. When multiple candidates satisfy the selection criteria, only the candidate with the highest PID score is retained. For the $\pi^+ \, \pi^0 \, \overline{\nu}_\tau$ mode, a single π^0 candidate is reconstructed by pairing two ECL neutral clusters not associated with the B_{tag} candidate. These clusters must pass photon quality requirements and satisfy the invariant mass constraint $120 < m_{\gamma\gamma} < 145\,\text{MeV}/c^2$ for the $\gamma\gamma$ pair. Additionally, the $\pi^+ \, \pi^0$ invariant mass is required to satisfy $625 < m_{\pi^+\pi^0} < 925\,\text{MeV}/c^2$. When multiple candidates fulfill these requirements, the candidate with an invariant mass closest to the nominal ρ mass is selected.

ECL neutral clusters not associated with the B_{tag} are further processed to remove fake clusters originating from beam-induced background, from hadronic

Table 3.3: Signal pre-Selection criteria and ECL cluster clean-up

Particles	Selections
good track	`dr` $< 0.5\,cm$, $\lvert$`dz`$\rvert < 2\,cm$, $p > 0.5\,\text{GeV}/c$, $E < 5.5\,\text{GeV}$
e^+ μ^+ π^+	good track, $eID > 0.9$ good track, $\mu ID > 0.9$ good track, $\pi ID > 0.6$
π^0 ρ^+	$120 < m_{\gamma\gamma} < 145\,\text{MeV}/c^2$ $625 < m_{\pi^+\pi^0} < 925\,\text{MeV}/c^2$
γ (from π^0)	$N_{\text{hit,ECL}} > 1.5$, θ in the CDC acceptance $E_\gamma > 80\,\text{MeV}$ $(0.8536 < \cos\theta < 0.9563)$ $E_\gamma > 30\,\text{MeV}$ $(-0.6252 < \cos\theta < 0.8462)$ $E_\gamma > 60\,\text{MeV}$ $(-0.8660 < \cos\theta < -0.6521)$
ROE tracks (=0)	`dr` $< 0.5\,cm$, $\lvert$`dz`$\rvert < 2\,cm$, θ in CDC acceptance
ROE γ	$E > 55\,\text{MeV}$ and `clusterNHits` > 1.5 `beamBackgroundSuppression` > 0.5 `fakePhotonSuppression` > 0.05

split-off, and neutral hadrons. This is achieved using two distinct Multivariate Algorithms (MVAs), `beamBackgroundSuppression` and `fakePhotonSuppression`, trained on a $B^0 \to \bar{D}^* \ell^+ \nu_\ell$ control sample. Requirements for all ECL neutral clusters include: number of hits in ECL, $N_{\text{hit,ECL}} > 1.5$; θ within the CDC acceptance; and specific minimum cluster energies: $E_\gamma > 100\,\text{MeV}$ in the forward region of the Belle II detector, $E_\gamma > 55\,\text{MeV}$ in the barrel region, and $E_\gamma > 80\,\text{MeV}$ in the backward region. All remaining clusters form the *Rest of the Event*, which is fundamental for constructing $E_{\text{ECL}}^{\text{extra}}$.
All the criteria defining the signal preselection are summarized in Tab.3.3.

3.5 CUT-BASED CONTINUUM REJECTION

Event shape variables, quantities related to the momentum and weighted spatial distribution of all particles in the detector are essential for discriminating between continuum and $B\bar{B}$ events. Continuum events typically exhibit a pronounced back-to-back topology, whereas $B\bar{B}$ events are characterized by a more

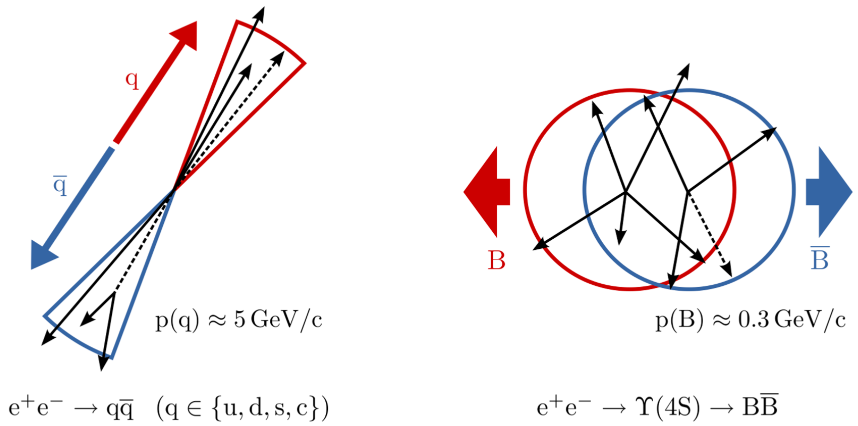

Figure 3.3: Momentum-weighted distribution of all particles in the detector for continuum and $B\bar{B}$ events.

spherical symmetry, as illustrated in Fig. 3.3.

To suppress continuum background, a set of loose selection criteria is applied to the following observables: $\cos\theta_T$, ΔE, and FoxWolframR2 (R_2).

The variable $\cos\theta_T$ represents the cosine of the angle between the thrust axis of the B_{tag} candidate and that of the rest of the event. This observable is particularly effective, as $B\bar{B}$ events yield an approximately uniform distribution, while continuum events are strongly peaked near unity. A requirement of $|\cos\theta_T| < 0.9$ is imposed.

The second variable, ΔE, denotes the difference between the energy of the B_{tag} candidate and the nominal beam energy in the center-of-mass frame. For correctly reconstructed $B\bar{B}$ events, ΔE is expected to peak at zero. However, since this variable is also utilized by the FEI algorithm, the continuum background distribution is modified and similarly peaks near zero. The selection $-150 < \Delta E < 100\,\mathrm{MeV}$ is applied.

The third variable, R_2, quantifies the event sphericity and is widely employed in B physics analyses to distinguish continuum from $B\bar{B}$ events. A loose cut of $R_2 < 0.6$ is adopted [59].

Following these cut-based continuum suppression requirements, approximately 99% of the $\tau^+\tau^-$ background component is rejected. Table 3.4 summarizes the signal and background efficiencies at each stage of the selection, starting from events passing the preselection criteria.

Figure 3.4 presents the distributions of these observables in off-resonance data and MC simulation, scaled to the off-resonance luminosity, prior to the application of the cut-based continuum suppression. As evident from the figure,

Table 3.4: Efficiency breakdown for cut-based continuum rejection. The preselection row reports the fraction of events satisfying the criteria in Table 3.3.

Selection	$B^+ \to \tau^+\nu_\tau$	$q\bar{q}$	$\tau^+\tau^-$
Preselection	100%	100%	100%
$\lvert\cos\theta_\mathrm{T}\rvert < 0.9$	86%	40%	17%
$-150 < \Delta E < 100\,\mathrm{MeV}$	74%	35%	8%
$R_2 < 0.6$	73%	34%	1%

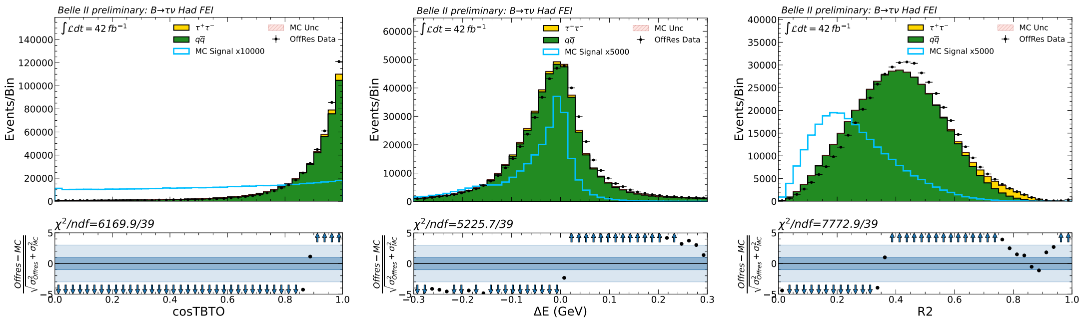

Figure 3.4: Distributions of $\lvert\cos\theta_\mathrm{T}\rvert$, ΔE, and R_2 for continuum MC, signal MC, and off-resonance data after preselection.

continuum MC simulations do not accurately reproduce the experimental data. The approach adopted to address this simulation mismodeling is discussed in Sec. 3.6.

3.6 CONTINUUM BACKGROUND MODELING

Continuum events constitute a substantial component of the background, particularly for hadronic τ decay modes. Even after the cut-based continuum rejection described in Sec. 3.5, the residual background remains significant. Consequently, it is essential to accurately estimate both the yields and the shapes of key observables, especially those employed in the final fit for signal extraction. Ideally, off-resonance data collected 60 MeV below the $\Upsilon(4S)$ mass peak would be used to model the distributions after the final selection. Although Belle II acquires approximately 10% of its data off-resonance, the limited statistics are sufficient for estimating the total background yield but are inadequate for reliably modeling the shapes of distributions. As an alternative, high-statistics

Table 3.5: Scaling factors for continuum MC simulations relative to off-resonance data.

Mode	Scaling Factor
$e^+\nu_e\bar{\nu}_\tau$	0.94 ± 0.03
$\mu^+\nu_\mu\bar{\nu}_\tau$	0.95 ± 0.02
$\pi^+\bar{\nu}_\tau$	0.92 ± 0.02
$\rho^+\bar{\nu}_\tau$	0.724 ± 0.008

MC simulations are available.
Table 3.5 reports the scaling factors between off-resonance data and MC yields.

To estimate the total continuum yield in on-resonance data, the off-resonance sample is scaled by the on-/off-resonance luminosity ratio. The shapes of the continuum background are modeled using MC simulations, which benefit from higher statistics. To improve the agreement between MC and data, a multivariate reweighting procedure is employed, following the method described in Refs. [60, 61]. Specifically, a Fast Boosted Decision Tree (FBDT) classifier [62] is trained to identify and correct discrepancies between data and MC. For calibration, 200 fb^{-1} equivalent continuum MC events and the full off-resonance dataset are used.
The FBDT hyperparameters ($N_{\text{trees}} = 200$, depth $= 2$, shrinkage $= 0.1$) are optimized to minimize the difference in Area Under the Curve (AUC) between training and test samples. The input variables for training are primarily event-shape, Rest of Event, and kinematic quantities. Since off-resonance data are collected at $\sqrt{s_{\text{off}}} = 10.52\,\text{GeV}$, it is necessary to reweight the energy to match the on-resonance conditions. In particular, M_{bc} and ΔE are recalculated as follows:

$$M_{bc} = \frac{1}{c^2}\sqrt{\frac{s}{4} - \frac{s}{s_{\text{off}}} p_B^{*2} c^2}\,; \tag{3.2}$$

$$\Delta E = \sqrt{\frac{s}{s_{\text{off}}}} E_B^* - \frac{\sqrt{s}}{2}. \tag{3.3}$$

The reweighting procedure is as follows: a classifier is trained with off-resonance data as *signal* and continuum MC as *background*. If the MC accurately models the data, the classifier output distributions for both samples would be identical; otherwise, the classifier highlights the discrepancies.
Figure 3.5 displays the FBDT output and variable importance, indicating the

degree of mismodeling. The continuum MC is then reweighted to match the data using the classifier output, with the event weight w_{CR} for each event defined as:

$$w^i_{\text{CR}} = \frac{\mathcal{O}^i_{\text{CR}}}{1 - \mathcal{O}^i_{\text{CR}}} \tag{3.4}$$

where $\mathcal{O}^i_{\text{CR}}$ is the output of the classifier for the event i. Figure 3.6 compares the off-resonance data and continuum MC before and after reweighting, normalized to the same total yield.

3.7 CONTINUUM SUPPRESSION

To further enhance the suppression of continuum backgrounds beyond the cut-based selections described previously, a dedicated multivariate approach is employed. Specifically, a second Fast Boosted Decision Tree (FBDT) classifier, referred to as $\mathcal{O}_{\text{CS}}$, is trained to discriminate between continuum and $B\overline{B}$ events. In this training, continuum MC events are treated as the *signal*, while $B\overline{B}$ MC events serve as the *background*. Only variables that exhibit satisfactory data-MC agreement after the continuum reweighting procedure are included as input features for the classifier, ensuring robust performance and minimizing systematic uncertainties. The FBDT algorithm natively supports event weights, which are applied to account for the residual mismodeling between MC and data.

Given the distinct event-shape characteristics and data-MC agreement observed in leptonic and hadronic τ decay channels, separate classifiers are trained for each category: $\mathcal{O}_{\text{CS}}$ (lep) for leptonic modes and $\mathcal{O}_{\text{CS}}$ (had) for hadronic modes. The hyperparameters for both classifiers ($N_{\text{trees}} = 300$, depth $= 2$, shrinkage $= 0.1$) are optimized to maximize the area under the ROC curve, while also ensuring good agreement between training and test samples to avoid overtraining.

Figure 3.7 illustrates the performance of the continuum suppression FBDT classifiers for both leptonic and hadronic channels. For each channel, the ROC curve quantifies the classifier's ability to distinguish continuum from $B\overline{B}$ events, while the overtraining check compares the classifier output distributions for training and test samples, confirming the absence of significant overfitting.

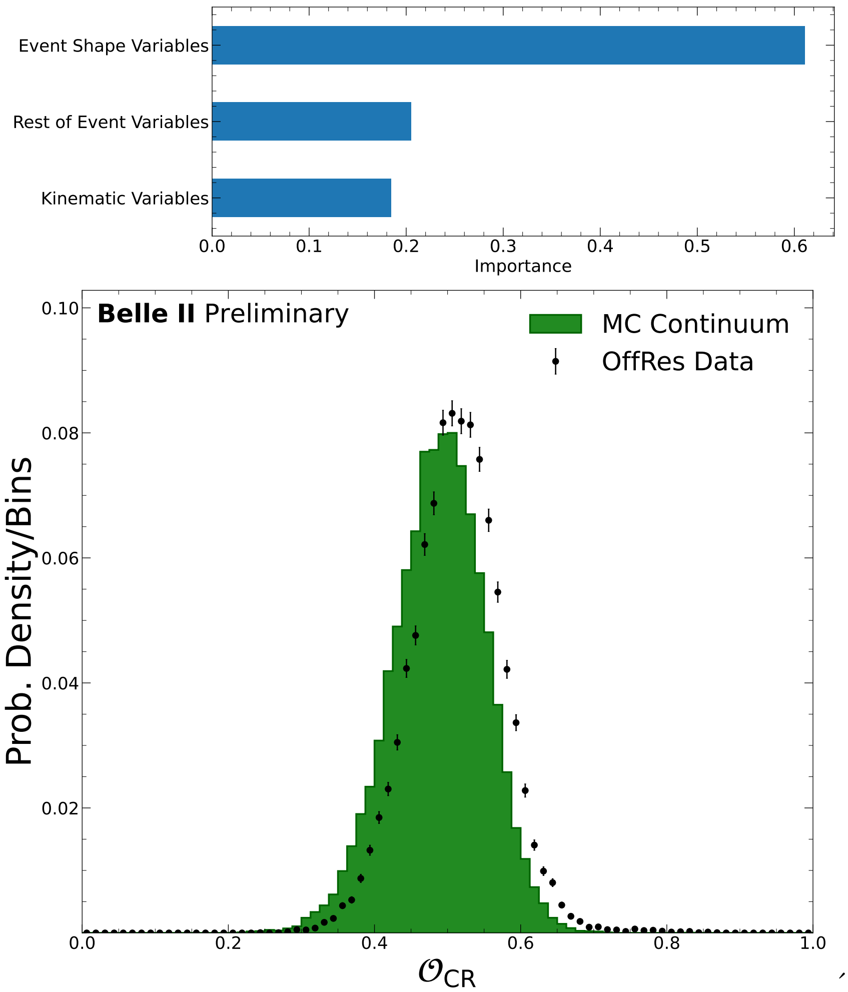

Figure 3.5: Continuum Reweight FBDT performance plots: variable importance, the greater the importance the greater the mismodeling (top plot). Train-Test comparison (bottom plot).

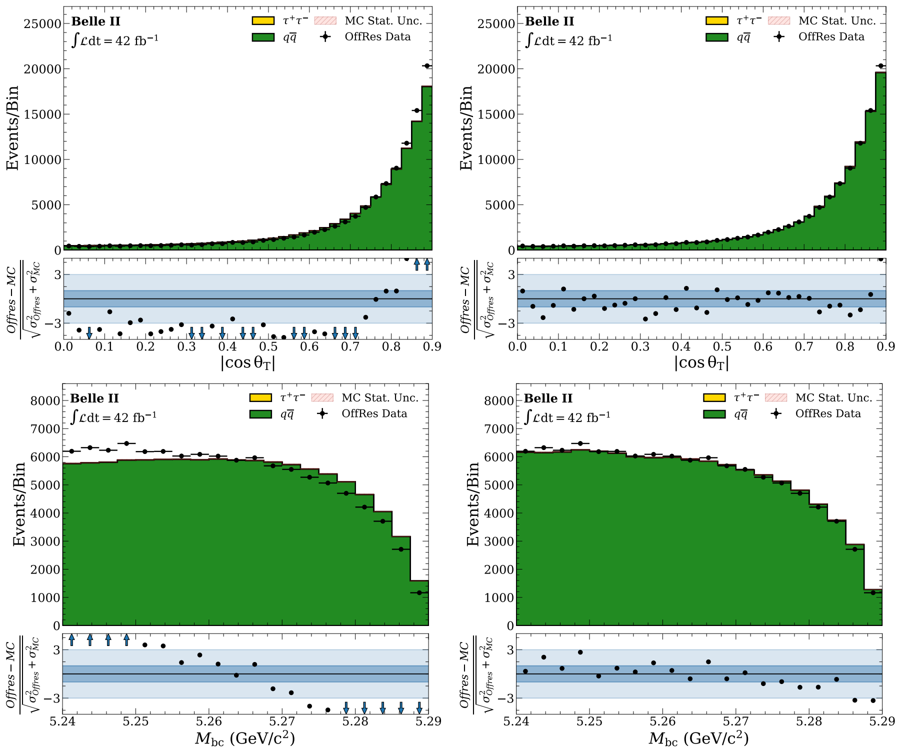

Figure 3.6: Distributions of $|\cos\theta_T|$ (top) and M_{bc} (bottom) in off-resonance data and continuum simulation before (left) and after (right) the continuum MC reweighting. The $\tau^+\tau^-$ component is negligible after the requirement on R_2.

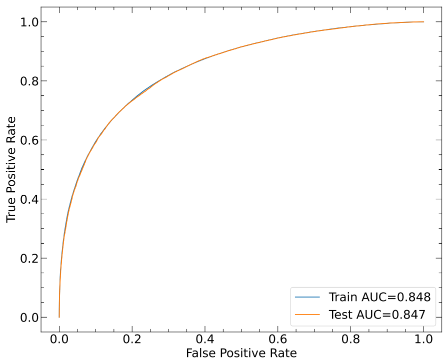

(a) Leptonic ROC curve

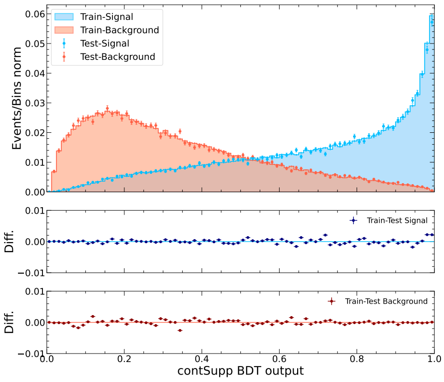

(b) Leptonic overtraining check

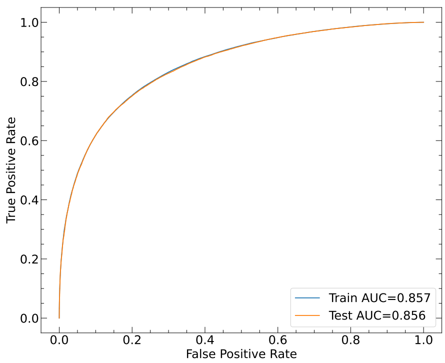

(c) Hadronic ROC curve

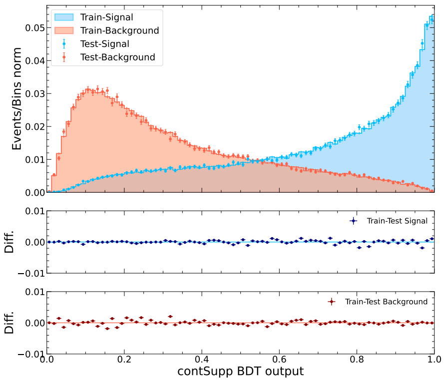

(d) Hadronic overtraining check

Figure 3.7: Performance of the continuum suppression FBDT classifiers for leptonic (top) and hadronic (bottom) channels. Left: ROC curves. Right: overtraining checks comparing classifier output for training and test samples.

4 SIGNAL SELECTION OPTIMIZATION

To optimize the signal selection, we extract four distinct signal yields, each corresponding to a specific τ^+ decay channel. All cleaned clusters from the electromagnetic calorimeter are considered in the construction of two key discriminating observables: the total residual energy in the ECL ($E_{\text{ECL}}^{\text{extra}}$), and the squared missing four-momentum (M_{miss}^2). The latter is computed using the known beam energies and all visible reconstructed objects, including cleaned ECL clusters:

$$p_{\text{miss}}^* = (\sqrt{s}/c, 0, 0, 0) - p_{\text{tag}}^* - p_{\text{sig}}^* - p_{\text{ROE}}^* \tag{4.1}$$

where p_{tag}^*, p_{sig}^*, and p_{ROE}^* denote the four-momenta in the center-of-mass frame of the B_{tag} candidate, the signal candidate, and the rest of the event (ROE), respectively.

In signal events, $E_{\text{ECL}}^{\text{extra}}$ is expected to be close to zero, as neutrinos produced in the decay do not interact with the ECL, and all visible energy should be accounted for by the reconstructed particles. Any residual energy is primarily attributable to beam-induced background or imperfections in the reconstruction process (hadronic split-off). On contrary, background events tend to exhibit larger values of $E_{\text{ECL}}^{\text{extra}}$, due to additional neutral energy deposits from unassigned tracks or clusters originating from either the B_{tag} or the signal side.

The variable M_{miss}^2 provides additional discrimination power. In signal events with leptonic τ^+ decays, the presence of multiple neutrinos typically results in larger values of M_{miss}^2. In contrast, hadronic τ^+ decays generally yield smaller values, though these remain larger than typical background contributions. This observable is particularly effective at reducing combinatorial backgrounds in leptonic channels and suppressing continuum backgrounds in hadronic channels, thereby enhancing the overall purity of the selected sample.

These variables are shown in Fig. 4.1 for each τ^+ decay channel, after the cut-based event selection (and continuum reweighting) as explained in Chap. 3. We use $E_{\text{ECL}}^{\text{extra}}$ and M_{miss}^2 to extract the signal yields, and so the $\mathcal{B}(B^+ \to \tau^+ \nu_\tau)$, through a 2D maximum likelihood fit to data distribution.

To further enhance the discrimination between signal and background, we exploit several additional observables beyond $E_{\text{ECL}}^{\text{extra}}$ and M_{miss}^2. Specifically, we utilize the output of the FEI algorithm, denoted as $\mathcal{O}_{\text{FEI}}$, explained in App. A,

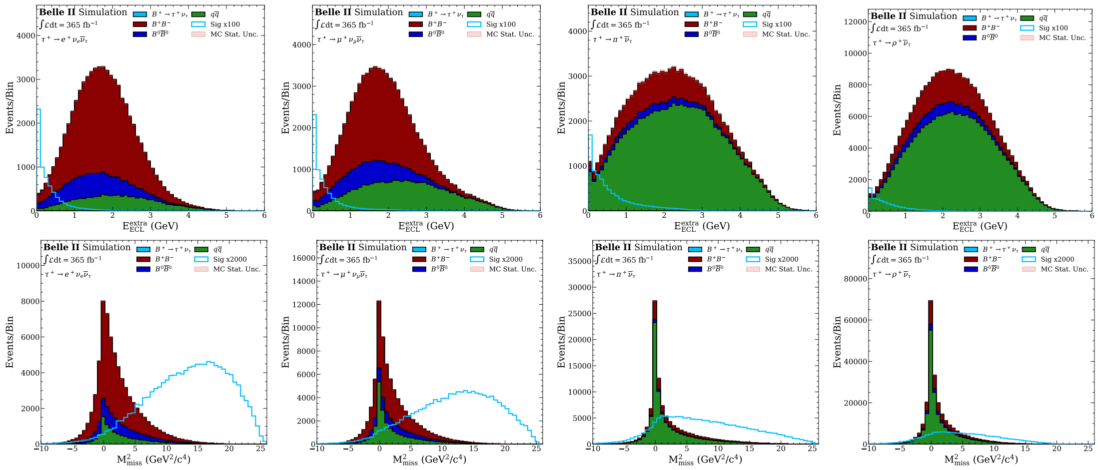

Figure 4.1: Distribution of $E_{\text{ECL}}^{\text{extra}}$ (top) and M_{miss}^2 (bottom) in simulation for the four τ^+ decay modes after the cut-based event selection. Continuum MC has been re-weighted and normalized to off-resonance data. Signal MC is also scaled by a factor of 100 to make it visible.

which quantifies the probability that a reconstructed B_{tag} candidate is correctly identified. We also employ the continuum suppression variable, $\mathcal{O}_{\text{CS}}$, which is derived from a multivariate classifier trained to distinguish $B\bar{B}$ events from continuum $e^+e^- \to q\bar{q}$ $(q = u, d, s, c)$ backgrounds. Furthermore, we consider the momentum of the reconstructed τ^+ daughter candidate (e^+, μ^+, π^+, or ρ^+) in the laboratory frame, denoted as p_{cand}. The distributions of these variables, after the application of the baseline cut-based selection, are presented in Fig. 4.2.

The variable $\mathcal{O}_{\text{CS}}$ is particularly effective in suppressing continuum backgrounds, which are especially prominent in hadronic τ^+ decay channels. Imposing a more stringent requirement on $\mathcal{O}_{\text{FEI}}$ increases the purity of the selected sample. The variable p_{cand} provides additional discrimination, especially in hadronic channels, where the kinematics of the two-body decay brings to a higher momentum for the signal.

The selection thresholds for $\mathcal{O}_{\text{FEI}}$, $\mathcal{O}_{\text{CS}}$, and p_{cand} are optimized through a systematic scan over a multidimensional grid of possible cut values. For each configuration, the expected statistical sensitivity is evaluated by generating pseudo-experiments (Toy Monte Carlo), in which the signal and background yields are sampled according to the distributions observed in simulation.

The branching fraction $\mathcal{B}(B^+ \to \tau^+\nu_\tau)$ is determined via a simultaneous extended maximum likelihood fit to the two-dimensional distributions of M_{miss}^2

and $E_{\mathrm{ECL}}^{\mathrm{extra}}$ in all four τ^+ decay channels. The probability density functions (PDFs) for signal and background are constructed as two-dimensional histograms with 10×10 uniform binning in the ranges $-10 < M_{\mathrm{miss}}^2 < 26\ \mathrm{GeV}^2/c^4$ and $0 \leqslant E_{\mathrm{ECL}}^{\mathrm{extra}} < 1\,\mathrm{GeV}$, respectively. The fit includes five free parameters: a common branching fraction $\mathcal{B}(B^+ \to \tau^+\nu_\tau)$ and four background yields $n_{b,k}$, one for each decay channel $k = e^+, \mu^+, \pi^+, \rho^+$. The expected signal yield in each channel, $n_{s,k}$, is given by

$$n_{s,k} = 2n_{B^+B^-}\varepsilon_k \mathcal{B}(B^+ \to \tau^+\nu_\tau), \tag{4.2}$$

where $n_{B^+B^-} = n_{\Upsilon(4S)} f^{+-}$ is the total number of B^+B^- pairs in the dataset, and $f^{+-} = 0.5113^{+0.0073}_{-0.0108}$ is the branching fraction for $\Upsilon(4S) \to B^+B^-$ decays, as reported in Ref. [27]. The reconstruction efficiency ε_k for each channel is determined from Monte Carlo simulations. These efficiencies include the branching fractions of the relevant τ^+ decays and incorporate the effects of cross-feed between channels. The composition of reconstructed τ^+ candidates in terms of their true decay modes, including cross-feed contributions, is summarized in Tab. 4.2.

The optimization procedure is performed independently for each decay channel. For every point in the grid of selection requirements, 10^4 pseudo-datasets are generated using the MC-derived $E_{\mathrm{ECL}}^{\mathrm{extra}}$ and M_{miss}^2 distributions, and the signal extraction fit is repeated. The expected relative statistical uncertainty for each channel is then defined as $\langle \sigma_{n_{s,k}} \rangle / \langle n_{s,k} \rangle$, where $\langle \sigma_{n_{s,k}} \rangle$ is the mean uncertainty on the fitted signal yield and $\langle n_{s,k} \rangle$ is the mean fitted yield across the pseudo-experiments.

All calibrations described in Chap. 5 are applied consistently throughout the analysis. The optimized selection thresholds for $\mathcal{O}_{\mathrm{FEI}}$, $\mathcal{O}_{\mathrm{CS}}$, and p_{cand} are summarized in Tab. 4.1. Figures 4.4 show the distributions of the selection variables after applying the optimized selection.

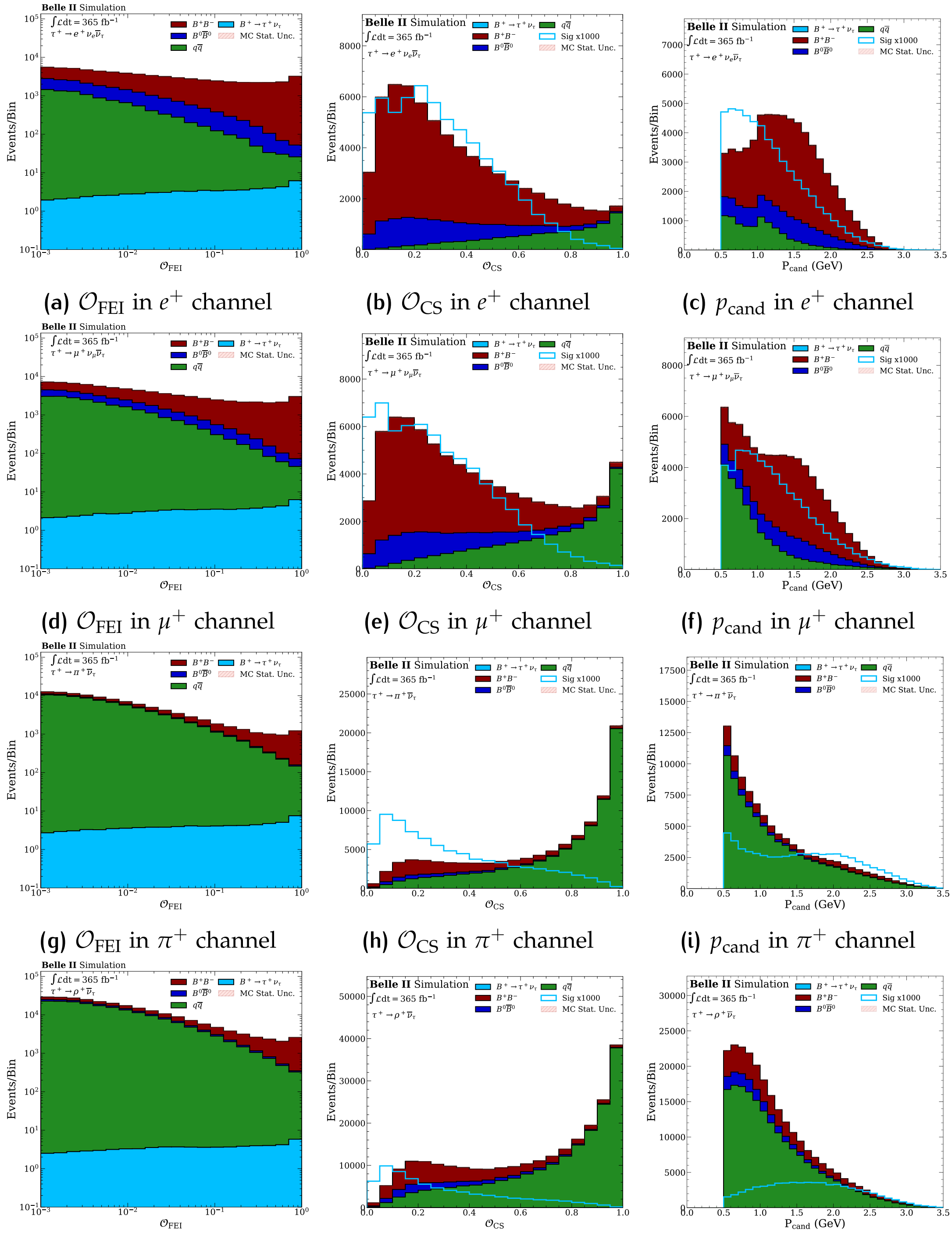

(a) $\mathcal{O}_{\mathrm{FEI}}$ in e^+ channel (b) $\mathcal{O}_{\mathrm{CS}}$ in e^+ channel (c) p_{cand} in e^+ channel

(d) $\mathcal{O}_{\mathrm{FEI}}$ in μ^+ channel (e) $\mathcal{O}_{\mathrm{CS}}$ in μ^+ channel (f) p_{cand} in μ^+ channel

(g) $\mathcal{O}_{\mathrm{FEI}}$ in π^+ channel (h) $\mathcal{O}_{\mathrm{CS}}$ in π^+ channel (i) p_{cand} in π^+ channel

(j) $\mathcal{O}_{\mathrm{FEI}}$ in ρ^+ channel (k) $\mathcal{O}_{\mathrm{CS}}$ in ρ^+ channel (l) p_{cand} in ρ^+ channel

Figure 4.2: Distributions of the selection variables $\mathcal{O}_{\mathrm{FEI}}$, $\mathcal{O}_{\mathrm{CS}}$, and p_{cand} for the four τ^+ decay channels after the cut-based event selection. The distributions are shown for only simulation, with continuum re-weighted and normalized to off-resonance data. Signal MC is also scaled by a factor of 100 to enhance visibility.

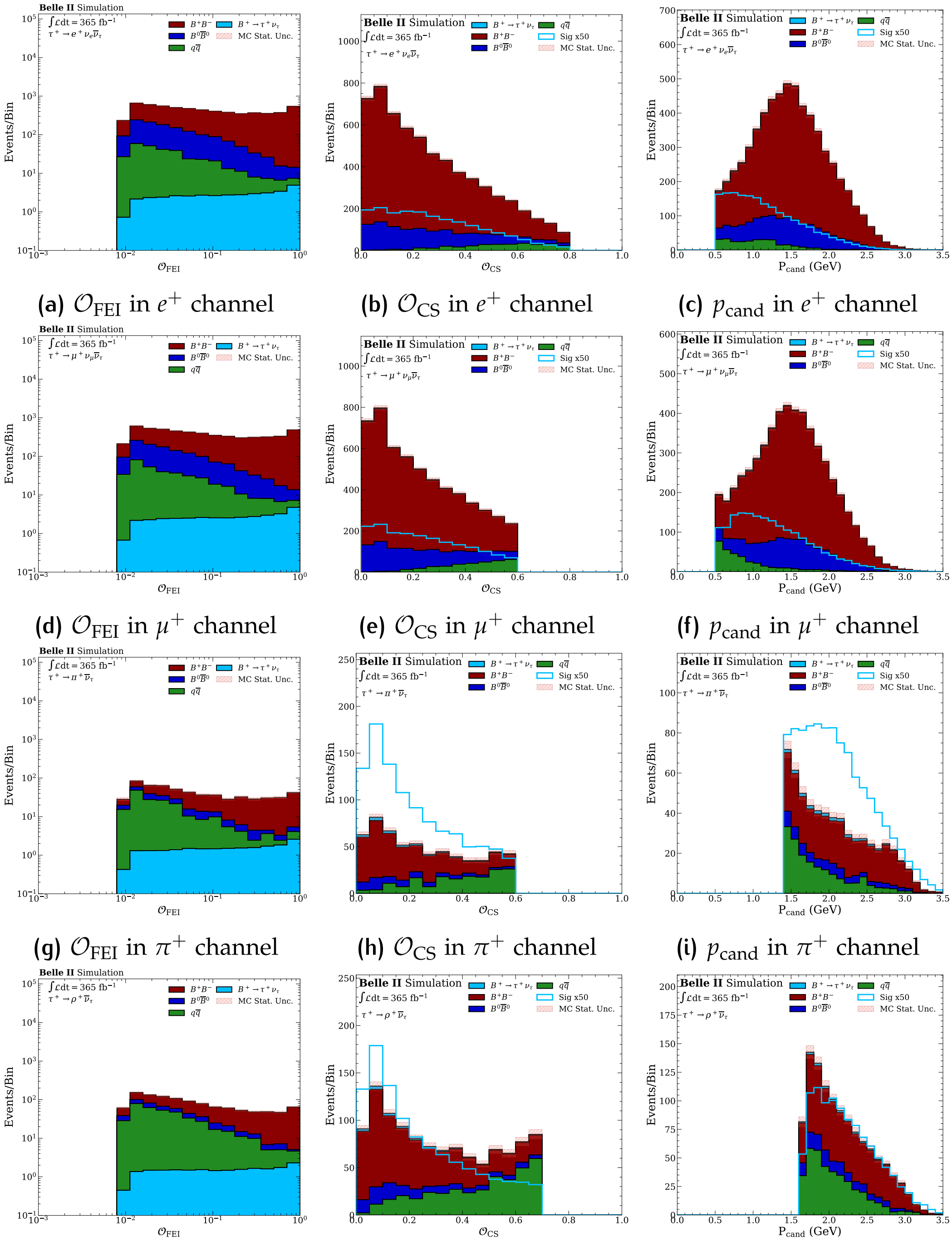

(a) $\mathcal{O}_{\text{FEI}}$ in e^+ channel (b) $\mathcal{O}_{\text{CS}}$ in e^+ channel (c) p_{cand} in e^+ channel

(d) $\mathcal{O}_{\text{FEI}}$ in μ^+ channel (e) $\mathcal{O}_{\text{CS}}$ in μ^+ channel (f) p_{cand} in μ^+ channel

(g) $\mathcal{O}_{\text{FEI}}$ in π^+ channel (h) $\mathcal{O}_{\text{CS}}$ in π^+ channel (i) p_{cand} in π^+ channel

(j) $\mathcal{O}_{\text{FEI}}$ in ρ^+ channel (k) $\mathcal{O}_{\text{CS}}$ in ρ^+ channel (l) p_{cand} in ρ^+ channel

Figure 4.3: Distributions of the selection variables $\mathcal{O}_{\text{FEI}}$, $\mathcal{O}_{\text{CS}}$, and p_{cand} for the four τ^+ decay channels after the optimized selection. The distributions are shown for only simulation, with continuum re-weighted and normalized to off-resonance data. Signal MC is also scaled by a factor of 100 to enhance visibility.

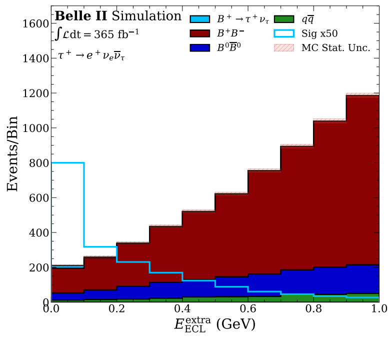

(a) $E_{\mathrm{ECL}}^{\mathrm{extra}}$ in e^+ channel

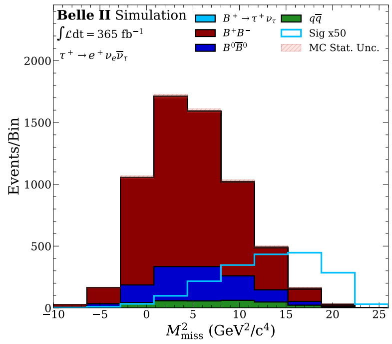

(b) M_{miss}^2 in e^+ channel

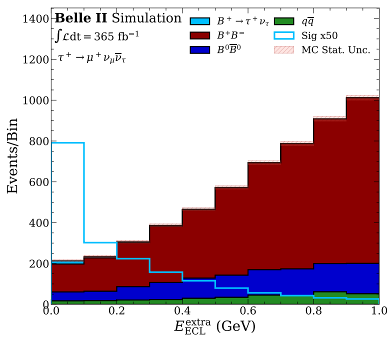

(c) $E_{\mathrm{ECL}}^{\mathrm{extra}}$ in μ^+ channel

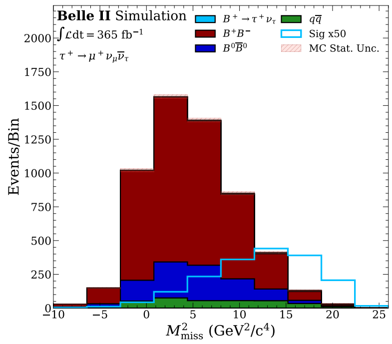

(d) M_{miss}^2 in μ^+ channel

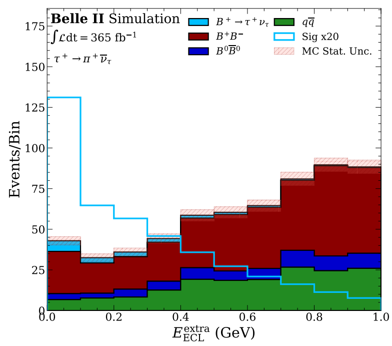

(e) $E_{\mathrm{ECL}}^{\mathrm{extra}}$ in π^+ channel

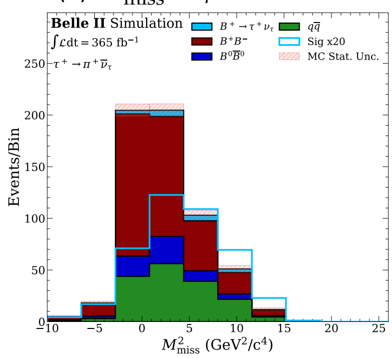

(f) M_{miss}^2 in π^+ channel

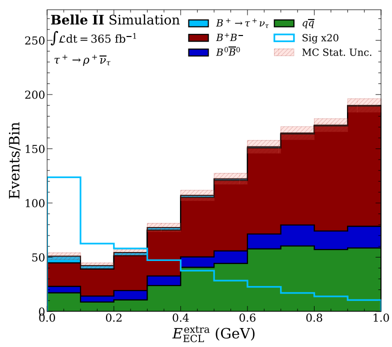

(g) $E_{\mathrm{ECL}}^{\mathrm{extra}}$ in ρ^+ channel

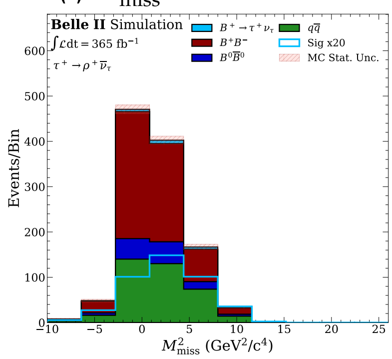

(h) M_{miss}^2 in ρ^+ channel

Figure 4.4: Distributions of $E_{\mathrm{ECL}}^{\mathrm{extra}}$ (left) and M_{miss}^2 (right) after the optimized selection for the four τ^+ decay channels. The distributions are shown for only simulation, with continuum re-weighted and normalized to off-resonance data. Signal MC is also scaled by a factor of 100 to enhance visibility.

Table 4.1: Optimized selection requirements and corresponding signal efficiencies. ϵ represents the efficiency for a $B^+ \to \tau^+ \nu_\tau$ event to be reconstructed in the specified category.

Mode	PID	M_{bc} (GeV $/c^2$)	$\mathcal{O}_{\text{FEI}}$	$\mathcal{O}_{\text{CS}}$	p_{cand} (GeV $/c$)	ε (10^{-4})
e^+	> 0.9	> 5.27	> 0.01	< 0.8	> 0.5	7.3
μ^+				< 0.6		7.6
π^+	> 0.6			< 0.6	> 1.4	3.4
ρ^+				< 0.7	> 1.65	3.1

Table 4.2: Composition of each reconstructed τ decay from $B^+ \to \tau^+ \nu_\tau$ in terms of decay mode. The row denotes the reconstructed final state, and the columns represent the generated decay mode. The off-diagonal entries reflect the amount of cross-feed between channels.

Reco \ True	e^+ (%)	μ^+ (%)	π^+ (%)	ρ^+ (%)	other(%)
e^+	97	0.1	0.1	0	2.8
μ^+	0	87	0.9	0.1	12
π^+	0.1	3.3	55.7	16	24.9
ρ^+	0.4	4.5	27.8	61.2	6.1

5 CALIBRATION AND VALIDATION

This chapter provides an overview of the calibration procedures applied to Monte Carlo simulations in this analysis. The calibration strategy combines official correction factors released by the Belle II collaboration with additional, dedicated corrections developed specifically for this analysis. Each source of potential data/MC discrepancy, such as tracking, particle identification, neutral reconstruction, and branching fractions *"cocktail"* in MC simulation, is systematically investigated and, where necessary, corrected and validated using control samples. After the application of all corrections, the agreement between data and simulation is checked by comparing the distributions of the key discriminating variables.

5.1 TRACKING EFFICIENCY CORRECTION

The tracking efficiency for charged particles with momenta in the range $0.2 < p < 3.5\,\mathrm{GeV}/c$ is evaluated using a control sample of $e^+e^- \to \tau^+\tau^-$ events, where one τ lepton decays leptonically and the other decays hadronically into three charged pions. In this approach, events are selected in which a lepton candidate and two pion candidates are reconstructed, ensuring that the total charge of the three tracks is ± 1. The efficiency for reconstructing charged tracks is then determined by examining the probability of successfully reconstructing the third track, which is expected to have a charge of ∓ 1 to balance the event. This method allows for an unbiased measurement of the tracking efficiency, as the presence of the third track is inferred from kinematic and charge conservation constraints.
The tracking efficiency is studied as a function of the track's transverse momentum, polar angle, and azimuthal angle. Consequently, no data-driven correction factors are applied to the simulation. However, a systematic uncertainty is assigned to account for potential residual discrepancies, particularly those arising from possible charge-dependent effects in the reconstruction efficiency. This uncertainty is conservatively estimated based on the observed

charge asymmetry in the control sample and is propagated to the final results for all tracks with $p > 0.5\,\text{GeV}/c$.

5.2 LEPTON IDENTIFICATION EFFICIENCY CORRECTION

The accurate identification of leptons is a critical aspect of this analysis, as it directly impacts both the signal selection efficiency and the background suppression. In order to account for possible discrepancies between data and MC simulation in the lepton identification ID performance, dedicated correction factors are applied to the MC samples. These corrections are derived from official Belle II calibration tables, which provide data-to-MC efficiency ratios as functions of the lepton momentum and polar angle.

The correction factors are determined using high-purity control samples of electrons and muons. Specifically, electrons and muons are selected from decays such as $J/\psi \to \ell^+\ell^-$, as well as from low-multiplicity processes including $e^+e^- \to \ell^+\ell^-(\gamma)$ and $e^+e^- \to e^+e^-\ell^+\ell^-$. These processes offer clean environments with well-understood kinematics, enabling precise measurements of the lepton ID efficiencies in both data and simulation. The efficiency is evaluated in bins of momentum and polar angle, and the ratio of efficiencies in data to those in MC is computed for each bin. The resulting scaling factors are then applied as event weights to the MC events.

5.3 PION IDENTIFICATION EFFICIENCY CORRECTION

The identification of charged pions is another essential component of the analysis, particularly for the reconstruction of hadronic τ decays and background suppression. As with leptons, differences in the pion identification efficiency and misidentification rates between data and MC simulation are corrected using official Belle II calibration tables. These tables provide data-to-MC efficiency ratios and misidentification probabilities as functions of the track momentum and polar angle.

The calibration of the pion ID efficiency is performed using control samples enriched in pions, such as those from decays of $K^0_S \to \pi^+\pi^-$, $D^{*+} \to D^0\pi^+$, and $\Lambda^0 \to p\,\pi^-$. These samples are selected to provide a high-purity source of pions across a broad kinematic range, allowing for a detailed mapping of the efficiency and fake rate corrections. For each bin in momentum and polar

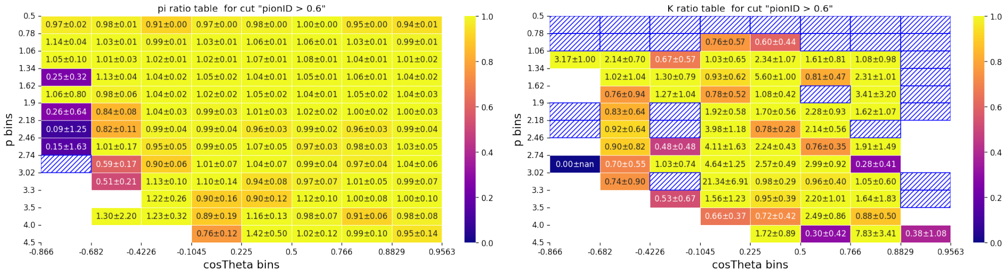

(a) Data-to-MC ratios for the pion identification efficiency, with associated uncertainties

(b) Data-to-MC ratios for the kaon misidentification (fake) rates, with associated uncertainties

Figure 5.1: Pion identification efficiency and kaon misidentification correction factors used in the analysis. The data/MC ratios are shown as a function of the track momentum and polar angle, with uncertainties represented by the shaded bands.

angle, the efficiency of correctly identifying a pion, as well as the probability of misidentifying a kaon as a pion, is measured in both data and MC.
Figure 5.1 presents the efficiency and misidentification tables used in this analysis.

5.4 π^0 RECONSTRUCTION EFFICIENCY

The reconstruction efficiency of neutral pions (π^0) is important in $\tau^+ \to \rho^+ \bar{\nu}_\tau$ decays. Discrepancies between data and MC simulation in the modeling of π^0 reconstruction can introduce biases in the signal yield and background estimation. To mitigate these effects, dedicated correction factors are applied to the MC samples to account for residual differences in π^0 reconstruction efficiency as a function of the π^0 momentum.
The correction factors are derived using the $D^{*0} \to D^0\, \pi^0$, with $D^0 \to K^-\, \pi^+$ (π^0), sample, where the π^0 reconstruction efficiency is measured both in data and simulation. The ratio of efficiencies (data/MC) is computed in bins of π^0 momentum.
Table 5.1 summarizes the correction factors adopted in this analysis for π^0 mesons originating from ρ candidates.

Table 5.1: Correction factors for the π^0 reconstruction efficiency as a function of π^0 momentum, derived from control samples. The quoted uncertainties are statistical only.

π^0 Momentum Range (GeV / c)	Correction Factor
$(0.05, 0.2)$	0.960 ± 0.006
$(0.4, 0.6)$	0.985 ± 0.042
$(0.6, 0.8)$	1.032 ± 0.053
$(0.8, 1.0)$	1.033 ± 0.042
$(1.0, 1.5)$	1.052 ± 0.047
$(1.5, 2.0)$	1.060 ± 0.047
$(2.0, 3.0)$	1.023 ± 0.048

5.5 BRANCHING FRACTION CORRECTIONS IN MONTE CARLO SIMULATION

In the generation of the simulated B^+B^- and $B^0\overline{B}^0$ samples, the branching fractions used for the various decay modes are not always aligned with the most recent world averages published by the Particle Data Group (PDG) [22]. This discrepancy arises because the MC production is typically based on a fixed set of input parameters, which may become outdated as new experimental measurements are incorporated into the PDG averages. To ensure that the simulation accurately reflects the current knowledge of B and D meson decays. a reweighting is applied by assigning to each event a weight equal to the ratio of the PDG branching fraction to the value used in the MC generation for the corresponding decay channel. In this way, the relative contributions of different decay modes in the simulated sample are corrected to reproduce the most up-to-date experimental results. The uncertainty of the measurement is accounted in the systematic uncertainty evaluation, explained in Chap. 7

5.6 SHAPE CORRECTION OF FIT VARIABLES

The variables $E_{\text{ECL}}^{\text{extra}}$ and M_{miss}^2, introduced in Chap. 4, serve as the principal discriminants between the $B^+ \to \tau^+\nu_\tau$ signal and the various background processes. In particular, the region with $E_{\text{ECL}}^{\text{extra}} > 0.5\,\text{GeV}$, where the expected

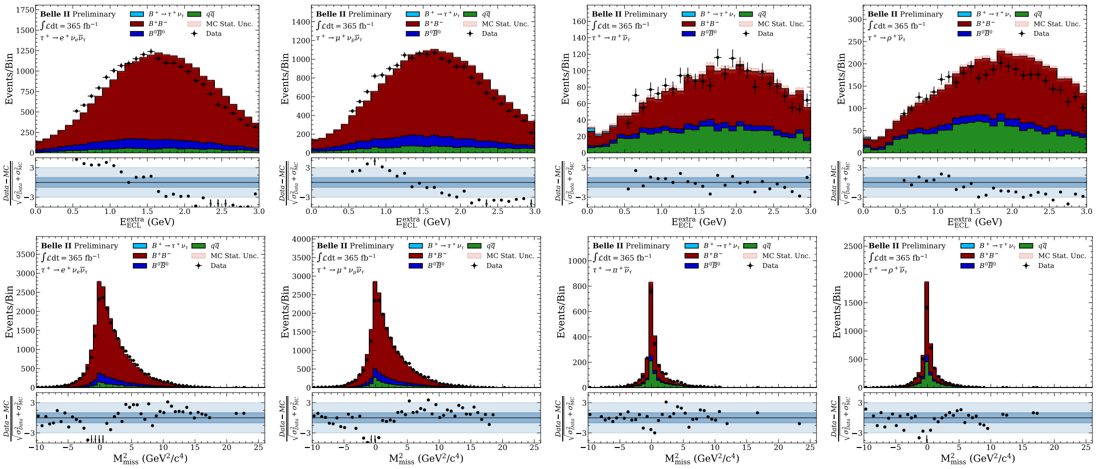

Figure 5.2: M_{miss}^2 distribution for the four signal channels in the $E_{\text{ECL}}^{\text{extra}} > 0.5\,\text{GeV}$ sideband.

signal contribution is negligible, is unblinded to enable a direct comparison between data and MC simulation. In this region, a significant discrepancy is observed between the distributions in data and MC, as illustrated in Fig. 5.2. The data/MC disagreement is due to an imperfect modeling of the reconstruction efficiency for ECL neutral clusters, which directly impacts the multiplicity of reconstructed photons ($n_{\gamma\text{extra}}$). This effect, in turn, influences the distributions of both $E_{\text{ECL}}^{\text{extra}}$ and M_{miss}^2, as these variables are sensitive to the presence of additional neutral energy in the event.
To address this issue, a two-step correction procedure is implemented:

1. **Photon Reconstruction Efficiency Correction:** The first step involves correcting the photon reconstruction efficiency in the MC simulation. This is accomplished by randomly removing photons from reconstructed MC events with a probability $1-\omega$, where ω is defined as the ratio of the photon reconstruction efficiency measured in data to that in simulation. The value of ω is determined as a function of the photon's kinematic properties (momentum and angular coordinates) using high-purity control samples of $e^+e^- \to \mu^+\mu^-\,\gamma$ events. This approach ensures that the photon reconstruction efficiency in simulation is brought into quantitative agreement with that observed in data, thereby mitigating the most significant source of discrepancy.

2. **Bin-by-bin Correction of Photon Multiplicity ($n_{\gamma\text{extra}}$):** Despite the application of the photon efficiency correction, residual discrepancies persist

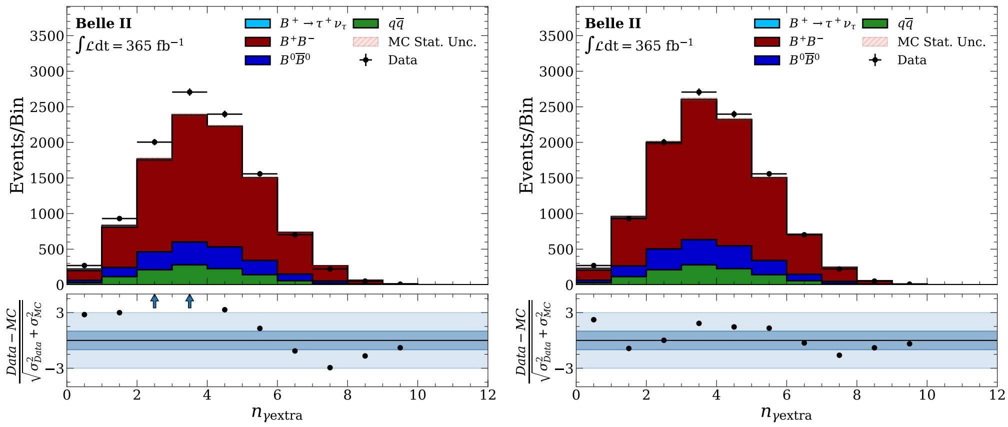

(a) $n_{\gamma\text{extra}}$ before applying corrections

(b) $n_{\gamma\text{extra}}$ after applying corrections

Figure 5.3: Distributions of $n_{\gamma\text{extra}}$ in data and simulation for $E_{\text{ECL}}^{\text{extra}} < 1$ GeV.

in the $E_{\text{ECL}}^{\text{extra}}$ distribution, particularly in the overall multiplicity of reconstructed photons. Figure 5.3a shows the distribution of $n_{\gamma\text{extra}}$ before any further correction. To further investigate the source of the disagreement, the $E_{\text{ECL}}^{\text{extra}}$ distributions are examined in bins of fixed $n_{\gamma\text{extra}}$, as shown in Fig. 5.4 for the electron channel. The resulting comparison demonstrates that, for a given value of $n_{\gamma\text{extra}}$, the shape of the $E_{\text{ECL}}^{\text{extra}}$ distribution is well modeled by the simulation. This observation indicates that the remaining discrepancy is predominantly attributable to differences in the overall $n_{\gamma\text{extra}}$ multiplicity between data and MC, rather than to the modeling of $E_{\text{ECL}}^{\text{extra}}$ itself within each multiplicity bin (single photon resolution).

A bin-by-bin correction to the $n_{\gamma\text{extra}}$ multiplicity is implemented to align the MC simulation with the data. The correction factors are derived using dedicated control samples, each specifically designed to represent the background or signal component under study:

- $B\bar{B}$ **Background:** The *Extra Tracks* control sample is constructed by selecting events with additional tracks originating from the interaction point and with momenta below 0.5 GeV /c. The $n_{\gamma\text{extra}}$ correction factors extracted from this sample are applied to reweight the $B\bar{B}$ background simulation. Further methodological details are provided in Subsec. 5.6.1.

- **Leptonic Signal:** For the leptonic τ decay channels, a control sample of $B^+ \to \bar{D}^* \ell^+ \nu_\ell$ decays is used to derive the $n_{\gamma\text{extra}}$ corrections, which are then applied to the signal MC. The selection and calibration strategy for this sample is described in Subsec. 5.6.2.

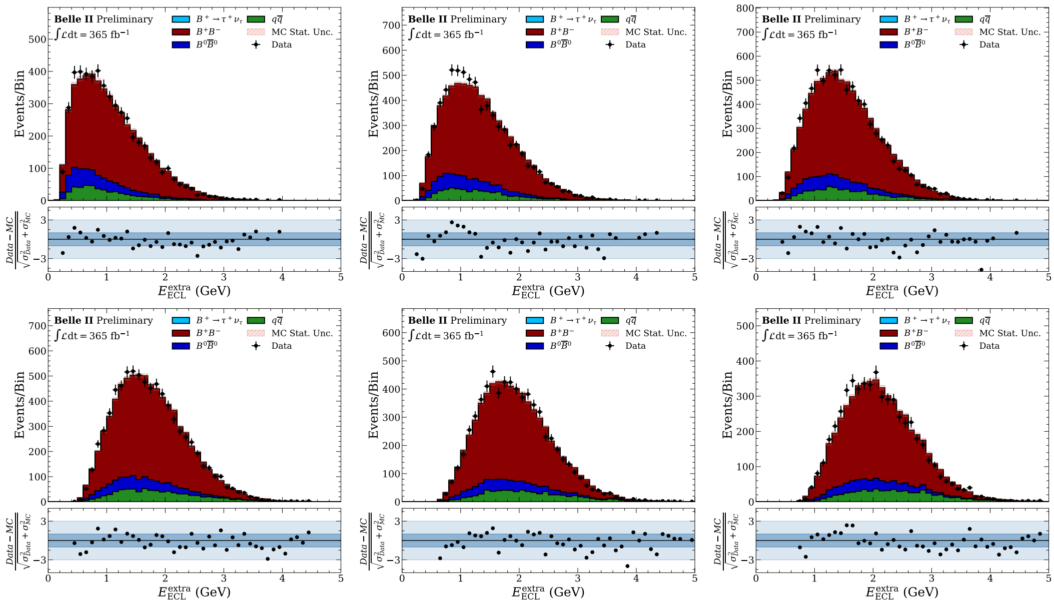

Figure 5.4: $E_{\text{ECL}}^{\text{extra}}$ distribution as a function of $n_{\gamma\text{extra}}$ with the number of events in simulation scaled to data for the electron channel. The first row shows the $E_{\text{ECL}}^{\text{extra}}$ with $n_{\gamma\text{extra}} = 3,4,5$. The second row shows the $E_{\text{ECL}}^{\text{extra}}$ with $n_{\gamma\text{extra}} = 6,7,8$.

- **Hadronic Signal:** For the hadronic τ decay channels, the Double Tag control sample, including events with two non-overlapping hadronic B candidates of opposite charge, is employed to determine the appropriate $n_{\gamma\text{extra}}$ corrections for the signal MC. The details of this sample are given in Subsec. 5.6.3.

The resulting correction factors for each control sample and signal channel are summarized in Tabs. 5.2 and 5.3. The impact of these corrections is illustrated in Fig. 5.5, which show the $E_{\text{ECL}}^{\text{extra}}$ and M_{miss}^2 distributions for each signal decay mode after the application of the corrections. Figure 5.3b demonstrates the improved agreement in the $n_{\gamma\text{extra}}$ distribution between data and simulation following the calibration.
This rigorous, data-driven calibration procedure ensures that the modeling of the key fit variables is robust and that any residual discrepancies between data and simulation are minimized. Additional checks are done using validation samples, explained in Sec. 5.8.

Table 5.2: Bin-by-bin correction factors for the background, evaluated in the *Extra Tracks* control sample for the four channels.

$n_{\gamma \text{extra}}$	e^+	μ^+	π^+	ρ^+
0	(1.101 ± 0.042)	(1.041 ± 0.043)	(1.001 ± 0.123)	(0.803 ± 0.112)
1	(1.190 ± 0.024)	(1.191 ± 0.025)	(1.162 ± 0.071)	(1.052 ± 0.066)
2	(1.168 ± 0.016)	(1.159 ± 0.017)	(1.034 ± 0.048)	(1.078 ± 0.048)
3	(1.111 ± 0.013)	(1.117 ± 0.014)	(0.995 ± 0.040)	(1.024 ± 0.037)
4	(1.061 ± 0.011)	(1.046 ± 0.012)	(0.989 ± 0.037)	(0.981 ± 0.032)
5	(1.023 ± 0.011)	(0.975 ± 0.012)	(0.996 ± 0.039)	(0.986 ± 0.031)
6	(0.970 ± 0.012)	(0.960 ± 0.012)	(0.940 ± 0.041)	(0.962 ± 0.031)
7	(0.894 ± 0.013)	(0.931 ± 0.013)	(0.997 ± 0.049)	(0.978 ± 0.033)
8	(0.863 ± 0.015)	(0.912 ± 0.015)	(0.992 ± 0.062)	(1.028 ± 0.039)
9	(0.844 ± 0.018)	(0.905 ± 0.018)	(1.053 ± 0.084)	(1.003 ± 0.047)

5.6.1 *Extra Tracks* control sample

To evaluate and calibrate the modeling of the $E_{\text{ECL}}^{\text{extra}}$ distribution in the $B\bar{B}$ background simulation, we construct a dedicated control sample, the *Extra Tracks*. This is specifically designed to be enriched in $B\bar{B}$ background events while being orthogonal to the signal region, ensuring that it is free from potential signal contamination.
The selection of the *Extra Tracks* control sample is based on the presence of additional charged tracks in the rest of the event (ROE), not associated with the reconstructed signal and tag sides. Two complementary track multiplicity criteria are employed to define this sample:

- **IP Tracks:** All charged tracks in the ROE are considered as *IP Tracks* if their impact parameter with respect to the interaction point (IP) satisfies $|\texttt{dz}| < 2\,cm$ along the beam axis and $|\texttt{dr}| < 0.5\,cm$ in the transverse plane.

- **Signal-like Tracks:** A subset of the *IP Tracks* is further identified as *Signal-like Tracks* if, in addition to the IP criteria above, the track momentum exceeds 0.5 GeV /*c*. This additional requirement ensures that tracks with kinematic properties similar to those expected from signal decay products are excluded from the control sample.

The *Extra Tracks* control sample is then defined by requiring that the number of *IP Tracks* in the ROE exceeds 0 ($N_{\texttt{IP Tracks}} > 0$), while simultaneously demanding that no *Signal-like Tracks* are present ($N_{\texttt{Signal-like Tracks}} = 0$). This

Table 5.3: Bin-by-bin correction factors for the signal, evaluated in the $B^+ \to \overline{D}^{*0}\ \ell^+\ \nu_\ell$ control sample for the leptonic channels and in the Double Tag control sample for the hadronic channels.

$n_{\gamma\text{extra}}$	e^+/μ^+	π^+/ρ^+
0	(1.093 ± 0.102)	(0.986 ± 0.030)
1	(0.972 ± 0.076)	(1.062 ± 0.020)
2	(1.051 ± 0.089)	(1.044 ± 0.017)
3	(0.904 ± 0.105)	(1.035 ± 0.018)
4	(0.917 ± 0.154)	(0.977 ± 0.020)
5	(0.935 ± 0.251)	(0.916 ± 0.025)

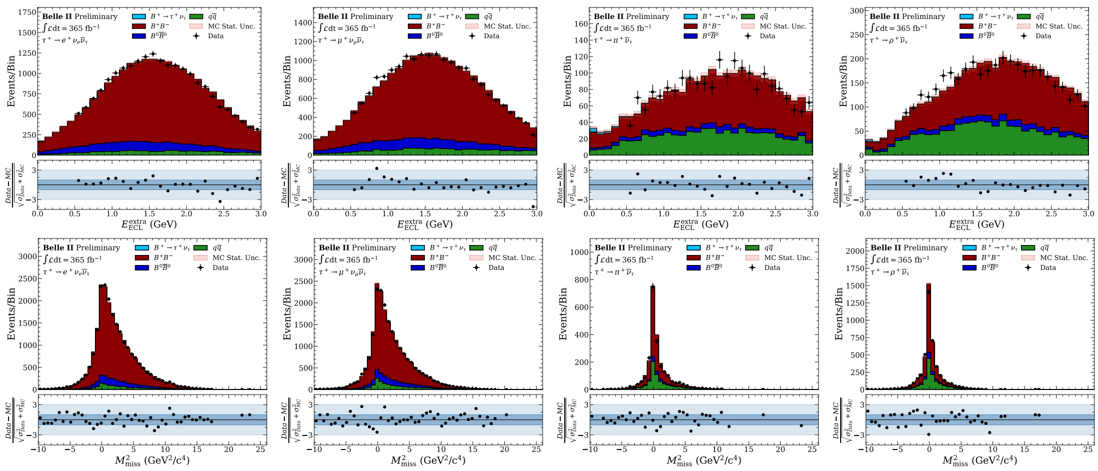

Figure 5.5: M^2_{miss} distribution for the four signal channels after applying all the corrections in the $E^{\text{extra}}_{\text{ECL}} > 0.5\,\text{GeV}$ sideband.

selection efficiently suppresses signal-like topologies and enhances the purity of generic $B\overline{B}$ background events. On average, events in this control sample contain approximately 3.2 *IP Tracks* per event, reflecting the typical multiplicity of additional tracks in generic $B\overline{B}$ decays.

Figure 5.6 presents the distribution of the number of reconstructed neutral clusters ($n_{\gamma\text{extra}}$) in data and simulation for each signal channel within the *Extra Tracks* control sample. The continuum background component is subtracted to isolate the $B\overline{B}$ contribution. The comparison between data and simulation in this sample forms the basis for extracting bin-by-bin correction factors, which are subsequently applied to reweight the MC background and improve the agreement with data in the modeling of the $E^{\text{extra}}_{\text{ECL}}$ observable.

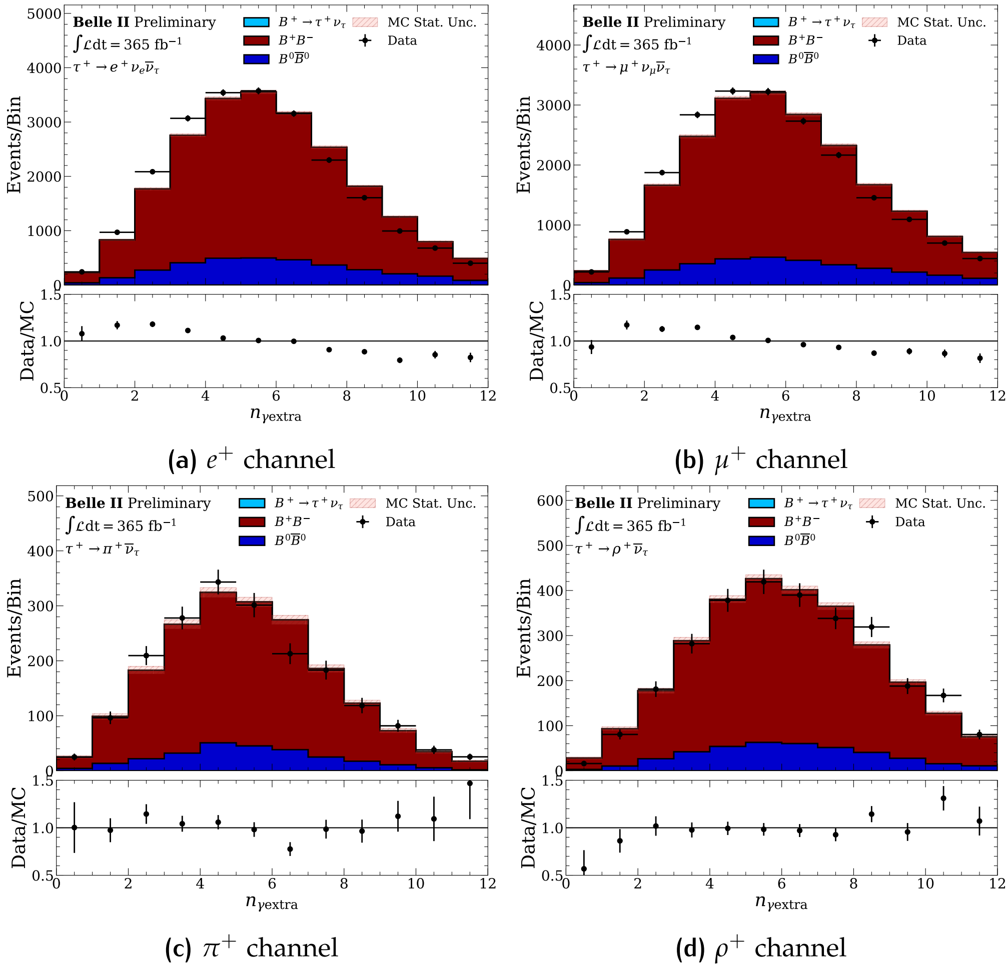

(a) e^+ channel

(b) μ^+ channel

(c) π^+ channel

(d) ρ^+ channel

Figure 5.6: Distributions of $n_{\gamma\mathrm{extra}}$ in the *Extra Tracks* control sample for the four signal channels. The continuum component is subtracted.

5.6.2 $B^+ \to \bar{D}^{*0}\ \ell^+\ \nu_\ell$ control sample

To derive data-driven corrections for reweighting the signal MC in the leptonic τ decay channels, we use the control sample of $B^+ \to \bar{D}^{*0}\ \ell^+\ \nu_\ell$ decays, where $\ell^+ = e^+, \mu^+$. This decay topology shares similar kinematic features with the signal channel $B^+ \to \tau^+\nu_\tau$, particularly in the distribution of $E_{\text{ECL}}^{\text{extra}}$, which is expected to peak near zero in both cases.
In this control sample, the signal-side B meson (B_{sig}) is required to decay into $\bar{D}^{*0}\ \ell^+\ \nu_\ell$, with no additional charged tracks present in the rest of the event (ROE). The hadronic tag-side (B_{tag}) selection is performed using the same multivariate algorithm and criteria as in the main analysis, ensuring consistency in the event topology.
The $\bar{D}^{*0}$ mesons are reconstructed via their decays into $\bar{D}^0\ \pi^0$ and $\bar{D}^0\ \gamma$. The $\bar{D}^0$ candidates are identified in three hadronic final states: $K^+\ \pi^-$, $K_S^0\ \pi^+\ \pi^-$, and $K^+\ \pi^-\ \pi^+\ \pi^-$. After reconstructing both the tag and the signal side, we apply a set of corrections and calibrations to align the simulation with the data. These include continuum reweighting weights, particle identification (PID) efficiency corrections, ROE cluster clean-up procedures, and other standard Belle II corrections, as for the signal sample.
To improve the purity of the selected sample and suppress backgrounds, we impose a momentum threshold of $p_\ell > 1.5\,\text{GeV}/c$. Additionally, for candidates where the $\bar{D}^{*0}$ is reconstructed via the radiative decay mode $\bar{D}^{*0} \to \bar{D}^0\ \gamma$, we require the photon energy to exceed 170 MeV, reducing the contribution from soft combinatorial photons. Following these selection criteria, approximately 84% of the selected events correspond to correctly reconstructed $B^+ \to \bar{D}^{*0}\ \ell^+\ \nu_\ell$ decays. The remaining 16% of the sample consists of misreconstructed backgrounds, primarily originating from $B^+ \to D^{**}\ \ell^+\ \nu_\ell$, $B^+ \to \bar{D}^0\ \ell^+\ \nu_\ell$, and other semileptonic or hadronic decay modes.
Figure 5.7a shows the distribution of the number of extra clusters in the ROE, $n_{\gamma\text{extra}}$, for both data and MC in this control sample, after subtraction of the continuum background. This distribution is used to derive correction factors that are subsequently applied to the signal MC in the leptonic τ channels.
In addition to providing reweighting corrections, the control sample is used to validate the overall signal-side efficiency. After all selection cuts and calibration steps, we find good agreement between data and simulation, with a Data/MC ratio of (0.96 ± 0.04).
Figure 5.8 presents a comparison between data and MC distributions for $E_{\text{ECL}}^{\text{extra}}$ and the missing mass squared variable M_{miss}^2, both before and after applying

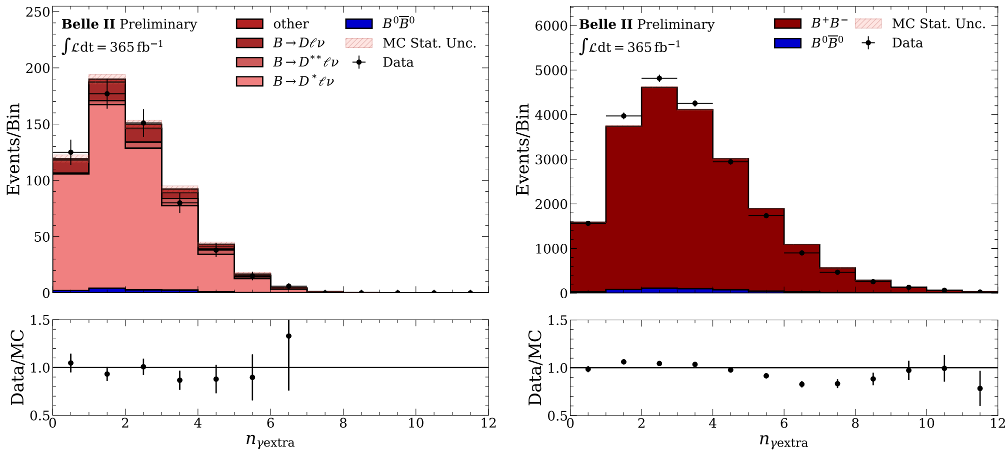

(a) $B^+ \to \bar{D}^{*0}\,\ell^+\,\nu_\ell$ control sample **(b)** Double Tag control sample

Figure 5.7: Distribution of the number of extra clusters ($n_{\gamma\text{extra}}$). The continuum contribution has been subtracted in both cases.

the derived corrections. These comparisons demonstrate the effectiveness of the correction procedure in aligning simulation with data.

5.6.3 Double Tag control sample

The Double Tag (DT) control sample is employed to derive data-driven correction factors for the hadronic τ decay channels in the signal MC simulation. This sample is composed of events in which both B mesons are fully reconstructed through hadronic decay modes using the FEI algorithm. Specifically, two B candidates with opposite charges are identified in each event, and both must satisfy $\mathcal{O}_{\text{FEI}} > 0.01$ criteria.
To ensure a clean event topology and reduce background contamination, we require that no additional charged tracks are present in the Rest of Event (ROE). This selection mimics the topology of signal events with hadronic τ decays.
Similar to the leptonic control sample discussed in Subsec. 5.6.2, the distribution of $E_{\text{ECL}}^{\text{extra}}$ is expected to peak near zero for correctly reconstructed signal-like events.
The DT control sample undergoes the same suite of calibration procedures as the main analysis. These include:

- Continuum suppression through reweighting to match the $q\bar{q}$ background composition observed in data;

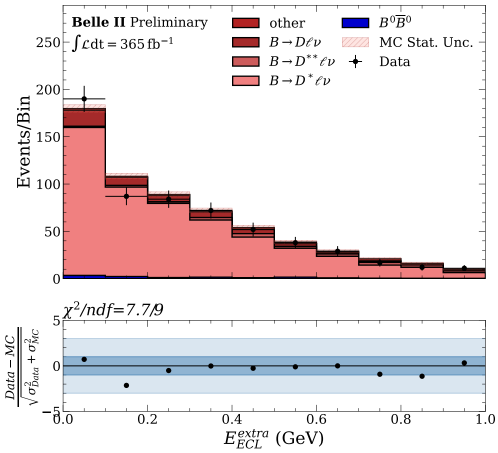

(a) $E_{\mathrm{ECL}}^{\mathrm{extra}}$ before applying corrections

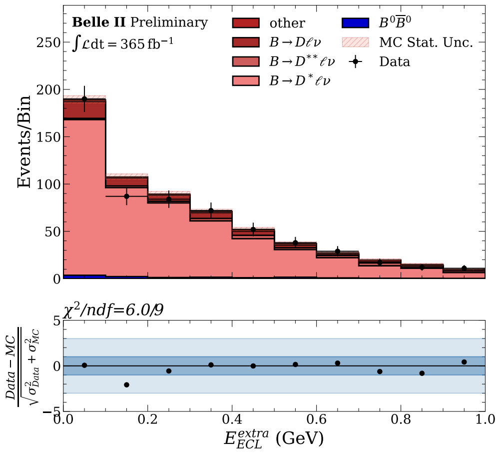

(b) $E_{\mathrm{ECL}}^{\mathrm{extra}}$ after applying corrections

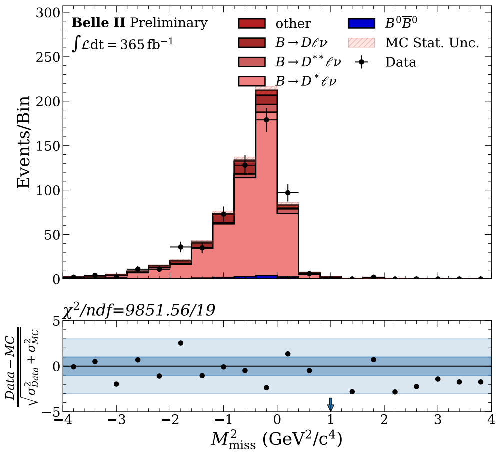

(c) M_{miss}^2 before applying corrections

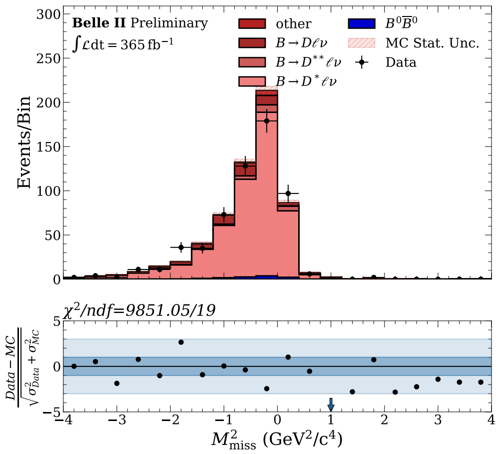

(d) M_{miss}^2 after applying corrections

Figure 5.8: Comparison of the $E_{\mathrm{ECL}}^{\mathrm{extra}}$ and M_{miss}^2 distributions in the $B^+ \to \bar{D}^{*0}\ \ell^+\ \nu_\ell$ control sample.

- Overall normalization to match the integrated luminosity and event yields;
- Corrections for particle identification (PID) efficiency mismatches between data and MC;
- ROE cluster clean-up to mitigate spurious contributions from beam backgrounds or reconstruction artifacts.

Figure 5.7b illustrates the distribution of the number of extra clusters ($n_{\gamma\text{extra}}$) in this control sample, demonstrating good agreement between data and MC. Based on this comparison, we extract bin-by-bin correction factors that are subsequently applied to reweight the signal MC in the hadronic τ decay categories. Furthermore, Figure 5.9 presents the Data/MC comparison for the $E_{\text{ECL}}^{\text{extra}}$ and M_{miss}^2 distributions, both before and after applying the derived corrections. These plots serve as validation of the correction procedure and confirm that the simulation, once corrected, accurately reproduces the distributions observed in data.

5.7 SIGNAL EMBEDDING

The signal embedding technique is employed as an independent cross-check of the signal selection efficiency, and it serves as an additional tool to validate the modeling of the signal region in the simulation. This method enables a direct comparison between data and MC by constructing hybrid events in which a well-reconstructed generic $B\bar{B}$ event provides the event topology, while the signal-side decay $B^+ \to \tau^+\nu_\tau$ is artificially injected from simulated samples.
The embedding procedure is based on the clean and well-understood decay mode $B^+ \to J/\psi\ K^+$, with the subsequent decay $J/\psi \to \ell^+\ell^-$ ($\ell = e, \mu$). This decay topology can be efficiently and exclusively reconstructed in both data and simulated $B\bar{B}$ samples, without any need of B tagging. After reconstructing the $B^+ \to J/\psi\ K^+$ candidate on the signal side of a $B\bar{B}$ event, the entire decay chain of this B^+ meson is removed from the event reconstruction. In its place, a fully simulated $B^+ \to \tau^+\nu_\tau$ decay is embedded.
The rest of the event (ROE) and the tag-side B meson remain unaltered and originate from the original $B^+ \to J/\psi\ K^+$ event. This ensures that the underlying event structure, background environment, and tagging information reflect realistic data conditions. The inserted $B^+ \to \tau^+\nu_\tau$ signal decay is taken from high-statistics MC samples and is reconstructed using the same algorithms and selection criteria as in the main signal analysis.

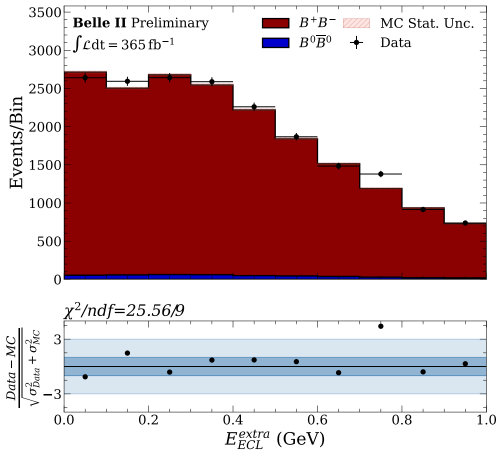

(a) $E_{\mathrm{ECL}}^{\mathrm{extra}}$ before applying corrections

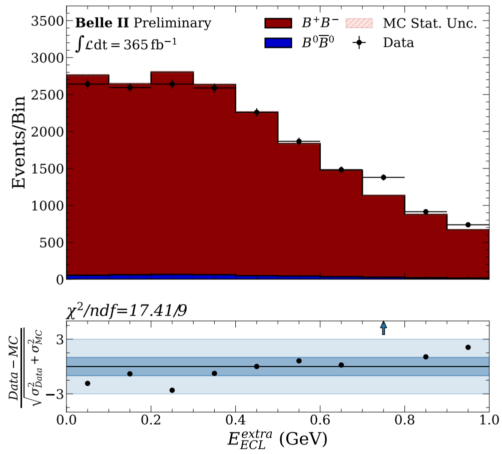

(b) $E_{\mathrm{ECL}}^{\mathrm{extra}}$ after applying corrections

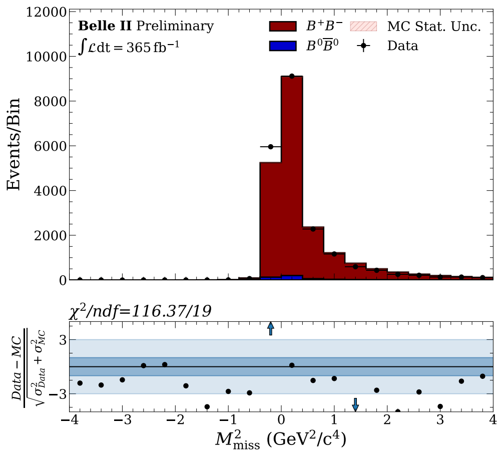

(c) M_{miss}^2 before applying corrections

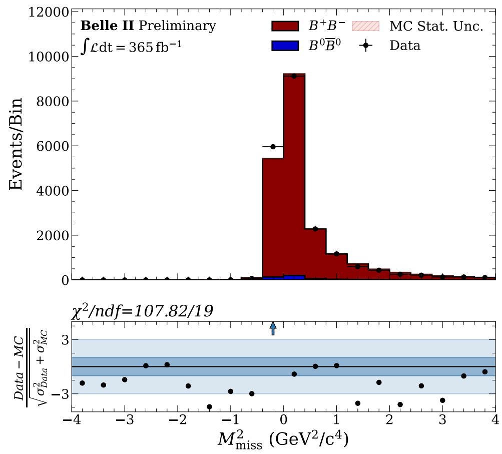

(d) M_{miss}^2 after applying corrections

Figure 5.9: Comparison between data and simulation in the Double Tag control sample.

This technique allows us to isolate and test the signal-side reconstruction and selection efficiency without unbox any signal event in data. After applying the full selection chain to the embedded events, the signal efficiency observed in data and MC is found to be in good agreement, with a Data/MC ratio of (1.02 ± 0.18). This result, with the signal efficiency from $B^+ \to \bar{D}^* \ell^+ \nu_\ell$, confirms the robustness of the signal efficiency in the simulation.
Figure 5.10 shows the distributions of the extra energy in the calorimeter ($E_{\mathrm{ECL}}^{\mathrm{extra}}$) and the missing mass squared (M_{miss}^2) for the signal embedding sample. Additional distributions, including the number of extra clusters in the ROE ($n_{\gamma\mathrm{extra}}$), the beam-constrained mass M_{bc}, the tag probability ($\mathcal{O}_{\mathrm{FEI}}$), and the candidate momentum p_{cand}, are shown in Fig. 5.11. All variables demonstrate good agreement between the embedded signal and expectations.

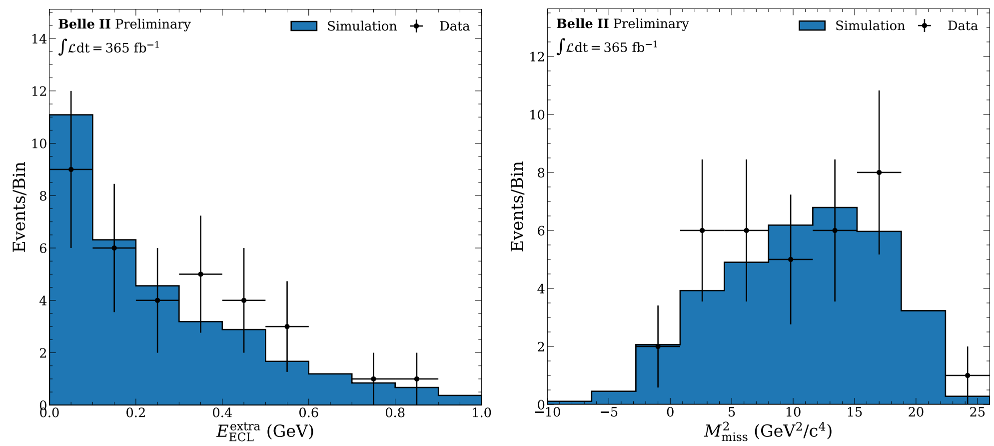

(a) $E_{\mathrm{ECL}}^{\mathrm{extra}}$ distribution in the embedding sample.

(b) M_{miss}^2 distribution in the embedding sample.

Figure 5.10: Distributions of the key variables in the signal embedding sample.

5.8 VALIDATION OF BACKGROUND MODELING USING CONTROL SAMPLES

The accuracy of the MC simulation in modeling both the continuum and $B\bar{B}$ backgrounds is crucial for the reliability of the signal extraction. In this section, we perform a validation of the background templates using dedicated control samples, where the signal contribution is either negligible or absent. These validation regions are defined through specific sideband selections or by

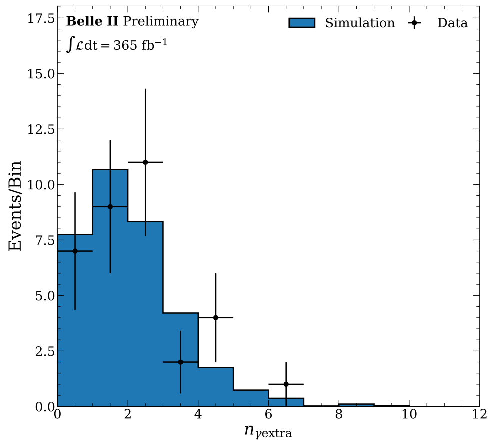

(a) Number of extra clusters ($n_{\gamma\text{extra}}$) in the embedding sample.

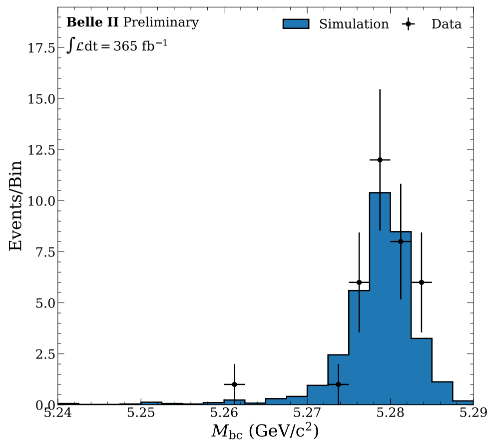

(b) Beam-constrained mass M_{bc} in the embedding sample.

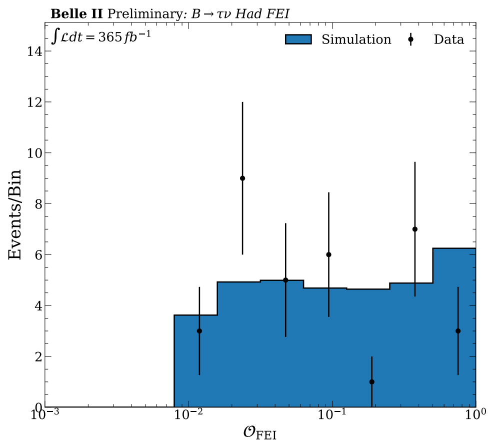

(c) Tag-side signal probability ($\mathcal{O}_{\text{FEI}}$) in the embedding sample.

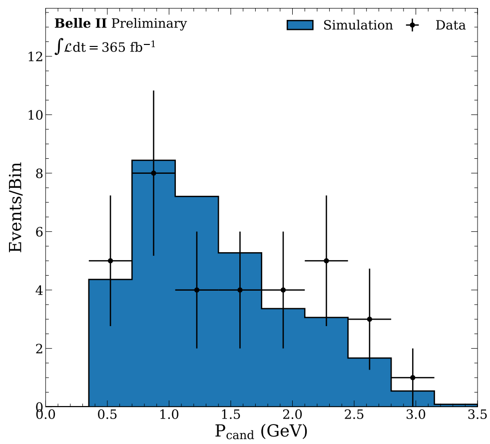

(d) Signal-side candidate momentum p_{cand} in the embedding sample.

Figure 5.11: Distributions of additional observables for the signal embedding sample.

employing off-resonance data, and allow us to evaluate the modeling of key discriminating variables after all corrections are applied.
We consider four sideband regions:

- $E^{\mathbf{extra}}_{\mathbf{ECL}}$ **sideband:** $E^{\text{extra}}_{\text{ECL}} > 500\,\text{MeV}$, used to validate the modeling of high extra energy events, where the signal yield is negligible due to the signal region being restricted to low $E^{\text{extra}}_{\text{ECL}}$.
- M_{bc} **sideband:** $M_{bc} < 5.26\,\text{GeV}/c^2$, targeting events with poor beam-constrained mass, outside the typical signal region.
- M^2_{miss} **sideband (leptonic channels only):** $M^2_{\text{miss}} < 4\,\text{GeV}^2/c^4$, selecting low missing mass events for the lepton channels.
- $p_{\mathbf{cand}}$ **sideband (hadronic channels only):** $p_{\text{cand}} < 1.2\,\text{GeV}/c$, corresponding to candidate momentum values below the signal region for hadronic modes.

For each region, we assess the agreement between data and MC simulations in the fit variables, $E^{\text{extra}}_{\text{ECL}}$ and M^2_{miss}. The goodness of agreement is evaluated visually and through statistical metrics, such as χ^2 tests on one-dimensional distributions. The validation demonstrates satisfactory modeling in all regions, with one exception discussed in Sec. 5.12, where a small excess is observed in the muon channel.

5.9 VALIDATION WITH OFF-RESONANCE DATA

Off-resonance data, collected below the $\Upsilon(4S)$ resonance, contain no $B\bar{B}$ events and thus provide a clean sample for validating the continuum background component. The selection criteria described in Chap. 3 are applied consistently to both data and MC.
Figure 5.12 display the comparison of $E^{\text{extra}}_{\text{ECL}}$ and M^2_{miss} distributions across the four signal channels. The agreement between data and continuum MC is found to be satisfactory, confirming the reliability of the background shape after the reweighting explained in Sec. 3.6.

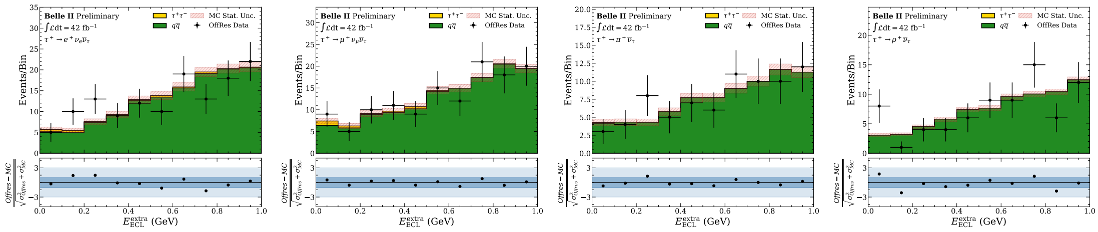

(a) $E_{\mathrm{ECL}}^{\mathrm{extra}}$ for e^+ (b) $E_{\mathrm{ECL}}^{\mathrm{extra}}$ for μ^+ (c) $E_{\mathrm{ECL}}^{\mathrm{extra}}$ for π^+ (d) $E_{\mathrm{ECL}}^{\mathrm{extra}}$ for ρ^+

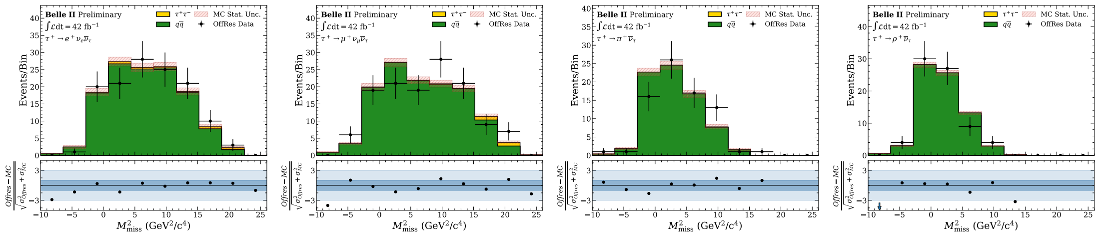

(e) M_{miss}^2 for e^+ (f) M_{miss}^2 for μ^+ (g) M_{miss}^2 for π^+ (h) M_{miss}^2 for ρ^+

Figure 5.12: Comparison of $E_{\mathrm{ECL}}^{\mathrm{extra}}$ and M_{miss}^2 distributions in off-resonance data for the four signal channels.

5.10 $E_{\mathrm{ECL}}^{\mathrm{EXTRA}}$ SIDEBAND VALIDATION

The control region defined by $E_{\mathrm{ECL}}^{\mathrm{extra}} > 500\,\mathrm{MeV}$ ensures negligible signal contamination, as the signal selection requires low $E_{\mathrm{ECL}}^{\mathrm{extra}}$. This sideband is particularly sensitive to the modeling of residual calorimetric energy from particles not associated with the signal candidate ($500 < E_{\mathrm{ECL}}^{\mathrm{extra}} < 1000\,\mathrm{MeV}$ is part of the final fit).
Figure 5.13 show the $E_{\mathrm{ECL}}^{\mathrm{extra}}$ and M_{miss}^2 distributions for all four signal channels after applying all corrections. The level of agreement between data and MC validates the modeling of events with large additional energy deposits in the calorimeter.

5.11 M_{bc} SIDEBAND VALIDATION

The M_{bc} sideband is defined by selecting events with $M_{bc} < 5.26\,\mathrm{GeV}/c^2$, which lie outside the nominal signal window and are thus in correctly reconstructed $B\overline{B}$ events. This region provides a cross-check of background modeling in a region enriched in combinatorial background.

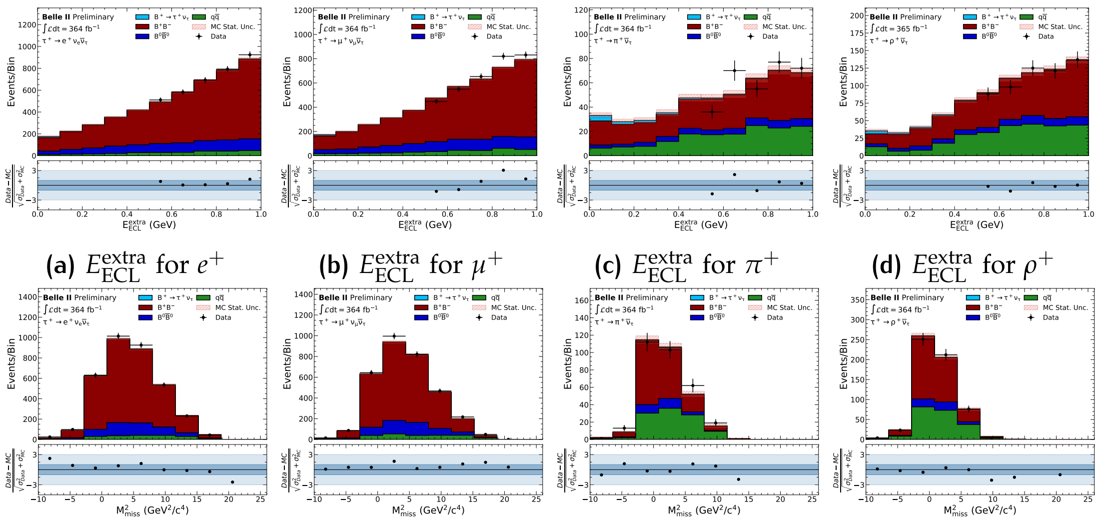

(a) $E_{\text{ECL}}^{\text{extra}}$ for e^+ (b) $E_{\text{ECL}}^{\text{extra}}$ for μ^+ (c) $E_{\text{ECL}}^{\text{extra}}$ for π^+ (d) $E_{\text{ECL}}^{\text{extra}}$ for ρ^+

(e) M^2_{miss} for e^+ (f) M^2_{miss} for μ^+ (g) M^2_{miss} for π^+ (h) M^2_{miss} for ρ^+

Figure 5.13: Distributions of $E_{\text{ECL}}^{\text{extra}}$ (top) and M^2_{miss} (bottom) for the four signal channels in the $E_{\text{ECL}}^{\text{extra}} > 500\,\text{MeV}$ sideband.

Distributions of $E_{\text{ECL}}^{\text{extra}}$ and M^2_{miss} in this sideband, shown in Fig. 5.14, are consistent with the simulation within uncertainties

5.12 M^2_{miss} SIDEBAND VALIDATION FOR LEPTONIC CHANNELS

For the lepton channels (e and μ), we define a control region by selecting $M^2_{\text{miss}} < 4\,\text{GeV}^2/c^4$, corresponding to events with low missing mass, where the signal contribution is suppressed. This region probes the modeling of the $E_{\text{ECL}}^{\text{extra}}$ distribution in events where missing energy from neutrinos is minimal. Figure 5.15 shows the resulting $E_{\text{ECL}}^{\text{extra}}$ distributions. In the electron channel, the agreement is satisfactory. In the muon channel, however, a small discrepancy is observed in the region $0.8 < E_{\text{ECL}}^{\text{extra}} < 1.0\,\text{GeV}$, where data exhibit a $\sim 3\sigma$ excess over the simulation. This excess is traced to specific B_{tag} decay modes, namely $D^0\,\pi^-\,\pi^0$, $D^0\,\pi^-\,\pi^+\,\pi^-$ and $D^0\,\pi^-\,\pi^+\,\pi^-\,\pi^0$, which are slightly mismodeled in the MC. A systematic uncertainty is assigned to account for this discrepancy.

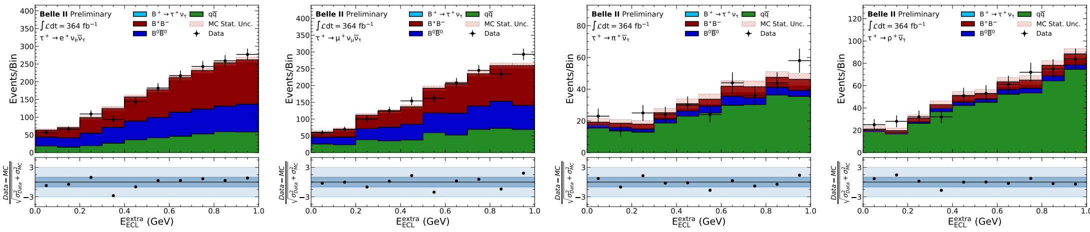

(a) $E^{\text{extra}}_{\text{ECL}}$ in e^+ **(b)** $E^{\text{extra}}_{\text{ECL}}$ in μ^+ **(c)** $E^{\text{extra}}_{\text{ECL}}$ in π^+ **(d)** $E^{\text{extra}}_{\text{ECL}}$ in ρ^+

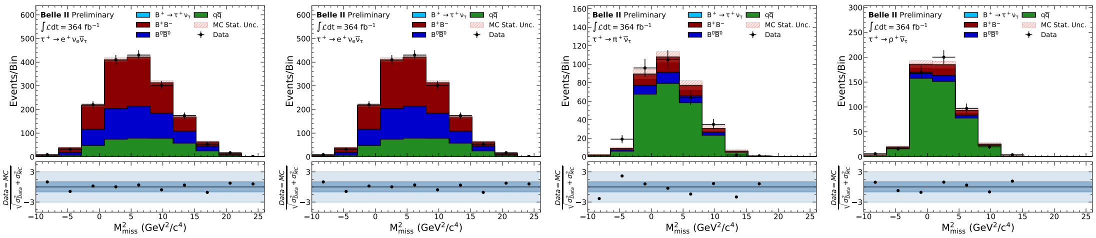

(e) M^2_{miss} in e^+ **(f)** M^2_{miss} in μ^+ **(g)** M^2_{miss} in π^+ **(h)** M^2_{miss} in ρ^+

Figure 5.14: Distributions of $E^{\text{extra}}_{\text{ECL}}$ (top) and M^2_{miss} (bottom) for the four signal channels in the $M_{bc} < 5.26\,\text{GeV}/c^2$ sideband.

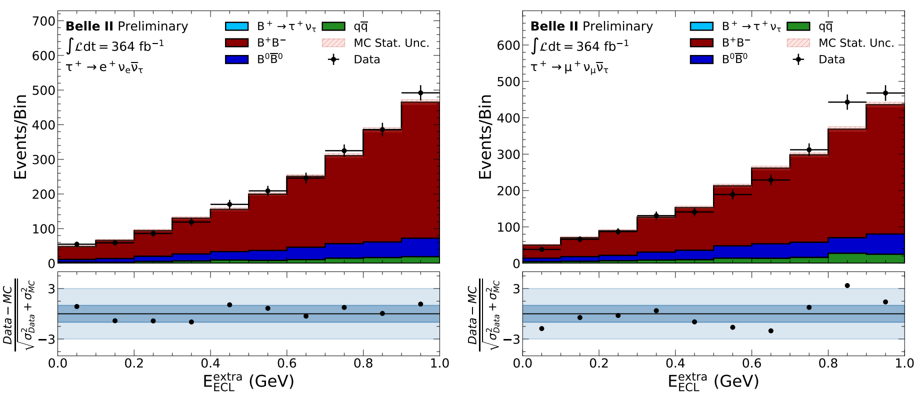

(a) $E^{\text{extra}}_{\text{ECL}}$ in e^+ **(b)** $E^{\text{extra}}_{\text{ECL}}$ in μ^+

Figure 5.15: $E^{\text{extra}}_{\text{ECL}}$ distribution in the leptonic channels after applying all the corrections in the $M^2_{\text{miss}} < 4\,\text{GeV}^2/c^4$ sideband.

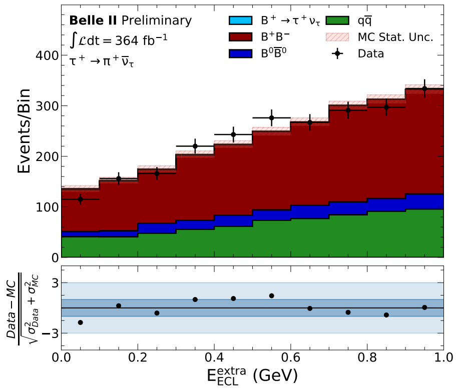

(a) $E_{\text{ECL}}^{\text{extra}}$ in π^+

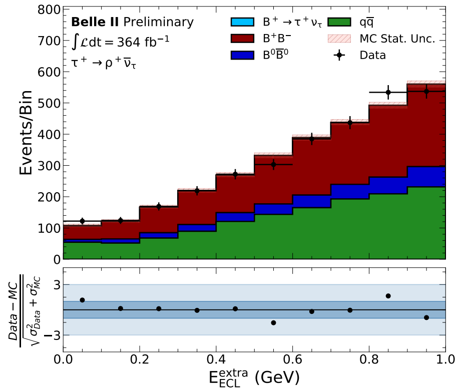

(b) $E_{\text{ECL}}^{\text{extra}}$ in ρ^+

Figure 5.16: $E_{\text{ECL}}^{\text{extra}}$ distribution in the hadronic channels after applying all the corrections in the $p_{\text{cand}} < 1.2\,\text{GeV}/c$sideband.

5.13 p_{CAND} SIDEBAND VALIDATION FOR HADRONIC CHANNELS

In the hadronic channels (π and ρ), we perform a validation using the p_{cand} sideband defined by $p_{\text{cand}} < 1.2\,\text{GeV}/c$. As with other sidebands, the signal yield in this region is negligible, and it provides sensitivity to the modeling of low-momentum candidates.

Figure 5.16 presents the $E_{\text{ECL}}^{\text{extra}}$ distributions in this sideband. The observed agreement between data and MC supports the accurate simulation of $E_{\text{ECL}}^{\text{extra}}$ in hadronic events with low momentum.

6 BRANCHING RATIO EXTRACTION

The extraction of the $B^+ \to \tau^+\nu_\tau$ branching fraction is performed through a 2D simultaneous maximum likelihood fit. The branching fraction is treated as a global floating parameter common to all four reconstructed τ^+ decay modes: $e^+\, \nu_e\, \overline{\nu}_\tau$, $\mu^+\, \nu_\mu\, \overline{\nu}_\tau$, $\pi^+\, \overline{\nu}_\tau$, and $\rho^+\, \overline{\nu}_\tau$. In addition to the signal branching fraction, four independent background yields, one for each τ^+ decay mode, are allowed to float freely in the fit. The Probability Density Functions (PDFs) for both signal and background components are taken from MC simulations, with their shapes being corrected and validated according to the methodologies detailed in Chap. 5. This procedure allows to estimate all the 5 free parameters and their relative statistical uncertainties. Moreover, all systematic uncertainties are evaluated and incorporated separately, as elaborated in Chap. 7. The overall likelihood function for the simultaneous fit is the product of the individual likelihoods corresponding to each of the four τ^+ decay modes, as for the optimization procedure, that is described in Chap. 4. The framework used is RooFit [63], a data modeling and fitting package created at Stanford Linear Accelerator Center, integrated within the Root analysis framework.
The final 2D templates for $E_{\mathrm{ECL}}^{\mathrm{extra}}$ and M_{miss}^2 obtained from simulation for signal and background in the four channels are shown in Fig. 6.1, respectively.

6.1 SENSITIVITY STUDY WITH TOY MONTE CARLO SIMULATIONS

To check the sensitivity of the fit and also to search for potential biases in the measurement, a Toy Monte Carlo (Toy MC) study was performed. This is done by generating 10000 pseudo-experiments based on the expected signal and background distributions. Each pseudo-experiment was constructed by sampling from the 2D PDFs of $E_{\mathrm{ECL}}^{\mathrm{extra}}$ and M_{miss}^2, which were derived from the MC simulations, and rescaled according to the data luminosity and the number of the signal is set to be the PDG mean value [22], $\mathcal{B}_{\mathrm{input}} = 1.09 \times 10^{-4}$. For each of the 10000 pseudo-experiments, a $\mathcal{B}$ and a relative statistical uncertainties is

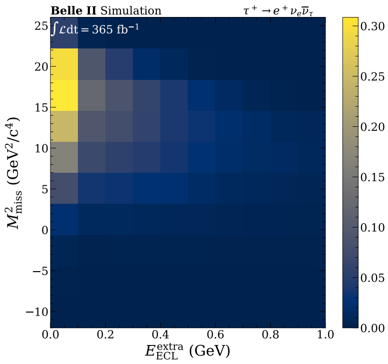

(a) Signal in e^+ channel

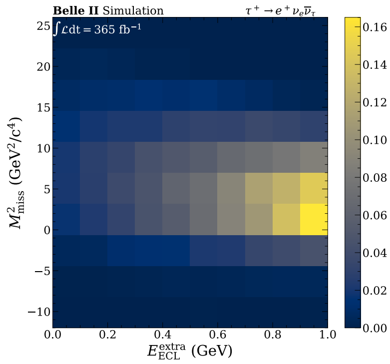

(b) Background in e^+ channel

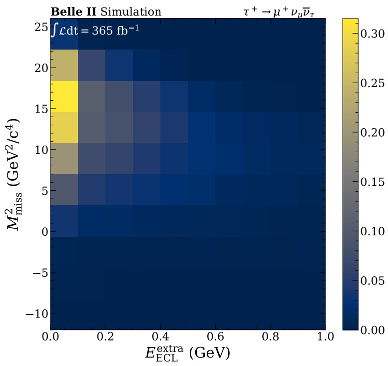

(c) Signal in μ^+ channel

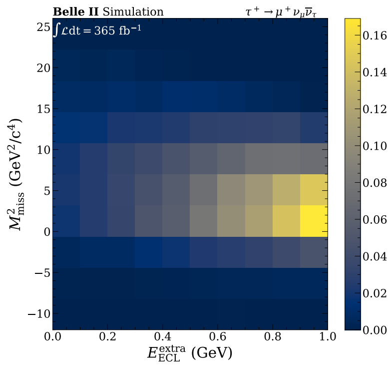

(d) Background in μ^+ channel

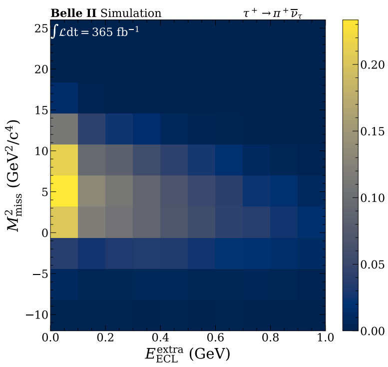

(e) Signal in π^+ channel

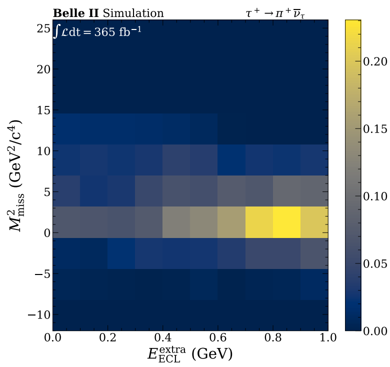

(f) Background in π^+ channel

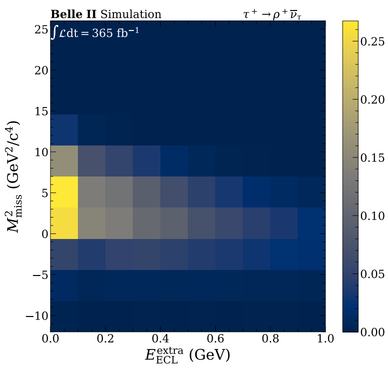

(g) Signal in ρ^+ channel

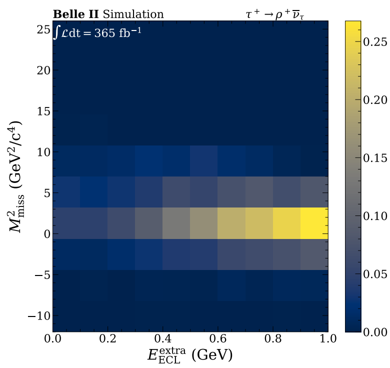

(h) Background in ρ^+ channel

Figure 6.1: 2D distributions of $E^{\mathrm{extra}}_{\mathrm{ECL}}$ and M^2_{miss} for the four τ^+ decay channels. The left column shows the signal distributions, while the right column displays the background distributions.

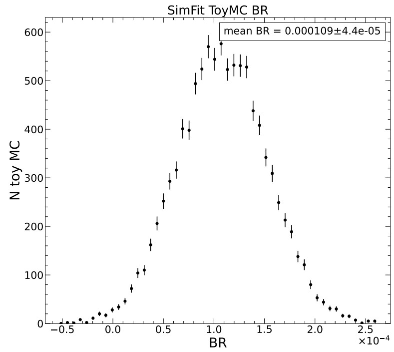

(a) Toy MC results

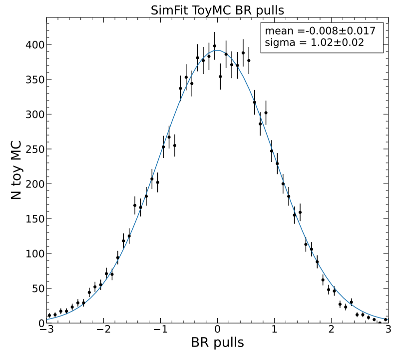

(b) Pull of the Toy MC

Figure 6.2: Distribution of the fitted branching ratios from the Toy MC ensemble (left) and the corresponding pull distribution (right). The pull distribution, defined as $(\mathcal{B}_{\text{fit}} - \mathcal{B}_{\text{input}})/\sigma_{\text{fit}}$, provides a valuable diagnostic for assessing the quality and consistency of the uncertainty estimation

estimated. The mean of the fitted $\mathcal{B}$ values provides an estimate of the central value, while the mean of the uncertainties reflects the expected statistical uncertainty (if the number of the signal event is equal to the PDG expectation value).

The Toy MC study yielded a mean fitted branching ratio of $\mathcal{B}_{\text{TOYs}} = (1.09 \pm 0.45) \times 10^{-4}$. This result indicates an expected statistical uncertainty of 41%, with no significant bias observed in the measurement. Figure 6.2 shows the result of the study.

We also performed a linearity test to search any other source of signal extraction bias. This involved repeating the Toy MC study (10000 pseudo-experiments) for 15 different input signal branching fraction values, ranging from 0.5 to 2 times the nominal PDG value. The results, presented in Fig. 6.3, demonstrate a linear and highly stable slope, with the observed bias remaining within 2% across the entire tested range of input branching fractions. This confirms the reliability of the fitting procedure over a wide range of possible signal strengths.

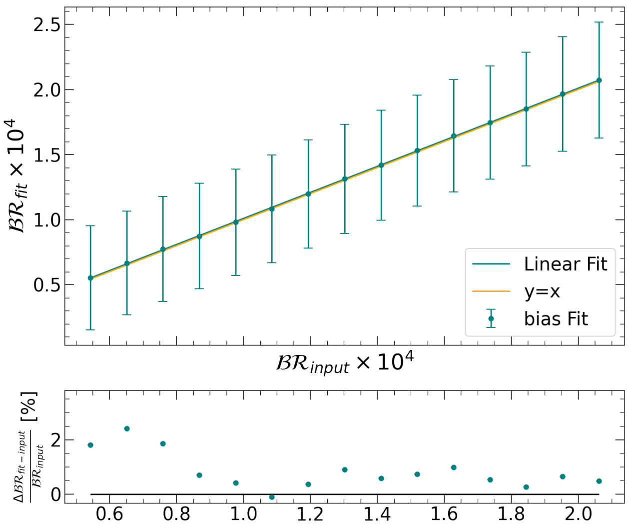

Figure 6.3: Results of various TOY Monte Carlo studies utilizing different Branching Ratio inputs, ranging from $0,5\times$ to $2\times$ the nominal value. **Top panel:** Comparison of Input value *vs.* Fit value (mean of the TOY results). **Bottom panel:** Relative difference in percent.

6.2 FINAL FIT AND RESULT

Following the methodology described before, the branching fraction $\mathcal{B}(B^+ \to \tau^+\nu_\tau)$ is finally extracted from Run1 data. The result of the fit is:

$$\mathcal{B}(B^+ \to \tau^+\nu_\tau) = (1.24 \pm 0.41(\text{stat}) \pm 0.19(\text{syst})) \times 10^{-4} \tag{6.1}$$

where the first uncertainty quantifies the statistical uncertainty arising from the finite data sample, and the second uncertainty represents the total systematic uncertainty. The discussion of the systematic uncertainties and their evaluation is provided in Chap. 7.

Figure 6.4 shows the projections of the post-fit distributions for $E_{\text{ECL}}^{\text{extra}}$ and M_{miss}^2 for each of the four τ^+ decay categories. To enhance the visibility of the signal component, it has been scaled by a factor of 40 for the leptonic channels (e^+ and μ^+) and 20 for the hadronic channels (π^+ and ρ^+). Furthermore, Fig. 6.5 presents the post-fit projections of the $E_{\text{ECL}}^{\text{extra}}$ distribution in the signal-enriched region, specifically for $M_{\text{miss}}^2 > 10\,\text{GeV}^2/c^4$ for leptonic channels and $M_{\text{miss}}^2 > 0.8\,\text{GeV}^2/c^4$ for hadronic channels. This emphasizes the signal contribution in the region where it is most abundant.

The comparison of the fitted background yields to their corresponding Monte Carlo expectations for an integrated luminosity of $365\,\text{fb}^{-1}$ is summarized in Tab. 6.1, while Tab. 6.2 presents the extracted values of $\mathcal{B}(B^+ \to \tau^+\nu_\tau)$ both from the simultaneous fit across all four τ^+ categories and from independent fits performed for each individual category.

The signal strength is observed with a significance of 3.0σ with respect to a background only hypothesis. This significance is determined through the CL_s procedure [64]. The test statistic used is given by $t = -2\log Q = -2\log(\mathcal{L}/\mathcal{L}_0)$, where $\mathcal{L}$ represents the maximum likelihood value obtained when the signal yield is allowed to vary freely, and $\mathcal{L}_0$ corresponds to the maximum likelihood value obtained when the signal yield is constrained to zero (background-only hypothesis). One million pseudo-datasets were generated in under both the hypotheses. The significance of the result is given by the ratio

$$CL_s = \frac{p_{s+b}}{1 - p_b} \tag{6.2}$$

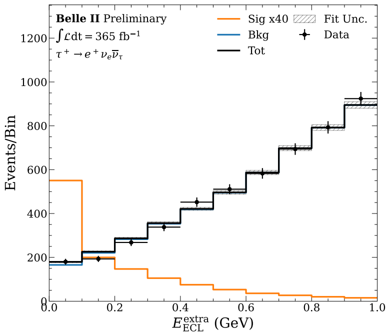

(a) $E_{\mathrm{ECL}}^{\mathrm{extra}}$ in e^+ channel

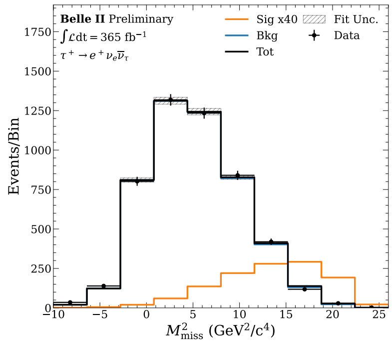

(b) M_{miss}^2 in e^+ channel

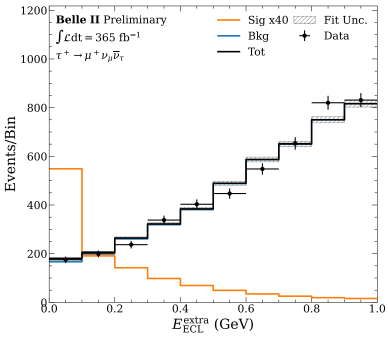

(c) $E_{\mathrm{ECL}}^{\mathrm{extra}}$ in μ^+ channel

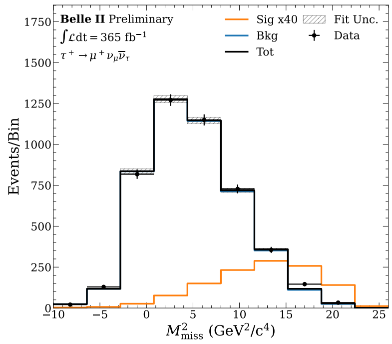

(d) M_{miss}^2 in μ^+ channel

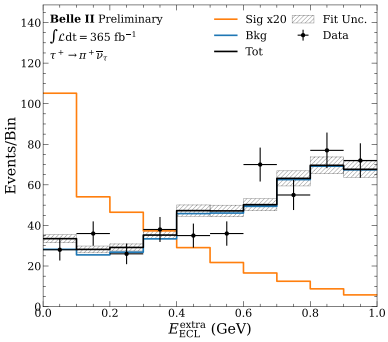

(e) $E_{\mathrm{ECL}}^{\mathrm{extra}}$ in π^+ channel

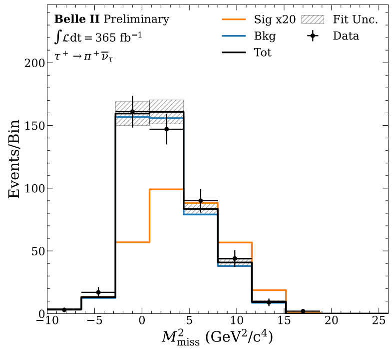

(f) M_{miss}^2 in π^+ channel

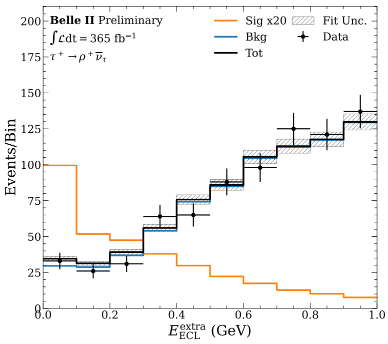

(g) $E_{\mathrm{ECL}}^{\mathrm{extra}}$ in ρ^+ channel

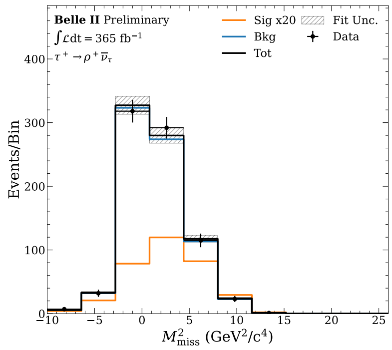

(h) M_{miss}^2 in ρ^+ channel

Figure 6.4: Post-fit projections of $E_{\mathrm{ECL}}^{\mathrm{extra}}$ (left column) and M_{miss}^2 (right column) for the four τ^+ decay channels. The signal component is scaled by a factor of 40 for leptonic channels and 20 for hadronic channels to enhance visibility.

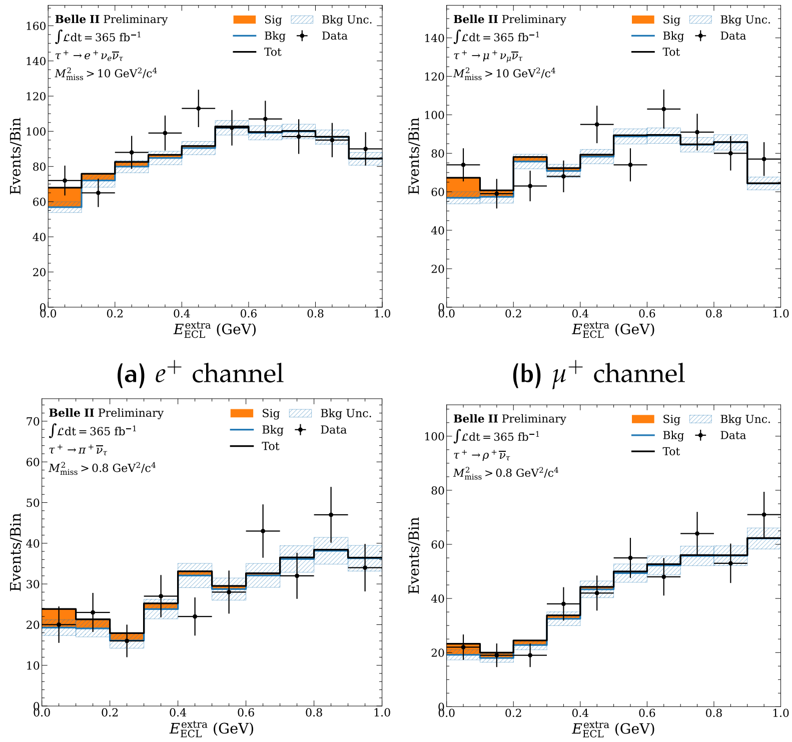

(a) e^+ channel

(b) μ^+ channel

(c) π^+ channel

(d) ρ^+ channel

Figure 6.5: First row: post-fit distributions of $E_{\text{ECL}}^{\text{extra}}$ for the leptonic channels in the signal-enriched region, defined by $M_{\text{miss}}^2 > 10\,\text{GeV}^2/\text{c}^4$. Second row: post-fit distributions of $E_{\text{ECL}}^{\text{extra}}$ for the hadronic channels in the signal-enriched region, defined by $M_{\text{miss}}^2 > 0.8\,\text{GeV}^2/\text{c}^4$.

Table 6.1: Observed and expected (for 365 fb^{-1}) values of the background yields obtained from the fit to the experimental data.

Parameter	Observed value	Expected value
n_{b,e^+}	4907 ± 71	4846 ± 24
n_{b,μ^+}	4620 ± 69	4493 ± 24
n_{b,π^+}	454 ± 22	461 ± 9
n_{b,ρ^+}	772 ± 28	811 ± 11

Table 6.2: Observed values of the signal yields (n_s) and branching fractions ($\mathcal{B}$) for $B^+ \to \tau^+\nu_\tau$, obtained from independent fits for each τ^+ decay mode and from the global simultaneous fit.

Decay mode	n_s	$\mathcal{B}(10^{-4})$
Simultaneous	94 ± 16	1.24 ± 0.41
e^+	13 ± 16	0.51 ± 0.63
μ^+	40 ± 20	1.67 ± 0.83
π^+	31 ± 13	2.28 ± 0.93
ρ^+	6 ± 25	0.42 ± 1.82

6.3 DISCUSSION ON THE RESULT

This thesis presents the first measurement of the branching fraction $\mathcal{B}(B^+ \to \tau^+\nu_\tau)$ by the Belle II experiment. The Belle II result is shown in Fig. 6.6 along with past measurements and the two SM expectation values, one calculated using the exclusive value $|V_{ub}| = (3.43 \pm 0.12) \times 10^{-3}$ and the other with the inclusive one $|V_{ub}| = (4.06 \pm 0.12 \pm 0.11) \times 10^{-3}$ [27]. The Belle II measurement is consistent with the previous measurements and the SM expectations, providing a competitive result to the others.
Assuming the SM, and using $f_B = (190.0 \pm 1.3)$ MeV [65], we extract a measurement of the CKM matrix element

$$|V_{ub}|_{B^+ \to \tau^+\nu_\tau} = [4.41^{+0.74}_{-0.89}] \times 10^{-3}. \tag{6.3}$$

Even though we use a smaller data sample, the statistical uncertainty of this measurement is comparable to the previous hadronic (and semileptonic) tag analysis from BABAR (426 fb^{-1}) [23, 26] and Belle (711 fb^{-1}) [24, 25]. This im-

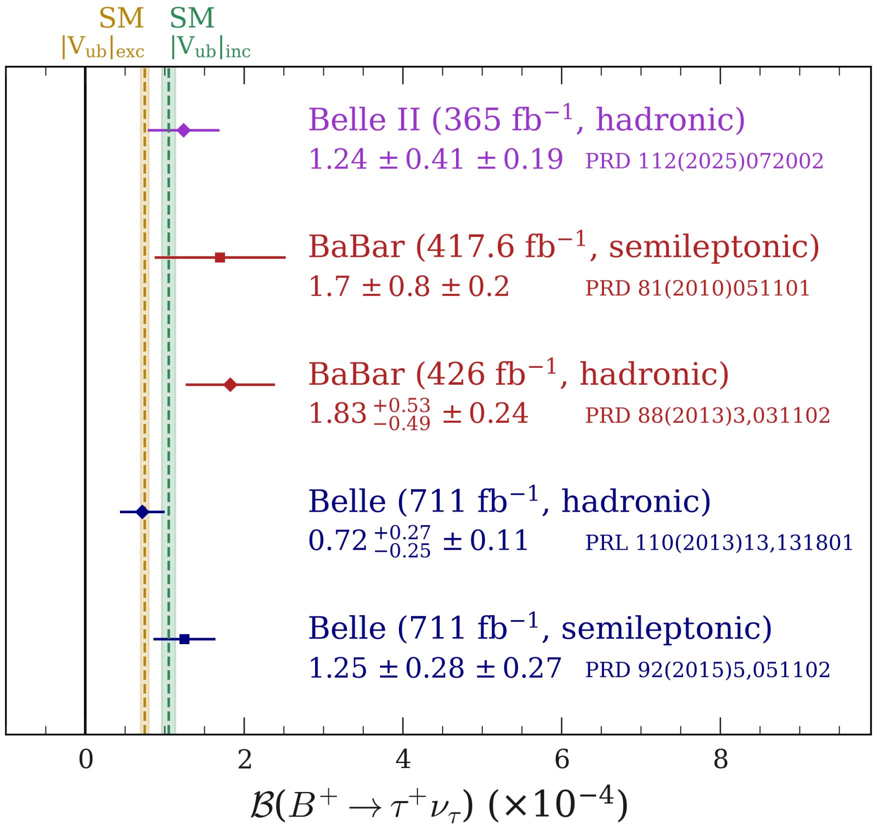

Figure 6.6: Branching fraction $\mathcal{B}(B^+ \to \tau^+\nu_\tau)$ measured by Belle II compared with the past measurements and the two SM expectation values, one calculated using the exclusive value $|V_{ub}| = (3.75 \pm 0.06 \pm 0.19) \times 10^{-3}$ and the other with the inclusive one $|V_{ub}| = (4.06 \pm 0.12 \pm 0.11) \times 10^{-3}$.

proved sensitivity is due to the use of a new B tagging algorithm and an optimized selection.

7 SYSTEMATIC UNCERTAINTIES

In this chapter, we present an evaluation of the systematic uncertainties affecting the measurement of the branching fraction $\mathcal{B}(B^+ \to \tau^+ \nu_\tau)$. Each source of systematic uncertainty is identified, its impact on the final result is quantified, and the methodology used for its evaluation is described.
The sources of systematic uncertainty are assessed by varying the relevant parameters within their estimated uncertainties and propagating these changes through the full analysis chain. This is done by repeating the toy Monte Carlo studies: pseudo-experiments are generated according to the modified probability density functions (PDFs), and the two-dimensional fit to $E_{\text{ECL}}^{\text{extra}}$ and M_{miss}^2 is repeated under these altered assumptions on data. The resulting variation in the extracted branching fraction distribution is then interpreted as the systematic uncertainty.
For systematic effects that do not directly affect the shape or normalization of the signal PDFs, such as the total number of $\Upsilon(4S)$ events, the fraction of B^+B^- pairs produced, and the tracking efficiency, the corresponding uncertainties are propagated directly to the branching fraction.
The full systematic set is described in Tab. 7.1. All the considered sources and the procedures adopted to evaluate their effects are described below:

- **Simulation Statistics:** the limited size of the MC samples introduces statistical fluctuations in the PDF shapes used in the fit. To assess this uncertainty, we fluctuate each bin of the 2D histograms used in the fit according to a Poisson distribution and repeat the full fitting procedure using pseudo-experiments.

- **PDF Corrections for Fit Variables:** corrections to the modeling of fit variables, *i.e.* the multiplicity of neutral clusters ($n_{\gamma\text{extra}}$), are derived from the different control samples for signal and background explained in Chap. 5 and applied to the MC simulation. The associated uncertainty is estimated by varying each bin of the correction map according to a Gaussian distribution with width given by the control-sample statistics. The impact on the fitted branching fraction is then evaluated.

Table 7.1: Summary of relative systematic uncertainties on the fitted branching fraction. The impact of each source is evaluated from the simultaneous fit of the four τ decay modes. The last three contributions affect only the normalization and not the signal yield.

Source	Relative Uncertainty (%)
Simulation statistics	13.3
Fit variable PDF corrections	5.5
Branching fractions in MC	4.1
Tag-side B reconstruction efficiency	2.2
Continuum reweighting	1.9
π^0 reconstruction efficiency	0.9
Continuum normalization	0.7
Particle identification	0.6
Number of $B\bar{B}$ pairs	1.5
Fraction of B^+B^- pairs	2.1
Tracking efficiency	0.2
Total	15.5

- **Branching Fractions in the Simulation:** the decay branching fractions of B and D mesons in the simulation are varied within the uncertainties reported by the Particle Data Group (PDG) [22]. These variations are propagated through the generation of alternative MC PDFs, and the fit is repeated to determine the resulting change in the signal yield.

- **Tag-side Reconstruction Efficiency:** the reconstruction efficiency of the hadronic tag side is calibrated using $B^+ \to X\ell^+\nu_\ell$ and $B^+ \to D^{(*)}\pi^+$ decays. We derive a covariance matrix from the calibration and generate alternative efficiency correction maps to estimate the corresponding systematic uncertainty.

- **Continuum Reweighting:** the limited statistics of the off-resonance dataset used to train the FastBDT classifier for continuum suppression introduces uncertainty in the reweighting procedure. A bootstrapping method is employed to resample the training and test datasets multiple times, thereby generating different sets of reweighting weights. The observed spread in the fitted branching fraction is used to quantify the uncertainty.

- π^0 **Reconstruction Efficiency:** for $\tau^+ \to \rho^+ \, \bar{\nu}_\tau$, mismodeling of the π^0 reconstruction efficiency in simulation can affect the signal yield. We study this effect using control samples of $D^{*0} \to D^0 \, \pi^0$, with $D^0 \to K^- \, \pi^+ \, (\pi^0)$, in different momentum regions. Correction factors are derived and applied to the simulation. To quantify the residual uncertainty, a π^0 removal procedure is implemented, in which π^0 candidates are probabilistically removed according to their efficiency correction uncertainties, and moved to $\tau^+ \to \pi^+ \, \bar{\nu}_\tau$ category, and the impact on the branching fraction is assessed.

- **Continuum Normalization:** the overall normalization of the continuum background is varied within the statistical uncertainty of the off-resonance dataset. This is implemented by fluctuating the continuum component using a Poisson distribution and repeating the fit.

- **Particle Identification Efficiency:** systematic uncertainties related to the efficiency and misidentification rates of particle identification (PID) algorithms are estimated using high-purity control samples such as $D^{*+} \to D^0 \, (\to K^- \, \pi^+)\pi^+$, $\Lambda^0 \to p \, \pi^-$, $K^0_S \to \pi^+ \, \pi^-$, and $J/\psi \to \ell^+\ell^-$. PID efficiencies and fake rates are varied within their uncertainties, and the resulting changes in selection efficiencies and fit PDFs are propagated to the final result.

- **Number of $B\bar{B}$ Pairs:** the total number of $\Upsilon(4S)$ decays is determined through a dedicated $\Upsilon(4S)$ counting analysis. In this procedure, the number of events collected at the $\Upsilon(4S)$ resonance is measured by removing the non-resonant contribution using data collected below the $\Upsilon(4S)$ threshold (off-resonance data), properly scaled by luminosity and cross-section ratios. The associated uncertainty is treated as a global normalization uncertainty and propagated directly to the branching fraction.

- **Fraction of B^+B^- Pairs:** the fraction of B^+B^- events produced at the $\Upsilon(4S)$ is taken from the latest HFLAV report [27]. Its uncertainty is propagated directly to the final result.

- **Tracking Efficiency:** the uncertainty in the track reconstruction efficiency is assessed using control samples and propagated as a global normalization uncertainty, based on the number of tracks in the signal final state (1 track).

CONCLUSIONS

Semi-leptonic and purely leptonic decays of B mesons provide a powerful laboratory for testing the flavour structure of the standard models. Among these, purely leptonic decays such as $B^+ \to \tau^+\nu_\tau$ offer a clean probe of the charged-current interaction mediated by the weak force. These processes occur via the annihilation of the constituent quarks in the B meson, specifically through the $b \to u$ transition, and are directly sensitive to the product of the Cabibbo-Kobayashi-Maskawa (CKM) matrix element $|V_{ub}|$ and the B-meson decay constant f_B.
Despite being helicity suppressed in the SM, the decay $B^+ \to \tau^+\nu_\tau$ is the most experimentally accessible among the purely leptonic B decays due to the comparatively large mass of the τ lepton, which partially compensates for the suppression. Importantly, this decay provides a complementary approach to the extraction of $|V_{ub}|$ with respect to semi-leptonic decays, with a negligible theoretical uncertainty (only f_B contributes). It is also sensitive to potential contributions from physics beyond the standard model, such as charged Higgs bosons in Two-Higgs-Doublet Model (2HDM).
From a theoretical standpoint, the decay rate prediction within the SM is relatively clean, as it depends on well-defined quantities such as $|V_{ub}|$, f_B, and the B^+ lifetime, allowing a direct confrontation between experimental results and SM expectations.
The SM prediction for the branching fraction reads:

$$\mathcal{B}(B^+ \to \tau^+\nu_\tau) = \frac{G_F^2 m_B m_\tau^2}{8\pi}\left(1 - \frac{m_\tau^2}{m_B^2}\right)^2 f_B^2 |V_{ub}|^2 \tau_{B^+}, \tag{7.1}$$

where G_F is the Fermi constant, m_B and m_τ are the masses of the B^+ meson and the τ lepton, respectively, f_B is the B-meson decay constant, $|V_{ub}|$ is the CKM matrix element, and τ_{B^+} is the B^+ lifetime.
The measurement of the branching fraction of the decay $B^+ \to \tau^+\nu_\tau$ is a challenging task due to the presence of large backgrounds and the need for precise event reconstruction. The Belle II experiment, with its high luminosity and advanced detector technology, provides an excellent environment for such measurements. The analysis presented in this thesis focuses on the extraction of

the branching fraction of this decay using data collected by the Belle II detector at the SuperKEKB accelerator.
The analysis is based on a dataset corresponding to an integrated luminosity of approximately $365\,\mathrm{fb}^{-1}$, collected at the $\Upsilon(4S)$ resonance. The event selection strategy involves a combination of kinematic and topological criteria to isolate the signal from the background. The signal is identified by tagging the events with the Full Event Interpretation (FEI), which selects all the hadronic B decay and then search all the 1-prong event in the decay products of the other B meson.
The branching fraction is extracted using a simultaneous fit to $E_{\mathrm{ECL}}^{\mathrm{extra}}$ *vs.* M_{miss}^2 template, calibrated and validated on the simulation. The systematic uncertainties associated with the measurement are evaluated, including contributions from the modeling of the background, the uncertainties in the statistics of simulation, and any others source.
The results of this analysis is:

$$\mathcal{B}(B^+ \to \tau^+ \nu_\tau) = (1.24 \pm 0.41(\mathrm{stat}) \pm 0.19(\mathrm{syst})) \times 10^{-4} \tag{7.2}$$

This kind of measurement are part of the European Strategy for Particle Physics, both for Belle II [66] and FCC$-ee$ [67].
The result was reported in Ref. [68], and it was presented at the 2025 Moriond electroweak conference [69] for the first time.

A THE FULL EVENT INTERPRETATION

In e^+e^- collider experiments such as Belle and Belle II, the full reconstruction of $\Upsilon(4S)$ events is a key technique for studying B-meson decays. Two complementary strategies are commonly employed: tagged and untagged analyses. In both cases the well-known initial state provided by the tuned beam energies allows one to exploit overall four-momentum conservation to constrain the signal decay. The following appendix summarise these approaches and give an overview of the Full Event Interpretation (FEI) [70], the machine-learning based hadronic tagger used at Belle II, which is an update of the Full Reconstruction (FR) algorithm developed for Belle.

A.1 RECONSTRUCTION METHODS

A.1.1 Untagged analysis

Untagged analyses reconstruct only the B_{sig} candidate and treat all remaining reconstructed objects as originating from the other B meson. Selections on these remaining particles suppress background and favour event topologies consistent with B decays. Without an explicit B_{tag} reconstruction one normally assumes that any neutrinos in the event belong to the signal decay; this allows an estimate of the signal-neutrino four-momentum, but generally with poorer resolution than in the tagged case.

A.1.2 Tagged analysis

In a tagged analysis both the signal-side B meson (B_{sig}) and the accompanying B meson (B_{tag}) are reconstructed. The B_{tag} is reconstructed in exclusive decay channels, either hadronic or semileptonic. The chosen tag mode strongly influences how missing momentum is interpreted. Neutrinos escape detection and therefore remove undetectable four-momentum from the visible final state. If the B_{tag} is reconstructed hadronically, neutrino only comes from the signal side,

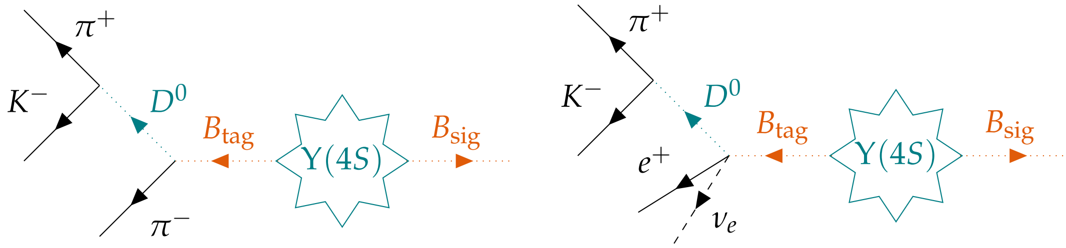

(a) Hadronic Tag **(b)** Semileptonic Tag

Figure A.1: Schematics examples of $\Upsilon(4S)$ event reconstruction in tagged analyses. Dashed lines represent undetected neutrinos. Dotted lines represent non stable particles.

so all the missing momentum can be attributed to it. If the B_{tag} is semileptonic, neutrinos may be present on both sides of the event and the signal neutrino momentum cannot be determined uniquely from kinematics alone. Schematic tagged topologies for hadronic and semileptonic tags are shown in Figs. A.1a and A.1b, respectively.

Beyond kinematic constraints, these kind of reconstruction approaches differ in their tagging efficiency (the fraction of $\Upsilon(4S)$ events that can be tagged), their tag-side efficiency (the fraction of $\Upsilon(4S)$ events with a correctly reconstructed tag), and the quality of the recovered information, which determines the purity (the fraction of tagged $\Upsilon(4S)$ events with a correct tag-side reconstruction). These three quantities serve as key performance indicators for tagging algorithms. They directly impact critical aspects of any analysis: the tagging efficiency determines the disk-space requirements for skimmed datasets (i.e. the number of events that must be retained for analysis); the tag-side efficiency influences the effective statistical power of the measurement; and the purity is related to the signal-to-background ratio. The relative advantages and trade-offs of these complementary approaches are illustrated in Fig. A.2.

A.2 OVERVIEW OF THE FULL EVENT INTERPRETATION

The FEI is the standard tagging algorithm in `basf2`; it applies multivariate classifiers to distinguish correctly reconstructed decay chains from combinatorial background, building on the original Full Reconstruction (FR) method used at Belle, while introducing algorithmic and performance improvements.

The FEI employs a hierarchical, staged training strategy. Detector-level objects

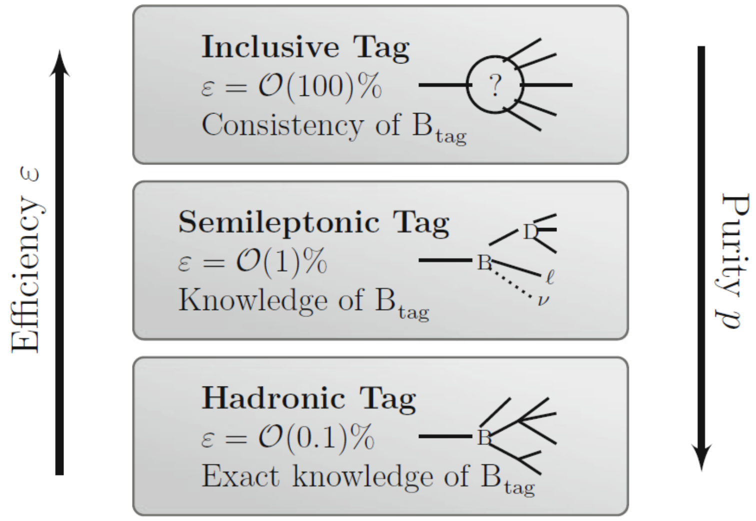

Figure A.2: Overview of the three tagging algorithms, which were used in the past to infer information about the B_{sig} meson using the other B_{tag} meson in the event

(tracks, electromagnetic and KLM clusters) are first combined into final-state particle candidates. A dedicated multivariate classifier (MVC) is trained for each particle type using inputs appropriate for that particle; the classifier output (SignalProbability) quantifies the likelihood that a candidate is correctly reconstructed and is propagated as an input to higher-level classifiers. Final-state candidates are combined into intermediate resonances, which in turn are combined into B-meson candidates, with channel-specific classifiers at each stage. Training proceeds stage by stage so that the probability and other lower-level information improve the quality of higher-level candidates. The hierarchical structure of the FEI is illustrated in Fig. A.3. All FEI classifiers are implemented as boosted decision trees and trained with the FastBDT framework [62] using large simulated samples with MC truth labels.

A.2.1 Input variables for classifier training

The following variables are used as inputs to the FEI multivariate classifiers. Variables are given for final-state particles (FSPs) and for typical intermediate particles; in many cases both kinematic and quality variables are used, and lower-level probability are included to exploit the hierarchical training.

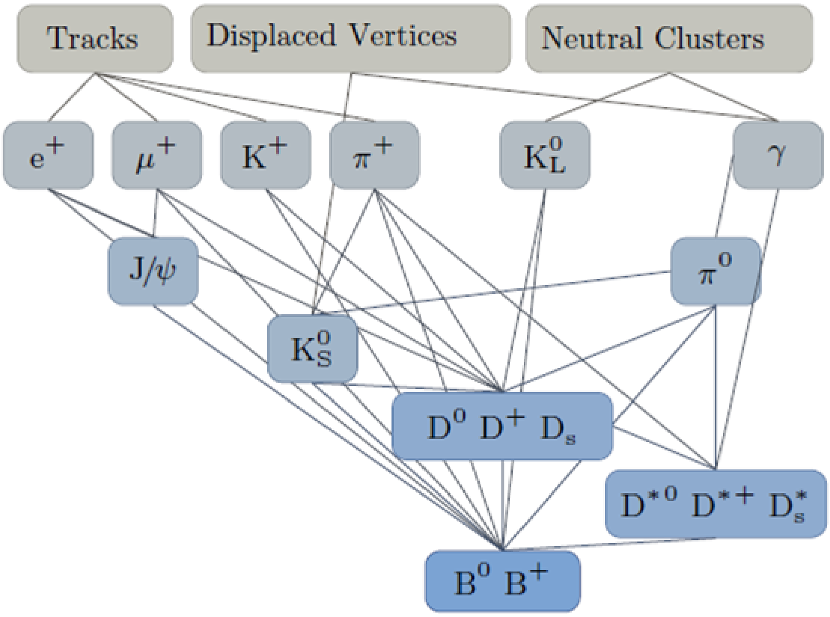

Figure A.3: Schematic overview of the hierarchical structure of the FEI algorithm. B-meson candidates are reconstructed bottom-up from detector-level objects: final-state particles are formed from tracks and clusters, combined into intermediate resonances, and ultimately assembled into B candidates. At each stage, a dedicated multivariate classifier assigns a probability that quantifies the likelihood of correct reconstruction. These probabilities are propagated as input features to subsequent stages, thereby enhancing discrimination power at higher levels of the decay hierarchy.

Final-state particles

For charged particles (electrons, muons, pions, kaons, protons), the FEI uses particle identification likelihood or likelihood-ratio scores (*e.g.* `electronID`, `muonID`, `kaonID`, `protonID`), with pion candidates typically identified by small values of the other PID scores. Kinematic variables include total momentum p, transverse momentum p_T, and longitudinal momentum p_z. Impact parameters, radial and longitudinal distances (`dr`, `dz`) to the interaction point, discriminate promptly produced tracks from displaced daughters, and the track χ^2 probability quantifies fit quality. After pre-selection, candidates are ranked (*e.g.* by PID score) and only the top entries are retained.
For photons, cluster properties such as the number of crystals hit, cluster region (forward/barrel/backward), cluster timing, and shape variables (*e.g.* E_9/E_{25}) in the electromagnetic calorimeter (ECL) are used alongside energy and momentum (E, p_T, p_z). After pre-selection by energy, the best candidates are retained. For K^0_L candidates, energy-like estimators and KLM cluster timing discriminate true K^0_L signals from background.

Intermediate particles

For π^0 mesons, the FEI uses the invariant mass M and mass deviation $|dM| = |M - M_{\pi^0}|$, the opening angle between the two daughter photons, daughter photon output probability, and kinematic variables such as energy E, transverse momentum p_T, and longitudinal momentum p_z. The best candidates are retained after pre-selection.
For long-lived neutral hadrons (K^0_S, Λ, Σ), vertex displacement variables such as decay distance, `dr`, `dz`, and their significances are crucial. The vertex fit quality is quantified by the χ^2 probability for the decay-vertex fit, and angular consistency is assessed via the angle between the momentum vector and the vector from the interaction point to the decay vertex. Invariant mass and $|dM|$ relative to the nominal mass, together with daughter kinematics, distance variables, and output probability.
For charm hadrons and quarkonia (Λ_c, J/ψ, $D_s^{0,\pm}$, ...), the classifiers exploit individual daughter probability and their product, vertex fit χ^2 probabilities for the parent and daughters (where applicable), invariant mass deviations ($|dM|$), and, where relevant, released energy Q. Decay kinematics such as decay angles and daughter momenta in the parent rest frame are included, along with a decay-mode identifier (`decayModeID`) when multiple channels are supported. After pre-selection, typically the top 20 candidates are retained.

B mesons

For B^0 and B^+ candidates, the FEI classifiers combine the daughter probability values, both individually and as their product, with vertex and kinematic information to distinguish correctly reconstructed B mesons from combinatorial background. The vertex fit quality is quantified by the χ^2 probability of the B-meson decay vertex and by the χ^2 probabilities of the daughter track fits or secondary decay vertices where applicable. Kinematic inputs include the magnitudes of the rest-frame momentum vectors for each daughter, as well as distance variables that characterise the displacement of the B vertex: the magnitude of the distance vector together with its radial component `dr` and Cartesian components `dx`, `dy`, and `dz`, all accompanied by their respective significances. The angle between the vertex position vector and the B-meson momentum vector provides additional consistency information, while decay angles between the B meson and each daughter, as well as between pairs of daughters, capture correlations in the decay topology.
A particularly important discriminating variable is the energy difference ΔE, defined as the difference between the energy E_B of the B-meson candidate in the $\Upsilon(4S)$ centre-of-mass frame and the beam energy E_{beam}, *i.e.* $\Delta E = E_B - E_{\text{beam}}$. The beam energy corresponds to half of the available energy in the centre-of-mass system. Since the $\Upsilon(4S)$ decays to two B mesons of equal mass, correctly reconstructed B candidates should exhibit values of ΔE close to zero. This strong kinematic constraint makes ΔE one of the most powerful inputs for separating signal from background, and it is therefore a central feature in the training of the B-meson classifiers. In addition, the decay-mode identifiers (`decayModeID`) of each daughter are included to allow the classifier to learn mode-specific response patterns. To manage combinatorics, B-meson candidates are ranked according to the product of their daughters' $\mathcal{O}_{\text{FEI}}$ values, and only the top 20 are retained and passed to the classifier; this ranking information is also provided as an input feature to the training algorithm.

A.2.2 Comparison with Belle Full Reconstruction

The Belle Full Reconstruction (FR) algorithm is the conceptual predecessor to the FEI, sharing the hierarchical reconstruction strategy and stage-wise classifier training. However, the FEI introduces several key algorithmic improvements and performance enhancements.
The FR algorithm relied on the external NeuroBayes package [71] for multivariate classification, whereas the FEI employs the FastBDT framework [62], which

implements stochastic gradient-boosted decision trees. This transition has substantially reduced the training time from weeks to days, while maintaining or improving classification performance. The FEI provides a fully automated and user-configurable training pipeline: analysts specify the desired configuration, and the algorithm executes the complete training procedure without further manual intervention, significantly improving usability and reproducibility.

A major advancement of the FEI is its support for both hadronic and semileptonic B-meson decay modes, whereas the FR was restricted to hadronic tags only. This dual-mode capability expands the range of physics analyses accessible with tagged methods. Users may optionally disable either hadronic or semileptonic modes during training to reduce computational overhead when only one tagging category is required.

The FEI substantially increases the number of exclusive decay channels relative to the FR. At the time of this study, the FEI incorporated 36 hadronic charged and 31 hadronic neutral B-meson decay modes, compared to 17 and 15, respectively, in the FR. Including 42 charged and 39 neutral semileptonic modes, the FEI reconstructs over 4000 exclusive decay chains, compared to approximately 1000 for the FR.

The full hadronic charged B decay-mode coverage of the FEI is summarised in Tab. A.2, and the neutral B modes are listed in Tab. A.1. All the intermediate particle decay modes supported by the hadronic FEI algorithm are detailed in Tab. A.3.

The increased decay-mode coverage directly translates into substantial improvements in tag-side efficiency. While untagged analyses trivially achieve 100% tag-side efficiency, since no explicit B_{tag} reconstruction is required, tagged analyses typically exhibit much lower values: approximately 0.1% for hadronic tags and 1% for semileptonic tags. Performance studies [70] demonstrate that the FEI more than doubles the hadronic tag-side efficiency achieved by the FR: from 0.28% to 0.76% for B^+ tags, and from 0.18% to 0.46% for B^0 tags. For semileptonic tagging, the FEI achieves maximum tag-side efficiencies of 1.80% and 2.04% for charged and neutral tags, respectively. These efficiency gains directly enhance the statistical power of Belle II analyses employing the tagging method.

Table A.1: Hadronic neutral B-meson decay channels supported by the FEI algorithm, with their `decayModeID` (`dmID`) flags.

`dmID`	Channel ($B^0 \to$)	`dmID`	Channel ($B^0 \to$)
0	$D^- \pi^+$	16	$D^{*-} \pi^+ \pi^0$
1	$D^- \pi^+ \pi^0$	17	$D^{*-} \pi^+ \pi^0 \pi^0$
2	$D^- \pi^+ \pi^0 \pi^0$	18	$D^{*-} \pi^+ \pi^+ \pi^+ \pi^-$
3	$D^- \pi^+ \pi^+ \pi^+ \pi^-$	19	$D^{*-} \pi^+ \pi^+ \pi^- \pi^0$
4	$D^- \pi^+ \pi^+ \pi^- \pi^0$	20	$D_s^{*+} D^-$
5	$\bar{D}^0 \pi^+ \pi^-$	21	$D_s^+ D^{*-}$
6	$D^- D^0 K^+$	22	$D_s^{*+} D^{*-}$
7	$D^- D^{*0} K^+$	23	$J/\psi K_S^0$
8	$D^{*-} D^0 K^+$	24	$J/\psi K^+ \pi^-$
9	$D^{*-} D^{*0} K^+$	25	$J/\psi K_S^0 \pi^+ \pi^-$
10	$D^- D^+ K_S^0$	26	$\bar{\Lambda}_c^- p \pi^+ \pi^-$
11	$D^{*-} D^+ K_S^0$	27	$\bar{D}^0 p \bar{p}$
12	$D^- D^{*+} K_S^0$	28	$D^- p \bar{p} \pi^+$
13	$D^{*-} D^{*+} K_S^0$	29	$D^{*-} p \bar{p} \pi^+$
14	$D_s^+ D^-$	30	$\bar{D}^0 p \bar{p} \pi^+ \pi^-$
15	$D^{*-} \pi^+$	31	$\bar{D}^{*0} p \bar{p} \pi^+ \pi^-$

Table A.2: Hadronic charged B-meson decay channels supported by the FEI algorithm, with their `decayModeID` (`dmID`) flags.

`dmID`	Channel ($B^+ \to$)	`dmID`	Channel ($B^+ \to$)
0	$\overline{D}^0\ \pi^+$	18	$\overline{D}^{*0}\ \pi^+\ \pi^+\ \pi^-$
1	$\overline{D}^0\ \pi^+\ \pi^0$	19	$\overline{D}^{*0}\ \pi^+\ \pi^+\ \pi^-\ \pi^0$
2	$\overline{D}^0\ \pi^+\ \pi^0\ \pi^0$	20	$D_s^{*+}\ \overline{D}^0$
3	$\overline{D}^0\ \pi^+\ \pi^+\ \pi^-$	21	$D_s^+\ \overline{D}^{*0}$
4	$\overline{D}^0\ \pi^+\ \pi^+\ \pi^-\ \pi^0$	22	$\overline{D}^0\ K^+$
5	$\overline{D}^0\ D^+$	23	$D^-\ \pi^+\ \pi^+$
6	$\overline{D}^0\ D^+\ K_S^0$	24	$D^-\ \pi^+\ \pi^+\ \pi^0$
7	$\overline{D}^{*0}\ D^+\ K_S^0$	25	$J/\psi\ K^+$
8	$\overline{D}^0\ D^{*+}\ K_S^0$	26	$J/\psi\ K^+\ \pi^+\ \pi^-$
9	$\overline{D}^{*0}\ D^{*+}\ K_S^0$	27	$J/\psi\ K^+\ \pi^0$
10	$\overline{D}^0\ D^0\ K^+$	28	$J/\psi\ K_S^0\ \pi^+$
11	$\overline{D}^{*0}\ D^0\ K^+$	29	$\overline{\Lambda}_c^-\ p\ \pi^+\ \pi^0$
12	$\overline{D}^0\ D^{*0}\ K^+$	30	$\overline{\Lambda}_c^-\ p\ \pi^+\ \pi^-\ \pi^+$
13	$\overline{D}^{*0}\ D^{*0}\ K^+$	31	$\overline{D}^0\ p\ \overline{p}\ \pi^+$
14	$D_s^+\ \overline{D}^0$	32	$\overline{D}^{*0}\ p\ \overline{p}\ \pi^+$
15	$\overline{D}^{*0}\ \pi^+$	33	$D^+\ p\ \overline{p}\ \pi^+\ \pi^-$
16	$\overline{D}^{*0}\ \pi^+\ \pi^0$	34	$D^{*+}\ p\ \overline{p}\ \pi^+\ \pi^-$
17	$\overline{D}^{*0}\ \pi^+\ \pi^0\ \pi^0$	35	$\overline{\Lambda}_c^-\ p\ \pi^+$

Table A.3: Decay modes of intermediate particles supported by the hadronic FEI algorithm, with their `decayModeID` (`dmID`) flags.

`dmID`	Channel	`dmID`	Channel	`dmID`	Channel
			π^0		
0	$\pi^0 \to \gamma\ \gamma$				
			K_S^0		
0	$K_S^0 \to \pi^+\ \pi^-$	1	$K_S^0 \to \pi^0\ \pi^0$		
			J/ψ		
0	$J/\psi \to e^+e^-$	1	$J/\psi \to \mu^+\mu^-$		
			D^0		
0	$D^0 \to K^-\ \pi^+$	1	$D^0 \to \pi^-\ \pi^+$	2	$D^0 \to K_S^0\ \pi^+\ \pi^-$
3	$D^0 \to K^-\ \pi^+\ \pi^0$	4	$D^0 \to \pi^-\ \pi^+\ \pi^+\ \pi^-$	5	$D^0 \to K_S^0\ \pi^+\ \pi^-\ \pi^0$
6	$D^0 \to K^-\ \pi^+\ \pi^0\ \pi^0$	7	$D^0 \to \pi^-\ \pi^+\ \pi^0$	8	$D^0 \to K^-\ K^+$
9	$D^0 \to K^-\ \pi^+\ \pi^+\ \pi^-$	10	$D^0 \to \pi^-\ \pi^+\ \pi^0\ \pi^0$	11	$D^0 \to K^-\ K^+\ \pi^0$
12	$D^0 \to K^-\ \pi^+\ \pi^+\ \pi^-\ \pi^0$	13	$D^0 \to K_S^0\ \pi^0$	14	$D^0 \to K^-\ K^+\ K_S^0$
			D^+		
0	$D^+ \to K^-\ \pi^+\ \pi^+$	1	$D^+ \to \pi^+\ \pi^0$	2	$D^+ \to K_S^0\ \pi^+\ \pi^0$
3	$D^+ \to K^-\ \pi^+\ \pi^+\ \pi^0$	4	$D^+ \to \pi^+\ \pi^+\ \pi^-$	5	$D^+ \to K_S^0\ \pi^+\ \pi^+\ \pi^-$
6	$D^+ \to K^-\ K^+\ \pi^+$	7	$D^+ \to \pi^+\ \pi^+\ \pi^-\ \pi^0$	8	$D^+ \to K^+\ K_S^0\ K_S^0$
9	$D^+ \to K^-\ K^+\ \pi^+\ \pi^0$	10	$D^+ \to K_S^0\ \pi^+$		
			D^{*0}		
0	$D^{*0} \to D^0\ \pi^0$	1	$D^{*0} \to D^0\ \gamma$		
			D^{*+}		
0	$D^{*+} \to D^0\ \pi^+$	1	$D^{*+} \to D^+\ \pi^0$	2	$D^{*+} \to D^+\ \gamma$
			D_s^+		
0	$D_s^+ \to K^+\ K_S^0$	1	$D_s^+ \to K^+\ K^-\ \pi^+\ \pi^+\ \pi^-$	2	$D_s^+ \to \pi^+\ \pi^+\ \pi^-$
3	$D_s^+ \to K^+\ \pi^+\ \pi^-$	4	$D_s^+ \to K^+\ K_S^0\ \pi^+\ \pi^-$	5	$D_s^+ \to K_S^0\ \pi^+$
6	$D_s^+ \to K^+\ K^-\ \pi^+$	7	$D_s^+ \to K^-\ K_S^0\ \pi^+\ \pi^+$	8	$D_s^+ \to K_S^0\ \pi^+\ \pi^0$
9	$D_s^+ \to K^+\ K^-\ \pi^+\ \pi^0$	10	$D_s^+ \to K^+\ K^-\ \pi^+\ \pi^+\ \pi^-$		
			D_s^{*+}		
0	$D_s^{*+} \to D_s^+\ \gamma$	1	$D_s^{*+} \to D_s^+\ \pi^0$		
			Λ		
0	$\Lambda \to p\ \pi^-$				
			Σ^+		
0	$\Sigma^+ \to p\ \pi^0$				
			Λ_c^+		
0	$\Lambda_c^+ \to p\ K^-\ \pi^+$	1	$\Lambda_c^+ \to p\ K_S^0$	2	$\Lambda_c^+ \to \Lambda\ \pi^+\ \gamma$
3	$\Lambda_c^+ \to p\ \pi^-\ \pi^+$	4	$\Lambda_c^+ \to p\ K_S^0\ \pi^0$	5	$\Lambda_c^+ \to \Lambda\ \pi^+\ \pi^0\ \gamma$
6	$\Lambda_c^+ \to p\ K^-\ K^+$	7	$\Lambda_c^+ \to p\ K_S^0\ \pi^+\ \pi^-$	8	$\Lambda_c^+ \to \Lambda\ \pi^+\ \pi^-\ \pi^+\ \gamma$
9	$\Lambda_c^+ \to p\ K^-\ \pi^+\ \pi^0$	10	$\Lambda_c^+ \to \Lambda\ \pi^+$	11	$\Lambda_c^+ \to \Sigma^+\ \pi^+\ \pi^-$
12	$\Lambda_c^+ \to p\ K^-\ \pi^+\ \pi^0\ \pi^0$	13	$\Lambda_c^+ \to \Lambda\ \pi^+\ \pi^0$	14	$\Lambda_c^+ \to \Sigma^+\ \pi^+\ \pi^-\ \pi^0$
15	$\Lambda_c^+ \to p\ \pi^+\ \pi^+\ \pi^-\ \pi^-$	16	$\Lambda_c^+ \to \Lambda\ \pi^+\ \pi^-\ \pi^+$	17	$\Lambda_c^+ \to \Sigma^+\ \pi^0$

A.3 FEI FOR ANALYSTS

The FEI serves as a practical tool for reconstructing complete $\Upsilon(4S)$ decay events. Its implementation consists of two distinct phases: training on simulated data and subsequent application to independent datasets.

Training is performed centrally by the Belle II collaboration using large samples of simulated $\Upsilon(4S)$ decays,approximately 100 million events for both charged and neutral B-meson pairs. The process builds both hadronic and semileptonic tag candidates across multiple decay channels, applying classifier cuts at each stage of the reconstruction hierarchy. The output consists of trained weight files and four `ParticleLists` accessible to users: `B0:hadronic`, `B+:hadronic`, `B0:semi-leptonic`, and `B+:semi-leptonic`. Individual analysts do not perform their own training; instead, centrally produced versions are maintained and updated as the software evolves.

Rather than applying the FEI individually, analysts are encouraged to use official FEI skims,centrally produced datasets where the FEI has been applied with loose selections. This approach substantially reduces file sizes by discarding events without viable B_{tag} candidates, thus saving computational resources. The skim selections are intentionally permissive to avoid excessive signal loss while providing basic background suppression. Event-level requirements include at least three charged tracks and three ECL clusters satisfying quality criteria, plus a minimum visible energy of 4 GeV in the centre-of-mass frame. For B_{tag} candidates, selections include $M_{bc} > 5.2\ \text{GeV}/c^2$, $|\Delta E| < 0.3$ GeV, and $\mathcal{O}_{\text{FEI}} > 0.001$ (except for certain J/ψ decay modes where classifier training was unsuccessful, where the cut is looser). These cuts, summarised in Table A.4, retain most signal events while removing clear background. Additional background rejection is left to individual analyses.

Table A.4: Summary of the FEI skim selection criteria applied to B_{tag} candidates in official Belle II FEI skims.

Variable	Selection
Beam-constrained mass M_{bc}	$> 5.2\ \text{GeV}/c^2$
Energy difference $\|\Delta E\|$	< 0.3 GeV
Tagging probability $\mathcal{O}_{\text{FEI}}$	> 0.001 (except for certain J/ψ modes)

A.3.1 Calibrating the FEI Algorithm

The FEI tagging efficiency differs between MC and experimental data, and this difference must be corrected through specific calibration.
Calibration of the tagging algorithm is performed by reconstructing a signal B meson decay with a high branching fraction recoiling against a tagged B meson in $\Upsilon(4S) \to B\bar{B}$ events. Calibration factors are determined by comparing the number of reconstructed signal events in data and MC, and these factors are subsequently used to weight MC events in independent analyses to correct the FEI efficiency. It is essential that the selection applied to the B meson tag probability matches that used in the calibration, as the calibration factors are highly dependent on this value. The Belle II collaboration provides calibration results for several different $\mathcal{O}_{\text{FEI}}$ thresholds relevant to other analyses.
For the Belle experiment, the Full Reconstruction (FR) algorithm was calibrated using the complete dataset, corresponding to an integrated luminosity of 711 fb^{-1} [72]. The calibration used the semileptonic decays $B \to D^{(*)}\ell\nu_\ell$ ($\ell = e, \mu$), which have a combined branching fraction of 6.26% for $B^- \to D^{(*)0}\ell^-\overline{\nu}_\ell$ and 5.31% for $\bar{B}^0 \to D^{(*)+}\ell^-\overline{\nu}_\ell$. The large branching fractions and dataset size allowed calibration to be performed separately for each hadronic tag decay channel.
For Belle II, to maximize statistics in the 365 fb^{-1} Run1 dataset, the inclusive semileptonic decays $B^+ \to X^0\ell^+\nu_\ell$ and $B^0 \to X^-\ell^+\nu_\ell$ were used for calibration, where X^0 and X^- denote any neutral or charged hadronic system, respectively. A second calibration method employed a purer signal-side decay, with the signal B meson decaying to a D or D^* meson and a π, $B \to D^{(*)}\pi$. In this study, after hadronic B-tagging via the FEI, a single pion was reconstructed on the signal side. The momenta of the B_{tag} and pion were used to determine the mass of the recoiling particle (either the D or D^* meson). In this way, the $D^{(*)}$ meson was not required to be explicitly reconstructed on the signal side.
Hadronic signal-side decays offer a strong advantage for calibration studies due to the low backgrounds associated with fully reconstructing the event. However, the high purity comes at the cost of a low reconstruction efficiency, which, together with the low branching fractions characteristic of individual hadronic B meson decays, results in sample sizes that are statistically limited. As a result, the two independent calibration studies complemented one another well, representing signal-side decays with both high efficiency ($B \to X\ell\nu_\ell$) and high purity ($B \to D^{(*)}\pi$). The calibration factors resulting from both studies were then combined to produce a final set of official calibration factors for all the Belle II analyses, which uses FEI.

Both studies performed the calibration for individual B_{tag} decay modes (or subsets of modes), which are listed in Tab. A.2. A total of 10 neutral and 11 charged hadronic B_{tag} decay modes were individually calibrated, with a single factor determined as a weighted average over all of the remaining modes. The calibration factors are provided for all the analyses, including the $B^+ \to \tau^+ \nu_\tau$ analysis, and are used to correct the FEI efficiency in the MC simulation. The uncertainties on the calibration factors are propagated to the final results, ensuring that the systematic uncertainties associated with the FEI efficiency are properly accounted for. The factors oscillates between 0.6 and 1.0, depending on the $\mathcal{O}_{\text{FEI}}$ threshold and the specific B_{tag} decay mode considered.

B RUN DEPENDENT MONTE CARLO AT BELLE II

B.1 DATA PRODUCTION WORKFLOW

The data production workflow at Belle II is a multi-stage process designed to ensure accurate reconstruction and calibration of the raw data collected by the experiment. This process begins with the transfer of raw data from the online data acquisition system to the KEK Central Computing system (KEKCC), located at the KEK laboratory in Tsukuba, Japan. Once the data is archived at KEKCC, the Belle II core computing team registers the dataset to the distributed computing infrastructure supported by the Belle II Grid.
Subsequently, the data production team initiates the reconstruction of specific subsets of raw data, particularly the High-Level Trigger (HLT) skimmed samples, which are primarily employed for detector calibration. Among these, special calibration streams are produced, including the so-called "delayed Bhabha" samples. These samples consist of events recorded shortly after a Bhabha scattering event and are stored at a reduced rate of approximately 5 Hz. This low rate is necessitated by the computational cost associated with preserving full waveform information from the electromagnetic calorimeter (ECL), which is both data-intensive and time-consuming to process.
The calibration of real data begins with a rapid, initial procedure referred to as *prompt calibration*. This step requires expert input on the detector configuration and operating conditions relevant to the given run. The corresponding calibration constants, known as *payloads*, are compiled and stored in the Belle II conditions database. Following the completion of the prompt calibration step, the processing of the HLT "hadron" stream commences, leading to the full reconstruction of the complete dataset.
As soon as the reconstructed data is available, analysis-level datasets (commonly referred to as *skims*) are produced with high priority. These datasets are tailored to specific physics analyses and are accompanied by the generation of corresponding Monte Carlo samples.
Tipically, the Belle II experiment organizes one major Monte Carlo (MC) production campaign per year, in alignment with the software release cycles that follow a similar cadence. Currently, two main types of MC simulations are

generated: run-independent (MCri) and run-dependent (MCrd).
The MCri samples are generated using an idealized, time-averaged configuration of the Belle II detector. Detector responses and beam backgrounds in these samples are simulated based on the best knowledge obtained from dedicated simulation studies and background modeling, independently of actual data-taking conditions. While this approach is computationally efficient and well-suited for general-purpose studies, it does not fully account for time-dependent variations in detector performance or environmental conditions. Consequently, analyses relying solely on MCri may suffer from discrepancies between data and simulation, particularly in precision measurements.
In contrast, the MCrd samples are designed to provide a much more faithful representation of the real experimental environment. These simulations incorporate run-specific detector configurations and background conditions derived directly from data. Background contributions are modeled using real-time measurements from each sub-detector system, and the geometry and alignment of the detector components are matched to those observed during specific data-taking periods. This high level of realism is essential for analyses requiring stringent control of systematic uncertainties, particularly in cases where background suppression and signal extraction must be performed with high precision.
Due to the inclusion of detailed, run-dependent information and the need to simulate realistic background overlays, MCrd samples are significantly more resource-intensive to produce. As of the current production cycle, the MCrd dataset corresponds to approximately four times the integrated luminosity of the recorded data, reaching a total equivalent of about $2\,\text{ab}^{-1}$ (with the actual luminosity).
By contrast, MCri samples are produced independently of the accumulated data statistics, with a total simulated luminosity reaching up to $3\,\text{ab}^{-1}$. These samples constituted the primary source of simulation prior to the start of actual data-taking and continue to serve as a useful benchmark for many types of studies.
The generation of MCrd samples on the distributed Grid infrastructure poses significant computational and logistical challenges, given the scale and complexity of the task. Nonetheless, it represents a critical step toward enabling the full exploitation of the Belle II dataset for high-precision physics measurements. A schematic overview of the Belle II Grid computing model is shown in Fig. B.1.

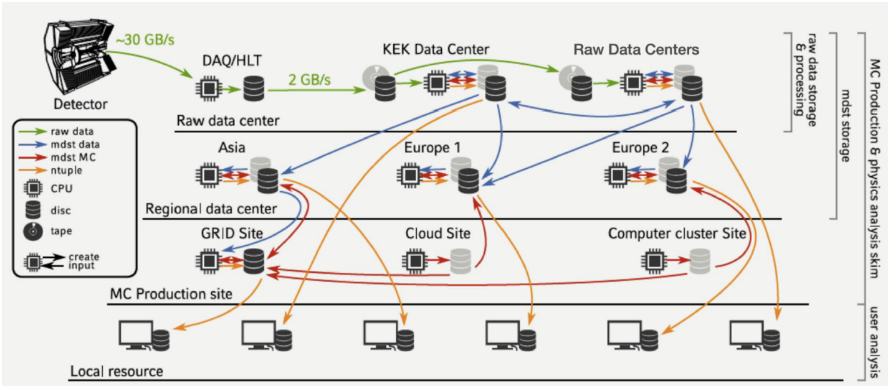

Figure B.1: Schematic overview of the Belle II Grid computing model, illustrating the flow of data from raw data acquisition to the analyses dataset for the users.

B.2 MC RUN-DEPENDENT PRODUCTION

The production of MCrd samples is significantly more complex and time-consuming than the generation of conventional run-independent simulations. This complexity arises from the need to faithfully reproduce the evolving detector and accelerator conditions that characterized each period of real data taking. At Belle II, each data-taking phase is identified through a combination of *experiment* and *run* numbers. A change in experimental configuration, such as a detector upgrade, modification in beam conditions, or a change in trigger settings, corresponds to a new experiment number. Within each experiment, multiple runs are recorded, each of varying duration and event statistics. Runs are the minimal unit where conditions of data taking is the same, and can last up to 8 hours.
The MCrd production process mirrors this structure and proceeds through several distinct steps: background overlay preparation, detector configuration retrieval, and job submission to the Belle II Grid infrastructure. Each of these steps is described in the following subsections.

B.2.1 Physics channels

MCrd samples are categorized into two broad classes: *generic* and *signal*. Generic samples include processes such as $e^+e^- \to q\bar{q}$, $\tau^+\tau^-$, $B\bar{B}$, low-multiplicity events (with fewer than five reconstructed tracks), and dimuon or Bhabha scattering events. The production of these samples is scaled according to a target integrated luminosity. A summary of the channels produced in the current

Table B.1: Summary of generic samples produced in MCrd campaigns at Belle II. `llXX` and `hhISR` include multi-lepton and hadronic with a γ_{ISR} final states, respectively.

Channel	cross section σ [nb]	MC/data scale
$q\bar{q}$	3.68	4
$\tau^+\tau^-$	0.919	4
$B\bar{B}$	1.05	4
$\mu^+\mu^-$	1.148	4
e^+e^-	295.8	0.1
$e^+e^-\ e^+e^-$	39.55	1
$e^+e^-\ \mu^+\mu^-$	18.83	1
$\gamma\ \gamma$	5.10	2
`llXX`	2.01	4
`hhISR`	0.216	1

campaign, along with their cross sections and luminosities, is presented in Tab. B.1.
Signal samples, on the other hand, correspond to specific final states of interest for targeted physics analyses. These are typically produced based on a fixed number of events, rather than an integrated luminosity. While the number of signal MC samples is considerably larger than that of the generic ones, their individual event statistics are smaller, making the production feasible. As of this writing, approximately 200 signal MC requests have been handled.

B.2.2 Background preparation

The incorporation of realistic beam-related background into MCrd is achieved through a dedicated data-driven procedure. Background events are selected using a special trigger configuration, activated shortly after Bhabha scattering events. This delay ensures that only pure background contributions, unrelated to primary collisions, are recorded. These background-enriched events are acquired at a low rate and subsequently unpacked to extract the raw digitized signals from tracking and calorimeter systems.
This digit-level information is then overlaid onto the MC generated sample events during simulation, ensuring a realistic modeling of background noise and detector occupancy. The background overlay is prepared separately for

each experiment number and, although not computationally intensive, is essential for reproducing the time-dependent environment of Belle II operations.

B.2.3 Detector configuration

One of the most resource-intensive phases of the MCrd production is the preparation of the detector configuration and calibration constants. Each Belle II subdetector system must provide run-specific payloads, including but not limited to alignment constants, dead channel maps, and time-dependent gain calibrations. These payloads are crucial for ensuring the accuracy of the simulated detector response. The aggregation and validation of these conditions data constitute a primary bottleneck in the production chain, and ongoing efforts are being directed at streamlining this process for future campaigns.
The payload can be very stable during the data-taking, like the geometry of the detector of the dead channel maps, or can change rapidly, like the position and the energy of the collision.

B.2.4 Submission to the Grid

The final step in the MCrd workflow is the distributed production of simulated events via the Belle II Grid infrastructure. The job submission system relies on structured `.json` files, which define the number of events to be generated for each run, weighted by the corresponding recorded luminosity, and a steering file, which uses the Belle II software package, `basf2`. As each run requires an independent simulation job, the total number of jobs submitted to the Grid is substantial.
Before full-scale production, a series of validation tests are performed on a dedicated test server to ensure correctness and stability. Once approved, the jobs are dispatched to the Grid and the resulting MCrd samples are uploaded and catalogued for use in physics analyses.

B.2.5 Book-keeping

Effective organization and accessibility of MCrd samples constitutes a critical component of the production workflow, serving two fundamental objectives: maintaining systematic organization of simulation outputs and ensuring user-friendly access for the entire collaboration.
The Belle II MC is organized with *collections*, which group datasets. When ana-

lysts submit computational jobs to the Belle II Grid infrastructure, they specify input datasets by referencing these collections for both experimental data and Monte Carlo samples. This standardized approach ensures consistency across different analysis workflows and facilitates reproducibility of results.
Each collection includes all Monte Carlo datasets corresponding to a specific physics process within a defined data-taking period. For example, a collection can have all $d\bar{d}$ Monte Carlo sample related to Run1 data. The hierarchical naming convention follows a structured format that encodes essential metadata directly within the collection identifier:

```
/belle/collection/MC/MC16rd_proc16_ddbar_Run1_4S_v1
```

This systematic nomenclature immediately conveys key information including the Monte Carlo campaign identifier (MC16rd), processing version (proc16), physics channel ($d\bar{d}$), data-taking period (Run1), collision energy configuration ($\Upsilon(4S)$), and dataset version (v1).
Beyond the hierarchical naming structure, each collection is accompanied by metadata that provides analysts information necessary for proper dataset utilization. This metadata includes parameters, such as the integrated luminosity. A representative example of collection metadata is shown below:

```
##########Metadata of Collection###############
name: /belle/collection/MC/MC16rd_proc16_ddbar_Run1_4S_v1
dataType: mc
dataLevel: mdst
description: Collection for MC16rd_proc16-Run1-ddbar-4S
int_luminosity: 1429.23/fb
#################################################
```

In future, a more detailed metadata schema is planned to be implemented, which will include additional parameters such as the number of events, cross sections, and other relevant information.

B.3 SUMMARY

The Belle II experiment is acquiring an unprecedented volume of data, making the accurate and efficient production of Monte Carlo samples a critical component of the collaboration's physics program. To meet the stringent requirements of high-precision measurements, a dedicated run-dependent Monte Carlo production framework has been developed. Although the system is inherently complex and computationally demanding, it provides the most realistic simu-

lation environment currently available within the collaboration.
By incorporating run-by-run variations in detector conditions and beam backgrounds, the MCrd samples enable a significant reduction in discrepancies between data and simulation. This improved fidelity is essential for controlling systematic uncertainties and enhancing the reliability of physics results.
As of today, Belle II has recorded approximately $500\,\text{fb}^{-1}$ of data, while the corresponding MCrd samples produced for high-multiplicity processes already amount to an integrated luminosity of about $2000\,\text{fb}^{-1}$, for the high multiplicity samples. This substantial MC production effort underscores the collaboration's commitment to high-quality simulation and robust data analysis, laying a strong foundation for future discoveries in flavor physics.
A detailed overview on the Monte Carlo run dependent production at Belle II was presented at 2025 EPS-HEP conference [73].

C R&D FOR FCC

C.1 MOTIVATION AND OVERVIEWS

High-precision calorimetry represents an important technology for next-generation high-energy physics experiments, particularly at proposed electron-positron colliders such as the Circular Electron Positron Collider (CEPC) [74] and the Future Circular Collider electron-positron program (FCC-ee) [67]. At these facilities, accurate reconstruction of jets and complex hadronic final states is essential for precision measurements of the Higgs boson properties and electroweak parameters. Among the various approaches to enhance calorimetric performance, *dual-readout calorimetry* stands out as a particularly promising technique. This method addresses one of the fundamental limitations of hadronic calorimetry: the event-by-event fluctuations in the electromagnetic fraction of hadronic showers. By simultaneously measuring both scintillation and Čerenkov light components from the same shower, dual-readout calorimetry can correct these fluctuations and significantly improve energy resolution.
Traditional implementations of dual-readout calorimetry [75, 76] rely on sampling structures incorporating alternating layers of scintillating and Čerenkov-sensitive optical fibers [77, 78, 79, 80, 81, 82]. While this approach has demonstrated promising results for hadronic energy resolution, it suffers from inherent limitations in electromagnetic performance due to sampling fluctuations that arise from the discrete nature of the active medium. Conversely, homogeneous calorimeters constructed from inorganic scintillating crystals offer exceptional electromagnetic energy resolution by providing complete containment and uniform response throughout the shower development. However, these systems traditionally lack the dual-readout capability necessary for optimal hadronic performance.
The IDEA (International Detector for Electron-positron Accelerator) [83] detector concept, proposed for the FCC-ee program, addresses this challenge through an innovative hybrid calorimeter design. This system combines a homogeneous crystal-based electromagnetic section with a fiber-based hadronic compartment, aiming to optimize performance for both electromagnetic and hadronic showers [84]. A critical requirement for this design is the implemen-

tation of dual-readout capabilities within the crystal electromagnetic calorimeter itself.

This appendix presents a study investigating the feasibility of implementing dual-readout techniques in homogeneous scintillating crystals. Specifically, we examine bismuth germanate (BGO) and bismuth silicate (BSO) crystals, utilizing Silicon Photomultipliers (SiPMs) to achieve the discrimination between scintillation and Čerenkov light components required for dual-readout operation.

C.2 DUAL-READOUT TECHNIQUES IN CRYSTAL CALORIMETERS

For this investigation, bismuth germanate (BGO) and bismuth silicate (BSO) crystals were selected based on their exceptional properties for calorimetric applications. Both materials exhibit high density and short radiation length, which are essential for compact electromagnetic shower containment. Additionally, they feature high scintillation light yields and elevated refractive indices (approximately 2.15 for BGO and 1.94 for BSO).

The experimental approach involved reading out each crystal from both ends using pairs of independent Silicon Photomultipliers, with each SiPM optimized for a specific light component [85, 86]. One channel (designated as the *s*-channel) was configured primarily for scintillation light detection, while the second channel (the *c*-channel) was optimized for Čerenkov light measurement. This dual-channel architecture enables the simultaneous collection of both light components from a single crystal volume.

The separation of scintillation and Čerenkov signals exploits the fundamental physical differences between these two light-generation mechanisms. Scintillation light is characterized by isotropic emission, with characteristic decay times on the order of tens to hundreds of nanoseconds, and broad spectral emission typically peaked in the visible range. In contrast, Čerenkov radiation exhibits prompt emission (sub-nanosecond timing), highly directional propagation along the particle trajectory, and a characteristic $1/\lambda^2$ spectral dependence that peaks at ultraviolet wavelengths.

To enhance the discrimination between these components, an optical filtering strategy was implemented in the *c*-channel. Specifically, a UG11 ultraviolet-transmitting optical filter [87] was employed to preferentially transmit short-wavelength light where the Čerenkov spectrum dominates, while simultaneously suppressing the longer-wavelength scintillation contribution. This spectral filtering, combined with pulse shape discrimination techniques based on the different temporal characteristics of the two light components, provides the foundation for effective signal separation.

The crystal used in this study were fabricated by the Shanghai Institute of Ceramics (SICCAS), following specifications optimized for dual-readout applications. Each crystal measured 150 mm in length with a square cross-section of $12 \times 12\,mm^2$, dimensions chosen to balance light collection efficiency with mechanical constraints. Before the test beam, comprehensive optical characterization was performed in laboratory conditions to determine key parameters such as optical transmittance and scintillation decay time constants.

Transmittance measurements confirmed transparency extending down to wavelengths of $320\,nm$, which is crucial for efficient collection of ultraviolet Čerenkov photons. Scintillation decay profiles were analyzed using double-exponential fits, revealing characteristic time constants of ($50\,ns$, $322\,ns$) for BGO and ($22\,ns$, $98\,ns$) for BSO. These temporal signatures provided the basis for the pulse shape templates used in subsequent signal decomposition analysis.

Figure C.1 presents the normalized emission spectra for both scintillation and Čerenkov light, overlaid with the measured transmission characteristics of the crystals and the UG11 optical filter. The scintillation emission peaks at approximately $480\,nm$, which aligns well with the peak photon detection efficiency of typical SiPMs, ensuring optimal light collection for the s-channel. The complementary spectral response achieved through optical filtering enables effective discrimination between the two light components.

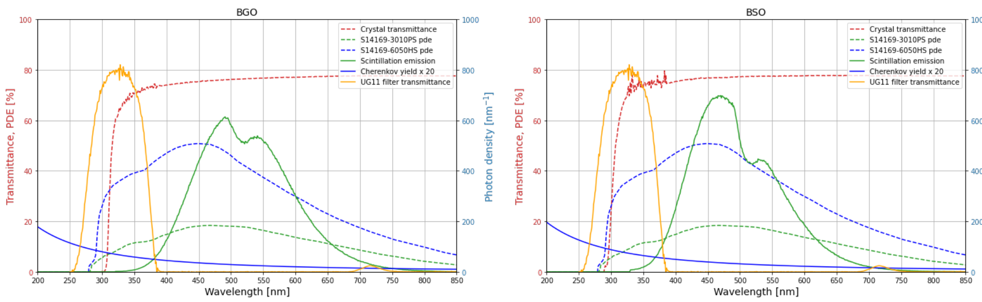

(a) BGO **(b)** BSO

Figure C.1: Normalized scintillation and Cherenkov emission spectra, overlaid with the transmission curves of the crystal and the UG11 filter. The photon detection efficiency of the C and S channel SiPMs at nominal over-voltage is also shown [85, 86].

C.3 EXPERIMENTAL SETUP

Together with Milano Bicocca and University of Perugia FCC-ee groups, we conducted the test beam at the H6 beamline of the CERN SPS North Area to validate the dual-readout approach under realistic conditions on July 2024. Crystals were exposed to 10 GeV positrons (for electromagnetic showers) and 120 GeV muons (as minimum ionizing particles) for the calibrations. The setup included a light-tight and thermally monitorated box, a rotating stage for angular scans, and a trigger system of scintillator counters and lead converters. Signals from SiPMs were read out with high-bandwidth amplifiers and acquired using a Tektronix MSO46B oscilloscope at 6.25Gs/ s, 1.5 GHz bandwidth, and 14 bit ADC. Data acquisition and slow control were managed through the MIDAS framework. Angular scans confirmed the expected directionality of the Čerenkov signal, and data were collected over a range of 5000 to 40000 events per run.

C.4 SIPM CALIBRATION AND SIGNAL RECONSTRUCTION

Calibration of the SiPMs was carried out in a dedicated laboratory setup using a Hamamatsu PLP-10 pulsed laser emitting at 405 nm. Two methods were employed:

- **Peak Identification (Method A)** was used for the c-channel, where the signal amplitude distribution displayed resolved photoelectron peaks. A linear fit to peak positions provided the single-$p.e.$ calibration factor, yielding 3.33 $mV/p.e.$ and 1.25 $mV/p.e.$ at 28 dB and 18 dB amplifier gain, respectively.

- **Fluctuation Analysis (Method B)** was used for the s-channel, where unresolved peaks necessitated a statistical approach. Assuming Poisson fluctuations, the variance of the signal was plotted against its mean for different laser intensities, and the slope provided the squared single-$p.e.$ amplitude. Calibration factors of 0.442 $mV/p.e.$ (18 dB gain) and 0.0421 $mV/p.e.$ (passive readout) were obtained.

Cross-validation between methods yielded agreement within 12%, which was included as a systematic uncertainty on the calibration constants. These values were subsequently used to convert waveforms into photoelectron-equivalent units for physics analysis.

C.5 SEPARATION OF SCINTILLATION AND ČERENKOV SIGNALS

A waveform decomposition technique was developed to isolate the scintillation and Čerenkov components in each event. The method modeled waveforms as a linear combination of two templates corresponding to the fast and slow components, respectively. This enabled event-by-event extraction of both signals without relying on external tracking or energy information.

The Čerenkov signal exhibited a clear directional peak at oblique angles, while the scintillation response was largely isotropic. To disentangle the scintillation and Čerenkov contributions on an event-by-event basis, the recorded waveforms were modeled as a linear superposition of two distinct components, each characterized by a dedicated pulse shape template. These templates $T(t)$ were obtained by convolving the expected photon arrival time distribution $P(t)$ at the SiPM surface with the detector's single-photon response (SPR) function:

$$T(t) = P(t) * SPR(t), \tag{C.1}$$

where $*$ denotes convolution. The SPR functions were extracted from calibration data acquired with a pulsed laser system, normalized to the single-photoelectron amplitude. Independent SPR templates were generated for each SiPM and preamplifier gain configuration used during the test beam campaign. The photon arrival time distributions $P(t)$ were derived from the scintillation decay constants measured in laboratory tests using cosmic rays. Separate templates were constructed for the Čerenkov (T_c) and scintillation (T_s) components. The full fit function used to model each waveform is defined as:

$$f(c, s, t_0) = c \cdot T_c(t - t_0) + s \cdot T_s(t - t_0), \tag{C.2}$$

where c and s are normalization parameters proportional to the number of detected Čerenkov and scintillation photons, respectively, and t_0 represents the time offset corresponding to the trigger. All three parameters are left free in the fit. The fitting procedure is based on χ^2 minimization.

Figure C.2 presents an example fit to a waveform from a 10 GeV e^+ beam event in BGO, demonstrating excellent agreement between the model and the observed signal in both channels. To ensure the quality of the waveform fits, a selection was applied based on the agreement between the total integrated charge in the data (Q_{data}) and in the fit result (Q_{fit}). Only events satisfying the following condition was retained:

$$0.75 < \frac{Q_{\mathrm{data}}}{Q_{\mathrm{fit}}} < 1.25, \tag{C.3}$$

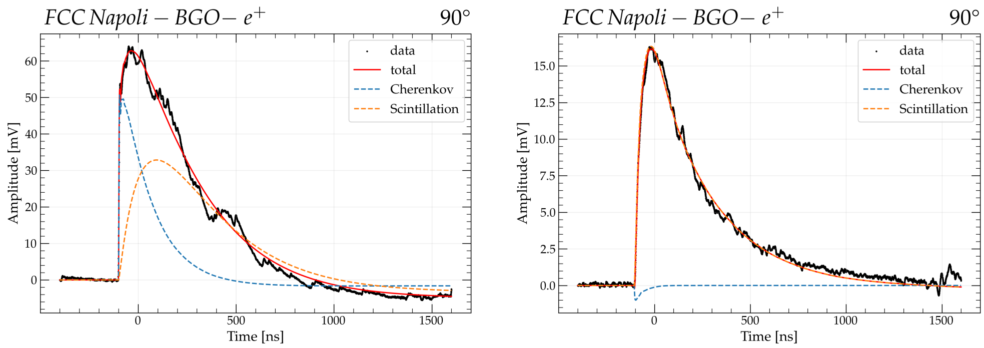

(a) *c*-channel **(b)** *s*-channel

Figure C.2: Example of waveform decomposition in BGO for a 10 GeV e^+ event. The black line shows the measured signal, while the total fit (red), Čerenkov (blue dashed), and scintillation (orange dashed) contributions are overlaid.

where Q_{data} is the total charge in the waveform and Q_{fit} is the total charge predicted by the fit. Additionally, pulses were required to exceed a dynamic amplitude threshold defined as

$$A > \mu + 5\sigma, \tag{C.4}$$

where μ and σ are the mean and standard deviation of the pre-signal baseline region ($t < t_0$). This selection ensures that only well-reconstructed and noise-free signals are included in the analysis.
Maximum Čerenkov-to-scintillation ratios of 0.15 (BGO) and 0.25 (BSO) were measured, corresponding to absolute Čerenkov yields of up to 140$p.e.$/ GeV. These results demonstrated the feasibility of separating Čerenkov light even in crystals with high scintillation output, validating the proposed dual-readout method for homogeneous calorimetry.

C.6 CONCLUSION AND OUTLOOK

This study aims to provide a proof-of-principle for implementing dual-readout calorimetry with inorganic scintillating crystals. Using BGO and BSO read out with fast SiPMs and optimized optical filtering, event-by-event separation of scintillation and Čerenkov signals was achieved under test beam conditions.
Future R&D will focus on scaling the technology to larger detector modules, enhancing the timing resolution of photodetectors, and exploring alternative

crystal materials with favorable light emission characteristics. These efforts are crucial for the development of next-generation calorimeters tailored to the demanding requirements of future e^+e^- colliders and precision Higgs physics.

BIBLIOGRAPHY

[1] Steven Weinberg. "A Model of Leptons." In: *Phys. Rev. Lett.* 19 (21 Nov. 1967), pp. 1264–1266. DOI: 10.1103/PhysRevLett.19.1264. URL: https://link.aps.org/doi/10.1103/PhysRevLett.19.1264.

[2] Sheldon L. Glashow. "Partial-symmetries of weak interactions." In: *Nuclear Physics* 22.4 (1961), pp. 579–588. ISSN: 0029-5582. DOI: https://doi.org/10.1016/0029-5582(61)90469-2. URL: https://www.sciencedirect.com/science/article/pii/0029558261904692.

[3] Abdus Salam. "Weak and electromagnetic interactions." In: *Selected Papers of Abdus Salam*, pp. 244–254. DOI: 10.1142/9789812795915_0034. eprint: https://www.worldscientific.com/doi/pdf/10.1142/9789812795915_0034. URL: https://www.worldscientific.com/doi/abs/10.1142/9789812795915_0034.

[4] F. Englert and R. Brout. "Broken Symmetry and the Mass of Gauge Vector Mesons." In: *Phys. Rev. Lett.* 13 (9 Aug. 1964), pp. 321–323. DOI: 10.1103/PhysRevLett.13.321. URL: https://link.aps.org/doi/10.1103/PhysRevLett.13.321.

[5] Peter W. Higgs. "Broken Symmetries and the Masses of Gauge Bosons." In: *Phys. Rev. Lett.* 13 (16 Oct. 1964), pp. 508–509. DOI: 10.1103/PhysRevLett.13.508. URL: https://link.aps.org/doi/10.1103/PhysRevLett.13.508.

[6] G. S. Guralnik, C. R. Hagen, and T. W. B. Kibble. "Global Conservation Laws and Massless Particles." In: *Phys. Rev. Lett.* 13 (20 Nov. 1964), pp. 585–587. DOI: 10.1103/PhysRevLett.13.585. URL: https://link.aps.org/doi/10.1103/PhysRevLett.13.585.

[7] W. Pauli. "Exclusion Principle, Lorentz Group and Reflection of Space-Time and Charge." In: *Niels Bohr and the Development of Physics*. Ed. by W. Pauli, L. Rosenfeld, and V. Weisskopf. New York: McGraw-Hill, 1955, pp. 30–51.

[8] Gerhart Lüders. "Proof of the TCP theorem." In: *Annals of Physics* 2.1 (1957), pp. 1–15. ISSN: 0003-4916. DOI: https://doi.org/10.1016/0003-4916(57)90032-5. URL: https://www.sciencedirect.com/science/article/pii/0003491657900325.

[9] J. H. Christenson et al. "Evidence for the 2π Decay of the K_2^0 Meson." In: *Phys. Rev. Lett.* 13 (4 July 1964), pp. 138–140. DOI: 10.1103/PhysRevLett.13.138. URL: https://link.aps.org/doi/10.1103/PhysRevLett.13.138.

[10] C. S. Wu et al. "Experimental Test of Parity Conservation in Beta Decay." In: *Phys. Rev.* 105 (4 Feb. 1957), pp. 1413–1415. DOI: 10.1103/PhysRev.105.1413. URL: https://link.aps.org/doi/10.1103/PhysRev.105.1413.

[11] C. B. Adams et al. *Axion Dark Matter*. 2023. arXiv: 2203.14923 [hep-ex]. URL: https://arxiv.org/abs/2203.14923.

[12] X. Fan et al. "Measurement of the Electron Magnetic Moment." In: *Phys. Rev. Lett.* 130 (7 Feb. 2023), p. 071801. DOI: 10.1103/PhysRevLett.130.071801. URL: https://link.aps.org/doi/10.1103/PhysRevLett.130.071801.

[13] Thomas E. Browder et al. "New physics at a Super Flavor Factory." In: *Rev. Mod. Phys.* 81 (4 Dec. 2009), pp. 1887–1941. DOI: 10.1103/RevModPhys.81.1887. URL: https://link.aps.org/doi/10.1103/RevModPhys.81.1887.

[14] Nicola Cabibbo. "Unitary Symmetry and Leptonic Decays." In: *Phys. Rev. Lett.* 10 (12 June 1963), pp. 531–533. DOI: 10.1103/PhysRevLett.10.531. URL: https://link.aps.org/doi/10.1103/PhysRevLett.10.531.

[15] S. L. Glashow, J. Iliopoulos, and L. Maiani. "Weak Interactions with Lepton-Hadron Symmetry." In: *Phys. Rev. D* 2 (7 Oct. 1970), pp. 1285–1292. DOI: 10.1103/PhysRevD.2.1285. URL: https://link.aps.org/doi/10.1103/PhysRevD.2.1285.

[16] J. -E. Augustin et al. "Discovery of a Narrow Resonance in e^+e^- Annihilation." In: *Phys. Rev. Lett.* 33 (23 Dec. 1974), pp. 1406–1408. DOI: 10.1103/PhysRevLett.33.1406. URL: https://link.aps.org/doi/10.1103/PhysRevLett.33.1406.

[17] J. J. Aubert et al. "Experimental Observation of a Heavy Particle J." In: *Phys. Rev. Lett.* 33 (23 Dec. 1974), pp. 1404–1406. DOI: 10.1103/PhysRevLett.33.1404. URL: https://link.aps.org/doi/10.1103/PhysRevLett.33.1404.

[18] Makoto Kobayashi and Toshihide Maskawa. "CP-Violation in the Renormalizable Theory of Weak Interaction." In: *Progress of Theoretical Physics* 49.2 (Feb. 1973), pp. 652–657. ISSN: 0033-068X. DOI: 10.1143/PTP.49.652. eprint: https://academic.oup.com/ptp/article-pdf/49/2/652/5257692/49-2-652.pdf. URL: https://doi.org/10.1143/PTP.49.652.

[19] Lincoln Wolfenstein. "Parametrization of the Kobayashi-Maskawa Matrix." In: *Phys. Rev. Lett.* 51 (21 Nov. 1983), pp. 1945–1947. DOI: 10.1103/PhysRevLett.51.1945. URL: https://link.aps.org/doi/10.1103/PhysRevLett.51.1945.

[20] Ludovico Vittorio for the UTfit Collaboration. "Constraints on New Physics from Global Fits." In: Contribution to EPS-HEP 2025. Marseille, France, 2025. URL: https://indico.in2p3.fr/event/33627/contributions/155084/.

[21] Minoru Tanaka and Ryoutaro Watanabe. "New physics in the weak interaction of $\overline{B} \to D^{(*)}\tau\overline{\nu}$." In: *Phys. Rev. D* 87 (3 Feb. 2013), p. 034028. DOI: 10.1103/PhysRevD.87.034028. URL: https://link.aps.org/doi/10.1103/PhysRevD.87.034028.

[22] S. Navas et al. "Review of particle physics." In: *Phys. Rev. D* 110.3 (2024), p. 030001. DOI: 10.1103/PhysRevD.110.030001.

[23] J. P. Lees et al. "Evidence of $B^+ \to \tau^+\nu$ decays with hadronic B tags." In: *Phys. Rev. D* 88 (3 Aug. 2013), p. 031102. DOI: 10.1103/PhysRevD.88.031102. URL: https://link.aps.org/doi/10.1103/PhysRevD.88.031102.

[24] K. Hara et al. "Evidence for $B^- \to \tau^-\overline{\nu}_\tau$ with a Hadronic Tagging Method Using the Full Data Sample of Belle." In: *Phys. Rev. Lett.* 110 (13 Mar. 2013), p. 131801. DOI: 10.1103/PhysRevLett.110.131801. URL: https://link.aps.org/doi/10.1103/PhysRevLett.110.131801.

[25] B. Kronenbitter et al. "Measurement of the branching fraction of $B^+ \to \tau^+\nu_\tau$ decays with the semileptonic tagging method." In: *Phys. Rev. D* 92 (5 Sept. 2015), p. 051102. DOI: 10.1103/PhysRevD.92.051102. URL: https://link.aps.org/doi/10.1103/PhysRevD.92.051102.

[26] B. Aubert et al. "Search for $B^+ \to \ell^+\nu_\ell$ recoiling against $B^- \to D^0\ell^-\overline{\nu}X$." In: *Phys. Rev. D* 81 (5 Mar. 2010), p. 051101. DOI: 10.1103/PhysRevD.81.051101. URL: https://link.aps.org/doi/10.1103/PhysRevD.81.051101.

[27] Sw. Banerjee et al. *Averages of b-hadron, c-hadron, and τ-lepton properties as of 2023*. 2024. arXiv: 2411.18639 [hep-ex]. URL: https://arxiv.org/abs/2411.18639.

[28] Andreas Crivellin et al. "Lepton-flavor violating B decays in generic $Z^{'}$ models." In: *Phys. Rev. D* 92 (5 Sept. 2015), p. 054013. DOI: 10.1103/PhysRevD.92.054013. URL: https://link.aps.org/doi/10.1103/PhysRevD.92.054013.

[29] Christoph Niehoff, Peter Stangl, and David M. Straub. "Direct and indirect signals of natural composite Higgs models." In: *Journal of High Energy Physics* 2016.1 (2016), p. 119. DOI: 10.1007/JHEP01(2016)119. URL: https://doi.org/10.1007/JHEP01(2016)119.

[30] Wei-Shu Hou. "Enhanced charged Higgs boson effects in $B \to \tau\nu$, $\mu\nu$ and $\tau\nu X$." In: *Phys. Rev. D* 48 (5 Sept. 1993), pp. 2342–2344. DOI: 10.1103/PhysRevD.48.2342. URL: https://link.aps.org/doi/10.1103/PhysRevD.48.2342.

[31] Andreas Crivellin, Christoph Greub, and Ahmet Kokulu. "Explaining $B \to D\tau\nu$, $B \to D^*\tau\nu$ and $B \to \tau\nu$ in a 2HDM of type III." In: *Phys. Rev. D* 86 (2012), p. 054014. DOI: 10.1103/PhysRevD.86.054014.

[32] J. Haller et al. "Update of the global electroweak fit and constraints on two-Higgs-doublet models." In: *Eur. Phys. J. C* 78.8 (2018), p. 675. DOI: 10.1140/epjc/s10052-018-6131-3.

[33] Chuan-Hung Chen and Takaaki Nomura. "Charged Higgs boson contribution to $B_q^- \to \ell\bar{\nu}$ and $\bar{B} \to (P,V)\ell\bar{\nu}$ in a generic two-Higgs doublet model." In: *Phys. Rev. D* 98.9 (2018), p. 095007. DOI: 10.1103/PhysRevD.98.095007.

[34] Andrei Angelescu et al. "Single leptoquark solutions to the B-physics anomalies." In: *Phys. Rev. D* 104 (5 Sept. 2021), p. 055017. DOI: 10.1103/PhysRevD.104.055017. URL: https://link.aps.org/doi/10.1103/PhysRevD.104.055017.

[35] Gudrun Hiller, Daniel Loose, and Keri Schönwald. "Leptoquark flavor patterns & B decay anomalies." In: *Journal of High Energy Physics* 2016.12 (2016), p. 27. DOI: 10.1007/JHEP12(2016)027. URL: https://doi.org/10.1007/JHEP12(2016)027.

[36] D. A. Bryman and R. Shrock. "Improved Constraints on Sterile Neutrinos in the MeV to GeV Mass Range." In: *Phys. Rev. D* 100.5 (2019), p. 053006. DOI: 10.1103/PhysRevD.100.053006.

[37] Alfredo Walter Mario Guerrera and Stefano Rigolin. "ALP Production in Weak Mesonic Decays." In: *Fortsch. Phys.* 71.2-3 (2023), p. 2200192. DOI: 10.1002/prop.202200192.

[38] G.C. Branco et al. "Theory and phenomenology of two-Higgs-doublet models." In: *Physics Reports* 516.1 (2012), pp. 1–102. DOI: 10.1016/j.physrep.2012.02.002. URL: https://doi.org/10.1016/j.physrep.2012.02.002.

[39] W. Buchmuller, R. Ruckl, and D. Wyler. "Leptoquarks in lepton-quark collisions." In: *Physics Letters B* 191.4 (1987). Erratum: Phys. Lett. B 448, 320 (1999), pp. 442–448. DOI: 10.1016/0370-2693(87)90637-X. URL: https://doi.org/10.1016/0370-2693(87)90637-X.

[40] E Kou et al. "The Belle II Physics Book." In: *Progress of Theoretical and Experimental Physics* 2019.12 (Dec. 2019). ISSN: 2050-3911. DOI: 10.1093/ptep/ptz106. URL: http://dx.doi.org/10.1093/ptep/ptz106.

[41] SuperB Collaboration. *SuperB: A High-Luminosity Asymmetric e+ e- Super Flavor Factory. Conceptual Design Report*. 2007. arXiv: 0709.0451 [hep-ex].

[42] K. Adamczyk et al. "The Belle II silicon vertex detector assembly and mechanics." In: *Nucl. Instrum. Meth. A* 845 (2017). Ed. by G. Badurek et al., pp. 38–42. DOI: 10.1016/j.nima.2016.03.100.

[43] Wikipedia contributors. *Monte Carlo method — Wikipedia, The Free Encyclopedia*. 2024. URL: https://en.wikipedia.org/wiki/Monte_Carlo_method.

[44] D. J. Lange. "The EvtGen particle decay simulation package." In: *Nucl. Instrum. Meth.* A462 (2001), p. 152. DOI: 10.1016/S0168-9002(01)00089-4.

[45] S. Jadach, B. F. L. Ward, and Z. Was. "The precision Monte Carlo event generator KK for two-fermion final states in e^+e^- collisions." In: *Comput. Phys. Commun.* 130 (2000), p. 260. DOI: 10.1016/S0010-4655(00)00048-5.

[46] Torbjörn Sjöstrand et al. "An Introduction to PYTHIA 8.2." In: *Comput. Phys. Commun.* 191 (2015), pp. 159–177. DOI: 10.1016/j.cpc.2015.01.024.

[47] S. Jadach, J. H. Kuhn, and Z. Was. "TAUOLA: A library of Monte Carlo programs to simulate decays of polarized τ leptons." In: *Comput. Phys. Commun.* 64 (1990), p. 275. DOI: 10.1016/0010-4655(91)90038-M.

[48] N. Davidson, T. Przedzinski, and Z. Was. *PHOTOS Interface in C++; Technical and Physics Documentation*. 2015. arXiv: 1011.0937 [hep-ph].

[49] Elisabetta Barberio and Zbigniew Was. "PHOTOS: A Universal Monte Carlo for QED radiative corrections. Version 2.0." In: *Comput. Phys. Commun.* 79 (1994), p. 291. DOI: 10.1016/0010-4655(94)90074-4.

[50] S. Agostinelli et al. "GEANT4: A simulation toolkit." In: *Nucl. Instrum. Meth.* A506 (2003), pp. 250–303. DOI: 10.1016/S0168-9002(03)01368-8.

[51] Thomas Kuhr et al. "The Belle II Core Software." In: *Comput. Softw. Big Sci.* 3.1 (2019), p. 1. DOI: 10.1007/s41781-018-0017-9.

[52] N. Katayama et al. "PANTHER: A Data Management System for the Belle Experiment." In: *IEEE Trans. Nucl. Sci.* 47.2 (2000), pp. 443–447. DOI: 10.1109/23.856464.

[53] Rene Brun and Fons Rademakers. "ROOT — An object oriented data analysis framework." In: *Nucl. Instrum. Meth. A* 389 (1997), pp. 81–86. DOI: 10.1016/S0168-9002(97)00048-X.

[54] Python Software Foundation. *Python Language Reference, version 3*. https://www.python.org/. 2023.

[55] Charles R. Harris et al. "Array programming with NumPy." In: *Nature* 585 (2020), pp. 357–362. DOI: 10.1038/s41586-020-2649-2.

[56] Pauli Virtanen et al. "SciPy 1.0: Fundamental Algorithms for Scientific Computing in Python." In: *Nature Methods* 17 (2020), pp. 261–272. DOI: 10.1038/s41592-019-0686-2.

[57] Fabian Pedregosa et al. "Scikit-learn: Machine Learning in Python." In: *J. Mach. Learn. Res.* 12 (2011), pp. 2825–2830.

[58] J. D. Hunter. "Matplotlib: A 2D Graphics Environment." In: *Computing in Science & Engineering* 9.3 (2007), pp. 90–95. DOI: 10.1109/MCSE.2007.55.

[59] Geoffrey C. Fox and Stephen Wolfram. "Observables for the Analysis of Event Shapes in e^+e^- Annihilation and Other Processes." In: *Phys. Rev. Lett.* 41 (23 Dec. 1978), pp. 1581–1585. DOI: 10.1103/PhysRevLett.41.1581. URL: https://link.aps.org/doi/10.1103/PhysRevLett.41.1581.

[60] Lena Feld. *Continuum suppression in Belle II*. Zenodo. https://doi.org/10.5281/zenodo.22016. 2020.

[61] D Martschei et al. "Advanced event reweighting using multivariate analysis." In: *Journal of Physics: Conference Series* 368.1 (June 2012), p. 012028. DOI: 10.1088/1742-6596/368/1/012028. URL: https://dx.doi.org/10.1088/1742-6596/368/1/012028.

[62] Thomas Keck. "FastBDT: A Speed-Optimized Multivariate Classification Algorithm for the Belle II Experiment." In: *Comput. Softw. Big Sci.* 1.1 (2017), p. 2. DOI: 10.1007/s41781-017-0002-8.

[63] *RooFit package*. https://root.cern/manual/roofit/.

[64] A L Read. "Presentation of search results: the CLs technique." In: *Journal of Physics G: Nuclear and Particle Physics* 28.10 (Sept. 2002), p. 2693. DOI: 10.1088/0954-3899/28/10/313. URL: https://dx.doi.org/10.1088/0954-3899/28/10/313.

[65] Y. Aoki et al. *FLAG Review 2024*. 2025. arXiv: 2411.04268 [hep-lat]. URL: https://arxiv.org/abs/2411.04268.

[66] Alessandro Gaz et al. "The Belle II Experiment at SuperKEKB." In: *Input to the European Strategy for Particle Physics – 2026 update*. Indico contribution. Contribution no.6461621; Presented online via CERN Indico. Europe/Zurich, Apr. 2025. URL: https://indico.cern.ch/event/1439855/contributions/6461621/.

[67] Wolfgang Bartmann et al. *Future Circular Collider Feasibility Study Report Volume 1: Physics and Experiments*. 2025. DOI: 10.17181/CERN.9DKX.TDH9. URL: http://cds.cern.ch/record/2928193.

[68] I. Adachi et al. "Measurement of $B^+ \to \tau^+ \nu_\tau$ branching fraction with a hadronic tagging method at Belle II." In: *Phys. Rev. D* 112 (7 Oct. 2025), p. 072002. DOI: 10.1103/dcwd-5tg4. URL: https://link.aps.org/doi/10.1103/dcwd-5tg4.

[69] Giovanni Gaudino. *$\mathcal{B}(B \to \tau\nu)$ measurement with the hadronic FEI at Belle II*. Contribution to Moriond EW 2025. La Thuile, Italy, 2025. arXiv: 2506.03000 [hep-ex]. URL: https://indico.in2p3.fr/event/35965/contributions/152391/.

[70] Thomas Keck. *Machine Learning at the Belle II Experiment: The Full Event Interpretation and Its Validation on Belle Data*. 1st ed. Springer Theses. Springer International Publishing, 2018, pp. 63–100. URL: https://www.springer.com/gp/book/9783319982489.

[71] M. Feindt and U. Kerzel. "The NeuroBayes neural network package." In: *Nuclear Instruments and Methods in Physics Research Section A: Accelerators, Spectrometers, Detectors and Associated Equipment* 559.1 (2006). Proceedings of the X International Workshop on Advanced Computing and Analysis Techniques in Physics Research, pp. 190–194. ISSN: 0168-9002. DOI: https://doi.org/10.1016/j.nima.2005.11.166. URL: https://www.sciencedirect.com/science/article/pii/S0168900205022679.

[72] A. Sibidanov et al. "Study of exclusive $B \to X_u \ell \nu$ decays and extraction of $|V_{ub}|$ using full reconstruction tagging at the Belle experiment." In: *Phys. Rev. D* 88 (3 Aug. 2013), p. 032005. DOI: 10.1103/PhysRevD.88.032005. URL: https://link.aps.org/doi/10.1103/PhysRevD.88.032005.

[73] Giovanni Gaudino for the Belle II Data Production group. "Run Dependent Monte Carlo at Belle II." In: Contribution to EPS-HEP 2025. Marseille, France, 2025. URL: https://indico.in2p3.fr/event/33627/contributions/155250/.

[74] Mingyi Dong et al. "CEPC Conceptual Design Report: Volume 2 - Physics & Detector." In: (Nov. 2018). Ed. by João Barreiro Guimarães da Costa et al. arXiv: 1811.10545 [hep-ex].

[75] Roberto Ferrari et al. "Dual-readout calorimetry." In: *Int. J. Mod. Phys. A* 34.13n14 (2019), p. 1940019. DOI: 10.1142/S0217751X19400190.

[76] Sehwook Lee, Michele Livan, and Richard Wigmans. "Dual-Readout Calorimetry." In: *Rev. Mod. Phys.* 90.2 (2018), p. 025002. DOI: 10.1103/RevModPhys.90.025002. arXiv: 1712.05494 [physics.ins-det].

[77] N. Akchurin et al. "Electron detection with a dual-readout calorimeter." In: *Nucl. Instrum. Meth. A* 536 (2005), pp. 29–51. DOI: 10.1016/j.nima.2004.06.178.

[78] N. Akchurin et al. "Hadron and jet detection with a dual-readout calorimeter." In: *Nucl. Instrum. Meth. A* 537 (2005), pp. 537–561. DOI: 10.1016/j.nima.2004.07.285.

[79] N. Akchurin et al. "Comparison of high-energy electromagnetic shower profiles measured with scintillation and Cherenkov light." In: *Nucl. Instrum. Meth. A* 548 (2005), pp. 336–354. DOI: 10.1016/j.nima.2005.03.169.

[80] N. Akchurin et al. "Dual-readout Calorimetry." In: (July 2013). arXiv: 1307.5538 [physics.ins-det].

[81] S. Lee et al. "Hadron detection with a dual-readout fiber calorimeter." In: *Nuclear Instruments and Methods in Physics Research Section A: Accelerators, Spectrometers, Detectors and Associated Equipment* 866 (Sept. 2017), pp. 76–90. ISSN: 0168-9002. DOI: 10.1016/j.nima.2017.05.025. URL: http://dx.doi.org/10.1016/j.nima.2017.05.025.

[82] N. Akchurin et al. "The electromagnetic performance of the RD52 fiber calorimeter." In: *Nucl. Instrum. Meth. A* 735 (2014), pp. 130–144. DOI: 10.1016/j.nima.2013.09.033.

[83] The IDEA Study Group. *The IDEA detector concept for FCC-ee*. 2025. arXiv: 2502.21223 [physics.ins-det]. URL: https://arxiv.org/abs/2502.21223.

[84] Marco T. Lucchini et al. "Particle flow with a hybrid segmented crystal and fiber dual-readout calorimeter." In: *JINST* 17.06 (2022), P06008. DOI: 10.1088/1748-0221/17/06/P06008. arXiv: 2202.01474 [hep-ex].

[85] Hamamatsu Photonics. *MPPC S14160 Series*. https://www.hamamatsu.com/eu/en/product/optical-sensors/mppc/mppc_mppc-array/S14160-6050HS.html. Accessed: 2025-06-26. 2020.

[86] Hamamatsu Photonics. *MPPC S14160-3010 Series Datasheet*. https://www.hamamatsu.com/eu/en/product/type/S14160-3010PS/index.html. Accessed: 2025-06-26. 2020.

[87] SCHOTT AG. *UG11 Bandpass Filter Datasheet*. https://www.https://media.schott.com/api/public/content/84cc6e733284498b8fd901559a6f883b?v=3b93aa4e. Accessed: June 2025.

ACKNOWLEDGEMENTS

For purely bureaucratic reasons, this doctoral thesis must have a single author; however, fortunately for this author, the theses was not at all a solitary work. Writing a document like this is only the final part of a work that began in November 2021, more than 4 years ago, when I joined the Belle II group in Napoli, which has always helped me, supported me both scientifically and humanly, and welcomed me into this world.

First of all, I would like to thank Prof. Guglielmo De Nardo, who has been an important guide for the writing of this thesis, having played two fundamental roles: on the one hand, he has always been formal and professional when discussing physics, various bureaucracies, and work organization; on the other hand, however, he has always been very willing to work together, to read pages and pages of documents, even with a 7-hour time difference.

Many thanks also to Prof. Mario Merola, who has always shown great interest in my work and has given me excellent advices, both scientific and behavioral, in particular during our walks around the KEK accelerator (sometimes even 2 walks).

Many thanks to Dr. Marcello Campajola, my idol and mentor, as he likes to define himself. It has been wonderful to share all phases of this work with him, and he has always given me excellent suggestions, with his jokes and his way of being, always cynical and realistic. Thanks to all his advice and maxims, I think I am a better physicist and also a better person.

I sincerely thank also Dr. Silvio Pardi, Dr. Marco Mirra, and Prof. Raffaele Giordano, who have broadened my knowledge of the research world, always in a kind and never overwhelming manner.

I would like to thank all the Belle II collaboration, but I particularly want to thank Dr. Stefano Lacaprara, who for some reason decided that a somewhat clumsy person, never met before, should do Monte Carlo. Beyond what I can only consider madness, he has always helped me find the best and most elegant way to solve the small problems that arose during these years of working together, which I hope can last much longer, because it has been a pleasure working with his scientific brilliance.

I spent a large part of these doctoral years working with the Belle II group in Nagoya. In particular, I would like to thank Prof. Toru Iijima, who allowed

me to broaden my scientific and cultural horizons by letting me live in Nagoya for three months and work in the beautiful *N-Lab*, which gave an important boost to this work, mainly thanks to the person with whom I shared this work, Dr. Michele Aversano. Many thanks to Michele for his company during the months in Nagoya and all the times at KEK. Thanks for his scientific help, and for his help with Japan and Japanese. ありがとうございま。
Finally, I would like to thank all my Ph.D. colleagues from the Scuola Superiore Meridionale, with whom I shared a relatively short but intense and fun period, made of study, work, exams, but also moments of leisure and pizzas in San Marcellino.